

**A study on characteristics and verification method  
for moiré minimization in 3D display**

**July 2019,**

**Lee Hyoung**

## Contents

### 1 Introduction

1.1 Background .....	1
1.1.1 Moiré phenomenon .....	1
1.1.2 Definition of moiré .....	2
1.2 Objective & Outline .....	4

### 2 Behaviors of moiré fringes induced by plate thickness

2.1 Introduction .....	5
2.2 Theoretical ground of leading chirped moiré fringes .....	7
2.3 Moiré fringe simulation .....	11
2.4 Experimental results .....	14
2.5 Conclusion .....	18

### 3 Color moirés in contact-type three-dimensional displays

3.1 Introduction .....	19
3.2 Parts of a manuscript .....	21

3.3 Color moirés in contact-type 3-D imaging .....	23
3.4 A formula for the moiré fringe periods .....	29
3.5 Moiré characteristic for different VZFO .....	30
3.6 Moiré reductions methods .....	32
3.7 Conclusions .....	35
4 Fringe periods of color moirés in contact-type 3-D displays	
4.1 Introduction .....	36
4.2 Derivation of moiré fringe periods in the contact-type 3-D displays .....	37
4.3 Experimental set-up .....	41
4.4 Experimental results .....	43
4.5 Conclusion .....	51
5 Simulation of slanted color moirés in IP-type 3-D displays	
5.1 Introduction .....	52
5.2 Behaviors of the color moirés .....	53
5.3 Moiré fringe simulation .....	54
5.4 Moiré fringe simulation .....	57
5.5 Conclusion .....	62

6. Holographic and light field imaging as future 3D displays	
6.1 Introduction	63
6.2 Parameters defining the quality of 3-D images	65
6.3 History of 3D imaging: From stereo imaging to light field displays	67
6.4 The condition to be a light field display	76
6.5 The difference in light field characteristics	
between Holographic and light field images	79
6.6 Problems and current issues in holographic and light field imaging	85
6.7 Future progresses in the holographic and light field displays	90
6.8 Conclusions	91
7. Summaries and conclusions	93
Reference	96
List of publications	111

# 1 Introduction

## 1.1 Background

### 1.1.1 Moiré phenomenon

The moiré phenomenon is one of the display characteristics found in the 1960s. Normally, moiré is called interference pattern, wavy pattern, or grid pattern, which refers to stripes that are created visually by the difference of these cycles when repeatedly joining repeated patterns. moiré patterns appear in many different situations. The moiré phenomenon can be found not only in a display monitor

3(TV), printed photographs, documents containing pattern images but also in buildings, clothing, etc... As mentioned above, the moiré phenomenon is one of phenomena easily found in our everyday life. The moiré effect is a visual optical effect observed in regular superposed layers. To a considerable extent, the moiré effect is caused by the periodicity of layers, such as the highly regular pixel grid of a digital screen, a lenticular or barrier plate of a typical autostereoscopic three-dimensional display. The moiré fringes form a patterned background which is effectively added to a displayed image, and the image quality degrades.



The bottom of the escalator



Clothing fibers



Display monitor



Appearance of building

Fig. 1-1. Examples of Moiré phenomena found in everyday life

To provide the high quality, the visibility of the moiré patterns should be estimated and the moiré effect should be minimized [1-1]. In order to realize this moiré minimization method, definition of moiré, geometrical characteristic, color characteristic, period characteristic and mathematical expression should be studied.

### 1.1.2 Definition of moiré

moiré effect is a visual perception that occurs when viewing a set of lines or dots that is superposed on another set of lines or dots, where the sets differ in relative size, angle, or spacing. We cannot see any moiré phenomenon when we look at line image at regular intervals, but when we overlap one-line image of the same line or rotate it at a certain angle, we can clearly see the moiré phenomenon. The moiré effect can be seen when looking through ordinary window screens at another screen of background.

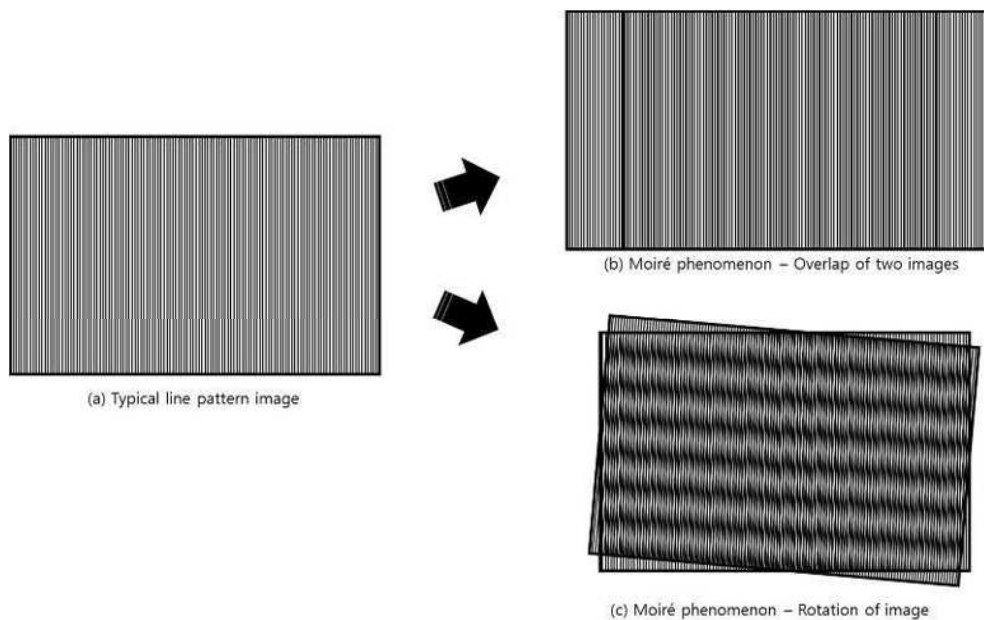


Fig. 1-2. Basic principle of moiré phenomenon

The moiré phenomenon can explain the moiré by its geometric representation. In other words, a natural interference effects can be explained by overlapping with two or more plates with regular patterns are superposed. In this moiré phenomenon image, it can be classified into dense area and sparse area. In dense area, it is lines in two patterns are barely or not matched to each other. For this reason, this area looks dark and dense. Also, in sparse area, it is lines in two patterns are completely or almost matched to each other [1-2]. This distinctive feature can be found in all moiré phenomena. This allows us to study the characteristics of moiré. We can do moiré minimization through prediction, evaluation, and verification of moiré through our research results.

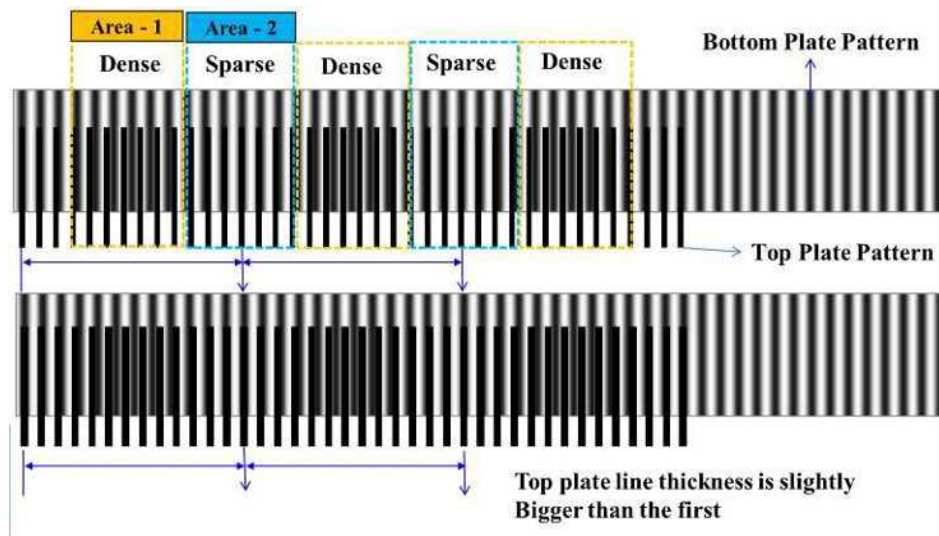


Fig. 1-3. Geometrical representation of moiré phenomena

The moiré phenomenon or effect on a 3D display is different from the moiré phenomenon on a 2D display. In the 3D display, moiré phenomena are shifting as viewers changes his viewing positions. The moiré phenomena are different for different viewing angles [1-3]. This characteristic is one of the most important factors when viewing 3D images. The moiré phenomenon is one of the causes of the degradation of the image quality in the three-dimensional display and causes the crosstalk between neighboring viewing areas. Many methods have been developed to minimize the moiré phenomenon but they are mainly grouped into two such as 1) slanting or rotating the VZFO (Viewing Zone Forming Optic) line pattern, 2) adding a diffuser between the panel and the VZFO [1-4] –[1-7].

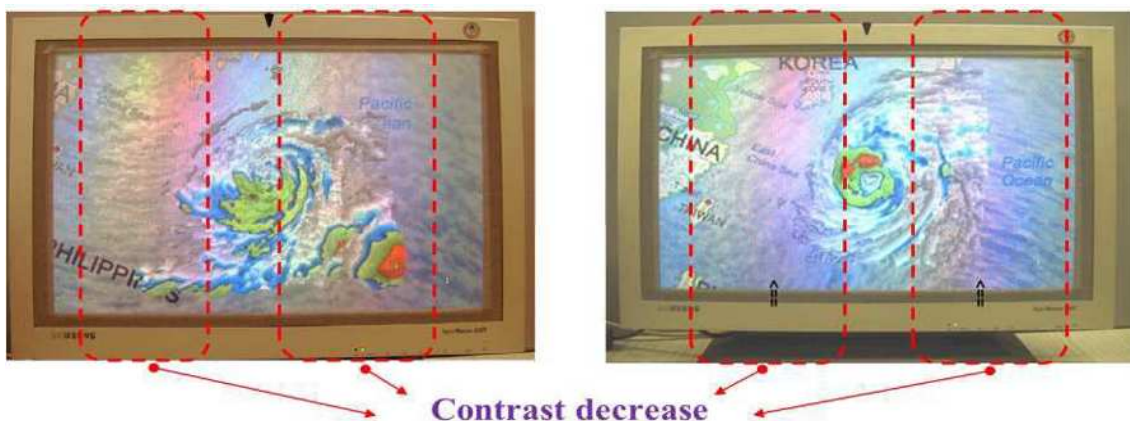


Fig. 1-4. Examples of Moiré pattern

## 1.2 Objective & Outline

The purpose of this thesis is to find out the characteristics of moiré in 3D display and verify it through developed simulation. For this purpose, this thesis is divided into 4 stages as follows: 1) study of moiré geometry and color characteristics in 3D displays, 2) mathematical representation of moiré in 3D display, 3) verification of moiré through developed moiré simulation, 4) to find optimization of moiré reduction method in 3D displays.

In 3D display, geometrical concepts, mathematical expressions, experiment and verification using VZFO, and verification with simulator were performed for the study of moiré geometry characteristics. This study explains the relationship between moiré phenomenon and VZFO in 3D display, and defines the characteristics caused by it. This research process was introduced in Chapter 2. We define basic Moiré characteristics in 3D display and study color characteristics using them. Also, we study the phenomenon of moiré that visual phenomenon according to color combination appears according to the characteristic of VZFO in 3D display. More specifically, the color representation in a typical display is determined by the R, G, and B constituting the pixel. In addition to this element, the 3D display also causes other characteristics such as the space of pixels and pixels, and the space between the display and VZFO. In this process, we express a new formula for calculating moiré. This research process was introduced in chapters 3 and 4 as basic principles, mathematical expressions, experiments, and verification through simulation. In this study, the characteristics of moiré phenomenon occurring in 3D display are defined, and mathematical expressions are verified through experiments. In Chapter 5, we simulate the characteristics of slanted color moirés at various angles( $0^{\circ}$ ~ $45^{\circ}$ ) in IP-type 3-D displays. We define the angle at which moiré minimization is achieved through experimental verification. Finally, we find a method of minimizing the moiré phenomenon through simulation technology. All of these processes are intended to prevent degradation of image quality caused by moiré phenomenon in 3D display, and at the same time to create an optimal viewing environment. Therefore, chapter 6 describes general image quality definitions for 3D displays, a description of a typical 3D display scheme, the formation of VZFO, and future perspectives.

## 2 Behaviors of moiré fringes induced by plate thickness

### 2.1 Introduction

Moiré is a common physical phenomenon appearing whenever two regularly patterned plates are superposed together [2-1]. The physical reasons behind the moirés are the difference between the pattern periods of the two plates. I.e., the moiré fringes are induced by beating between periods of the two patterns. The behaviors of the moiré fringes induced by this beating process can be easily predicted by cosine approximation of two grating patterns. In this prediction, it has always been assumed that the thickness of each of the two plates is negligible. Hence the number and position of moiré fringes for a given plate length and the fringe periods are fixed without regarding to viewers' viewing position, viewing distance and viewing angle change. Furthermore, the minus or plus difference between periods of two plate patterns has no role in the moiré fringe behavior. It can show only static moiré fringes. However, when the top plate has a thickness, the moiré fringe behaviors are completely different from the negligible thickness case. The thickness induces moiré fringe shifting, and changes in number of moirés fringes within a given plate length and period of each fringe when a viewer changes his/her viewing position, viewing distance and viewing angle of seeing the moiré fringes. And also, minus or plus difference resulted when the pattern period of one plate is subtracted from that of the other shows opposite moiré fringe behaviors, i.e., the periods and numbers of the moiré fringes are continuously either increasing or decreasing depending on the minus or plus difference as the viewing angle increases. This means that the moiré fringes are chirped. These moiré fringe behaviors have not been known so far and no moiré fringe descriptions found in metrology [2-2]-[2-4] and security [2-5]-[2-7] areas which have been known as the main application areas of moiré phenomenon, describe them. This is probably because it is necessary to have two patterned plates with one of them having a uniform thickness that can induce a comparable change in period of the other plate pattern, to observe the chirped moiré fringes. The gap effect which deals the moiré fringes when two regularly patterned plates are distanced with a certain air gap between them [2-8], [2-9], can be a special case of the thickness. In fact, the most of the moiré applications in metrology has basically the same set-up as the gap effect because it has the form of seeing a fringe pattern through a known grating pattern. The effect will be the case when refractive index of the top plate equals to 1.0. However, the gap effect has been known as producing only visual device dependent

moiré fringes which have no relationship with viewing angle and position at a given viewing distance, refractive index of the top plate and the minus or plus difference between two plates.

These moiré fringe behaviors can be explained by considering that the bottom plate pattern is chirped as the moiré fringes. In fact, the period of the line pattern in the bottom plate is virtually shortened by the thickness of the top plate because it is viewed through the top plate. When the top plate has a thickness, the bottom plate pattern will be refracted toward to the viewer by the top plate to appear at the pattern surface of the top plate. Since the amount of the shortening increases as the viewing angle increases and the refractive index of the top plate decrease, the period of the bottom plate pattern at the patterned surface reduces as the viewing angle increases. This means that the bottom plate pattern is chirped. The mixing of chirped and regularly spaced patterns creates a chirped moiré fringe. Since the viewing angle depends on viewing distance and viewing position, the period variation of the chirped pattern depends also on viewing distance and position. The period of the bottom pattern is varying with the changes in viewing angle, and viewing distance and position. This explains that why the moiré fringes are shifting. This is because the relative phase difference between two patterns changes as the viewing position changes.

The example of two superposed regularly patterned plates with the top plate having a thickness can be found in contact-type 3-D displays [2-10], though the thickness of the top plate has never been considered in analyzing moiré fringes in the displays [2-11], [2-12]. Since the increasing size and resolution of the displays result in a larger viewing angle of viewing displayed images at a closer distance from them, it will be necessary to know exactly the properties of the moiré fringes in these displays to develop more effective methods of reducing them in future.

The two-plate structure as in the 3-D displays was used to measure refractive index of the top plate material [2-13]. In this approach, the top plate is separated into two parts of the pattern part and the thickness part and then the thickness part is replaced by the material to be measured. The refractive index of unknown material is estimated by comparing the amount of moiré fringe shifting between the unknown and a reference.

In this paper, the presence of chirped moiré fringes in two superposed regularly patterned plates with one of the plates having a uniform thickness are identified, the theoretical ground of leading the chirped moiré fringes is developed and effectiveness of the theoretical ground is verified by experiments.

## 2.2 Theoretical ground of leading chirped moiré fringes

When two regularly patterned plates are superposed, the moiré fringes are induced by the beating between the pattern periods of the two plates. Hence the period of a moiré fringe,  $\delta_m$  is given as (2-1),

$$\delta_m = \left| \frac{\delta_T \delta_B}{\delta_T - \delta_B} \right| \quad (2-1)$$

Where  $\delta_T$  and  $\delta_B$  are pattern periods of top and bottom plates, respectively. Eq. (2-1) indicates that the moiré fringe period will be increased as the difference between  $\delta_T$  and  $\delta_B$  becomes smaller. However, they can hardly be equal due to misalignment, tolerances in pattern periods and uniformity of the patterns. Figure 1 shows the viewing geometry of two superposed regularly patterned plates when the top plate has a thickness  $t$ . The circular dots in top plate and square dots in bottom plate represent the regular patterns in them. The geometry is drawn as if a viewer watches the plate at right edge of the plate at the distance  $z_V$  to simulate a large size display panel. When a viewer at distance  $z_V$  from the top plate watches the bottom plate, i.e., the panel through the top plate, i.e., viewing zone forming optics (VZFO) having a thickness  $t$ , the panel pattern will be looked on the patterned surface of the VZFO by refraction effect as shown in Figure 2-1.

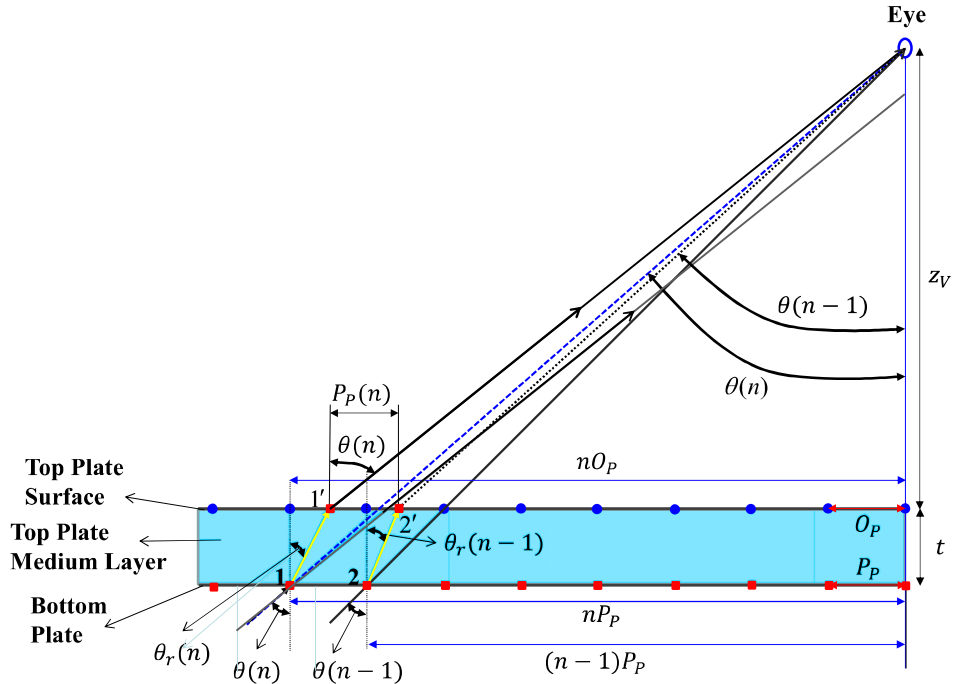


Fig. 2-1. Optical geometry of viewing two superposed regularly patterned plates

By this refraction effect, the patterns 1 and 2 of the panel are viewed as if they are patterns 1' and 2' in the patterned surface of the VZFO. Hence the VZFO and panel patterns are superposed at the patterned surface of the VZFO and create moiré fringes. The positions of patterns 1' and 2' will be found from the fact that the incidence angle of a ray to a flat object is equal to the exit angle of the ray from the object. However, this fact allows finding 1' and 2' only numerically. However, a more simple way is the following because of  $t \ll z_V$ : When there is no VZFO,  $n^{th}$  panel pattern from the right edge, specified by 1 will be viewed with the viewing angle  $\theta(n) = \tan^{-1}\{nP_p/(z_V + t)\}$  at the left edge of the panel, where  $P_p$  is the period of the line pattern on the panel.  $P_p$  is the same as  $\delta_B$  in Eq. 1.  $nP_p$  represents length of the panel. When the VZFO is on the panel, the panel pattern is refracted by the medium layer of the VZFO and viewed together with the VZFO pattern at the patterned surface of the VZFO. The refraction angle of pattern 1 will be given as  $\theta_r(n) = \sin^{-1}\{\sin \theta(n)/m_0\}$ , where  $m_0$  is the refractive index of the VZFO. Hence pattern 1 will appear at the position of pattern 1' on the patterned surface of the VZFO. Likewise pattern 2 at 2'. The distance of pattern 1' from the right edge will be given as  $nP_p - t \tan \theta_r(n)$ . Viewers' eyes perceive pattern 1' instead of  $n^{th}$  line pattern of the panel. Since  $(n-1)P_p - t \tan \theta_r(n-1)$  is the perceived position of the  $(n-1)^{th}$  line pattern in the panel,  $P_p(n)$  will be calculated as,

$$P_p(n) = P_p - t\{\tan \theta_r(n) - \tan \theta_r(n-1)\} \quad (2-2)$$

In Eq. (2-2),  $\tan \theta_r(n-1)$  is 0 when  $n = 1$ . Figure 2 depicts  $P_p/P_p(n)$  values for two cases of  $n = 1$  to  $n_{max}$  and  $n = 1$  to  $n_{max}$  for the three different  $z_V$  values of 0.7 m, 1.0 m and 2.0 m. A polycarbonate that has a refractive index of 1.589 at wavelength of 555 nm [14] is assumed as the VZFO medium. The pattern period of the VZFO is 3.406 mm for  $n_{max}$  and 1.28 mm for  $n_{max}$ .  $n_{max}$  and  $n_{max}$  correspond to  $nO_p$ , i.e., VZFO lengths of 1.032 m and 0.8m, respectively. These lengths represent the maximum sizes of available lenticular plates for the experiment.

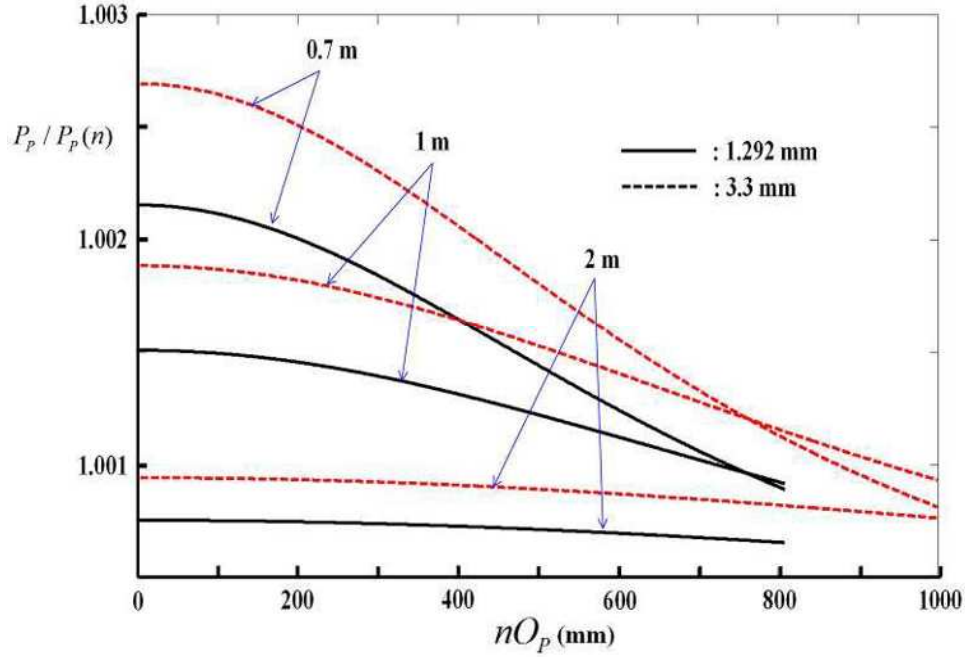


Fig. 2-2. Graphical representation of calculated  $P_p/P_p(n)$  values

For this reason, the abscissa of Figure 2 represents  $nO_p$  from right most edge to left most edge. The period  $P_p$  and the medium thickness  $t$  are assumed as 3.3 mm and 3 mm, respectively for  $n = 1$  to 303 case, and as 1.292 mm and 2.4 mm, respectively, for  $n = 1$  to 607 case. These values are chosen by the availability.  $P_p/P_p(n)$  is the inverse value of the normalized  $P_p(n)$  values by  $P_p$ . Each line in Figure 2 represents the line frequency variation in each corresponding panel pattern, i.e.,  $f_0 = 1/P_p$ .  $f_0 = 1/P_p$  will be modulated by each  $P_p/P_p(n)$  line. Figure 2 informs that 1) the line frequency reduces continuously as the viewing angle increases, 2)  $P_p(n)$  values are always smaller than  $P_p$  but the differences between them reduce as  $z_v$  increases, 3)  $P_p(n)$  becomes closer to  $P_p$  as  $n$  increases for all  $z_v$  values and 4) the difference between  $P_p$  and  $P_p(n)$  is less than 0.3%. This information indicates that  $P_p(n)$  value, i.e., the period of the panel pattern is chirped. The panel line pattern with a uniform period turns visually to the line pattern with continuously increasing period for all  $z_v$  values. The small difference between  $P_p$  and  $P_p(n)$  indicates almost no chirping for small  $n$  values but the chirping will be more visible as  $n$  becomes larger because the accumulated difference to the large  $n$  values increases as  $n$  increases. This means that the chirped moiré fringes can be observed for a large size panel. The line pattern with continuously increasing or decreasing period is considered as a chirp pattern. This chirp pattern can be mathematically expressed as  $2\pi f_0 s(x)$ , where  $f_0$  represents  $1/P_p$  and  $s(x) = P_p/P_p(n)$  or  $(O_p/O_p(n))$  the

chirp modulation function leading the chirp pattern, as specified by each line in Figure 2.  $s(x)$  is expressed by a 12th order polynomial to faithfully retrace the chirp modulated pattern with use of MATLAB. Since the phase of the oscillating signal is given by the integral of the frequency function, the mathematical expression of chirped oscillation,  $S(x)$  is given as (2-3),

$$S(x) = \cos\{\phi_0 + 2\pi f_0 \int_0^x s(x) dx\} \quad (2-3)$$

In Eq. 2-3,  $\phi_0$  is the initial phase at  $x = 0$ . When the VZFO and panel are superposed together, if  $O_p (= \delta_T)$  is the period of the VZFO, the moiré fringes  $f_m$  can be expressed as [2-12],

$$f_m = \frac{1}{2} \{1 + \cos(\omega_p x)\} - [1 + \cos\{\omega_o(x + \Delta x)\}] \quad (2-4)$$

Where  $\omega_o$  and  $\omega_p$  are spatial frequency of the VZFO and panel patterns, respectively,  $\Delta x$  is the difference between starting lines of the VZFO and panel patterns and  $\omega_o \Delta x = \phi_0$ .  $\omega_o$  and  $\omega_p$  are represented as  $\omega_o = 2\pi f_o (= 1/O_p)$  and  $\omega_p = 2\pi f_p (= 1/P_p)$ , and  $\Delta x$  is smaller than  $O_p$  in Eq. 4. When  $t \neq 0$ ,  $\Delta x$  will vary as viewers change their viewing positions because of relative phase changes between  $O_p$  and  $P_p(n)$ . This explains the moiré fringe shifting as viewers change their viewing positions. Eq. (2-3) is further reduced as [16],

$$f_m = \frac{1}{2} [\cos \frac{1}{2} \{(\omega_o - \omega_p)x + \omega_o \Delta x\} + \cos \frac{1}{2} \{(\omega_o + \omega_p)x + \omega_o \Delta x\}]^2 \quad (2-5)$$

Eq. (2-4) indicates that moirés are created by two cosines with periods  $2O_p P_p / (O_p - P_p)$  and  $2O_p P_p / (O_p + P_p)$ , respectively, because  $\omega_o - \omega_p$  and  $\omega_o + \omega_p$  in Eq. (2-4), are expressed as  $2\pi / \{O_p P_p / (O_p - P_p)\}$  and  $2\pi / \{O_p P_p / (O_p + P_p)\}$ , respectively. Since the difference between  $O_p$  and  $P_p$  is small,  $2O_p P_p / (O_p - P_p)$  will be much bigger than  $2O_p P_p / (O_p + P_p)$ . This means that the envelopes of the moiré fringes are defined by the 1st cosine term but the local variations are defined by the 2nd cosine term in Eq. (2-4). Hence the moiré fringe periods will be defined by the 1st cosine term. Hence the beat period defined in Eq. (2-1) represents the moiré fringe period. Furthermore, the second cosine reveals that the moiré fringe's local variation has the period close to the pattern period because  $2O_p P_p / (O_p + P_p)$  can be reduced to either  $O_p$  or  $P_p$  due to their small difference compared with their actual values. By combining Eqs. (2-3) and (2-4),  $f_m$  is rewritten as,

$$\begin{aligned} f_m &= \frac{1}{2} \{1 + S_p(x)\} - [1 + \cos\{\omega_o(x + \Delta x)\}] \\ &= \frac{1}{2} [1 + \cos\{\omega_p \int_0^x s_p(x) dx\}] - [1 + \cos\{\omega_o(x + \Delta x)\}] \end{aligned} \quad (2-6)$$

When both the VZFO and panel patterns are made to contact each together, both of them will be viewed through the VZFO medium. In this case, the moiré fringes can be expressed as,

$$f_m = \frac{1}{2} [1 + \cos\{\omega_P \int_0^x s_P(x) dx\}] \cdot [1 + \cos\{\omega_O \Delta x + \omega_O \int_0^x s_O(x) dx\}] \quad (2-7)$$

In Eqs. (2-6) and (2-7), subscripts  $P$  and  $O$  represent  $s(x)$  for panel and VZFO line patterns, respectively. The polynomial expression of  $s(x)$  has the following form;

$$s(x) = \sum_{i=0}^j a_i x^i \quad (2-8)$$

This  $j^{th}$  order polynomial should retrace very faithfully the  $P_P(n)$  curves of the line patterns and thicknesses employed in this manuscript. In Eq. (2-8),  $a_i (i = 1 \text{ to } j)$  represents constants. The integral form of the  $s(x)$  is given as,

$$\int_0^x s(x) dx = \int_0^x \sum_{i=0}^j a_i x^i dx = \sum_{i=0}^j \frac{a_i}{i+1} x^{i+1} \quad (2-9)$$

By substituting Eq. (2-9) to Eq. (2-6) or (2-7), moiré fringes for different combinations of thicknesses and periods can be estimated.

### 2.3 Moiré fringe simulation

Since the lenticular plates having near 1m length are available for us only for  $O_P = 1.27$  mm and  $O_P = 3.406$  mm cases, moiré fringes described by Eqs. (2-6) and (2-7) are calculated for two cases of 1)  $O_P = 1.27$  mm,  $P_P = 1.292$  mm and  $t = 2.4$  mm, and 2)  $O_P = 3.406$  mm,  $P_P = 3.3$ mm and  $t = 3.0$  mm for the three  $z_V$  values of 0.7 m, 1 m and 2 m. The 1st case is for  $P_P > O_P$  and the 2nd for  $P_P < O_P$ . In both cases, the calculations are compared with that from  $t = 0.0$  mm case. Other parameter values are the same as in Figure 2. A 12th order polynomial, i.e.,  $j = 0$  to 12 is used to retrace  $P_P(n)$  for the specified VZFO lengths. It is expected that the number of moiré fringes will increase with increasing  $z_V$  values for  $P_P > O_P$  case but decrease for  $P_P < O_P$  case. In other word, the period of the moiré fringes decreases continuously with increasing  $z_V$  values for  $P_P > O_P$  case but increases continuously for  $P_P < O_P$  case. This is because  $P_P(n)$  becomes smaller as  $z_V$  value decreases due to increasing  $\theta(n)$  values. As  $P_P(n)$  decreases, the differences between  $O_P$  and  $P_P(n)$  decrease for  $P_P > O_P$  but increase for  $P_P < O_P$ . According to Eq. (2-1),  $\delta_m$  will increase for  $P_P > O_P$  but decrease for  $P_P < O_P$ . Hence the number of moiré fringes will be smaller for smaller  $z_V$  values. For  $P_P > O_P$ , the number is smaller than that of  $t = 0.0$  mm case for all  $z_V$  values. Furthermore, the periods of moiré fringes are continuously reduced as the distance from viewers increases because  $P_P(n)$  becomes closer to  $P_P$ . For  $P_P < O_P$ , the trend is opposite to  $P_P > O_P$  case, i.e., the number of moiré fringes will be larger for smaller  $z_V$  values

and it is always larger than  $t = 0.0$  mm case. Furthermore, the periods of moiré fringes increase continuously as the distances from viewers increase. The differences in moiré fringe characteristics between  $t = 0.0$  mm and  $t \neq 0.0$  mm cases will be diminished as  $z_V$  increases for both  $P_p > O_p$  and  $P_p < O_p$  cases. Figure 2-3 shows the results when the plate width is considered as 810 mm for  $P_p > O_p$  case and 1,000 mm for  $P_p < O_p$  case. The moiré fringes are calculated by assuming that viewers are seeing the moiré fringes at right most edge and at the mid-position of the VZFO plate, respectively. The moiré fringe periods are determined by the  $\omega_O - \omega_P$  term in Eq. (2-2). The distances between two white broken lines and arrows with two tip lines represent the 1st moiré fringe period from the right edge.  $\delta_m$  is approximately calculated as 74.58mm and 106.04mm for  $P_p > O_p$  and  $P_p < O_p$  cases, respectively, for  $t = 0.0$  mm.  $\delta_m$  indicates that the total number of moiré fringes for  $P_p > O_p$  and  $P_p < O_p$  cases are 10.86 and 9.43, respectively. When  $O_p$  plate has a thickness,  $P_p$  plate will be seen through the  $O_p$  plate. The total numbers of moiré fringes for  $P_p > O_p$  case, are calculated as 9.83, 10.08 and 10.41, and for  $P_p < O_p$  case as 9.98, 9.88 and 9.69 for  $z_V$  0.7 m, 1 m and 2 m, respectively, according to Eq. (2-3) and the first cosine term of Eq. (2-5). These numbers are different from those of  $t = 0.0$  mm cases. For the given plate widths, the period ratios of the last and first fringes for  $z_V$  values of 0.7 m, 1 m and 2 m are (78.9 mm/88.07 mm = 0.91), (80.28 mm/83.62 mm = 0.96) and (77.6 mm/78.0 mm = 0.994), respectively, for  $P_p > O_p$  case, and (103.34 mm/97.73 mm = 1.057), (102.99 mm/100.03 mm = 1.030) and (103.53 mm/102.92 mm = 1.006), respectively, for  $P_p < O_p$  case.

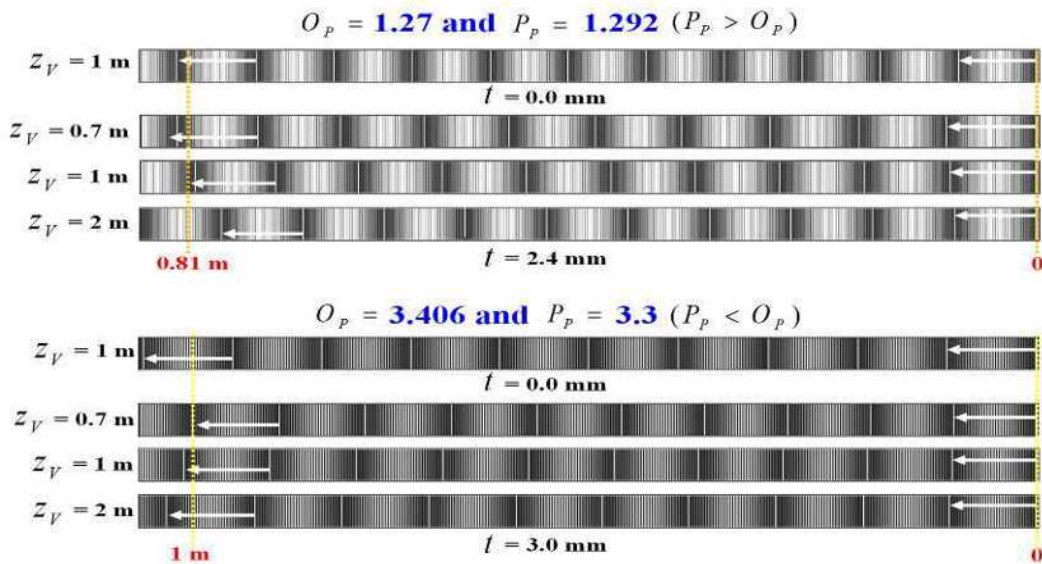
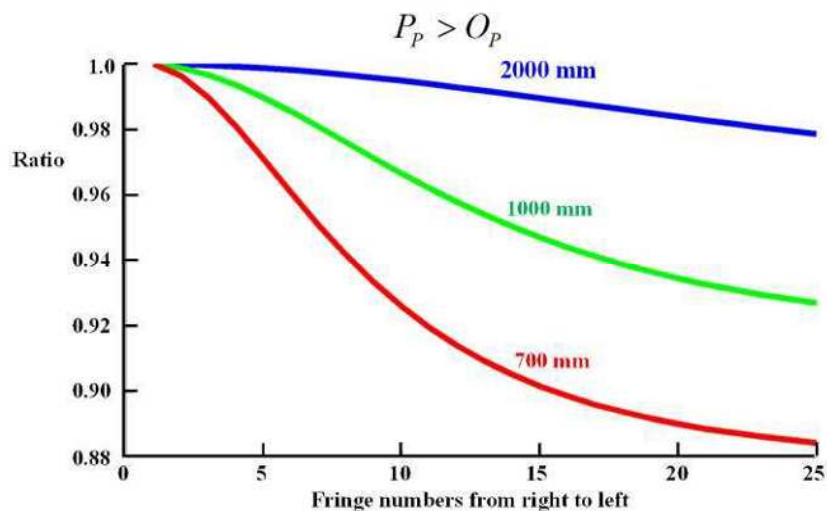


Fig. 2-3. Simulated moiré fringes for two cases

The periods are longer for  $P_p > O_p$  case and shorter for  $P_p < O_p$  case than the static cases, but the periods become nearly the same as those for the static as  $z_V$  increases. The ratios indicate that the chirped variations will be intensified for smaller  $z_V$  values. This is shown in Figure 3. The periods of moiré fringes decrease more for  $P_p > O_p$  case and increase more for  $P_p < O_p$  case as away from the right edge of the moiré fringes, though the chirped variations are noticed from 6th fringe from the right edge for both 0.7 m and 1.0 m for both  $P_p > O_p$  and  $P_p < O_p$  cases. The period ratios of the left most and right most moiré fringes for  $z_V = 0.7$  m is approximately 0.93 and 1.05 for  $P_p > O_p$  and  $P_p < O_p$  cases, respectively. These variations induce the moiré fringes to shift to the right side for  $P_p > O_p$  case and to the left side for  $P_p < O_p$  case as  $z_V$  increases. The moiré fringes are chirped, except  $t = 0.0$  mm case. For  $t = 0.0$  mm case, moiré fringes are having a constant period for both cases. For the case of 2 m, the period variations are hardly noticed for the calculated plate sizes. This is because the difference between  $P_p$  and  $P_p(n)$  for 2 m is smallest among the three  $z_V$  values. In fact,  $P_p/P_p(n)$  value for the given distance and thickness values cannot exceed 1.001 as shown in Figure 2-2. Figure 2-4 shows the period ratio of 1st moiré fringe to following fringes for three different  $z_V$  values in both cases. The ratio is calculated up to 2 m. It is obvious that the ratios are continuously decreasing as the numbers increases for  $P_p > O_p$  case but increasing for  $P_p < O_p$  case. The decreasing and increasing rate is highest for  $z_V = 0.7$  m. For the 2 m case in both cases, the ratios are close to 1 for the calculated plate sizes in Figure 2-3. Figure 2-4 shows clearly that the moiré fringes are chirped.



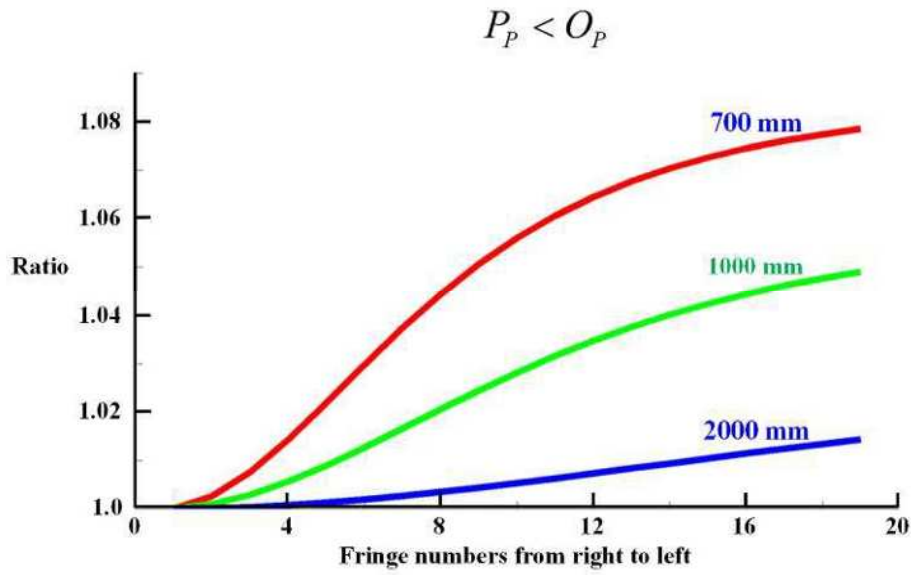


Fig. 2-4. Calculated period ratio of 1st moiré fringe to following fringes for three different  $z_V$  values in both cases. The number in each line represents  $z_V$  value.

## 2.4 Experimental results

To verify the simulation results, two moiré experimental sets having the same parameters as in simulation are prepared as in the simulation. For both experimental sets, line printed papers with corresponding  $P_P$  values are used for the bottom plates for the demonstration purposes. However, for the VZFO, a lenticular plate with 1.27 mm pitch, 2.4 mm thickness and  $200\mu\text{m}$  lens height, and a line printed plastic sheet with 3.4mm interval, glued on a plastic plate with thickness 3mm are used. Both the lenticular and the plastic plate are made of the polycarbonate mentioned in Figure 2-2. The lengths of the lenticular plate and the plastic plate are 0.81 m and 1.0 m, respectively. Photographs of moiré fringe patterns are taken with Nikon D700 camera with Sigma's wide-angle objective DG HSM which has a nominal field of view angle of  $122^\circ$ . The optical axis of the camera is aligned at both right edge and mid-position of the top plates to show moiré fringe shifting with the viewing position changes for three  $z_V$  values of 0.7 m, 1 m and 2 m. The minimum value of the photographing distance is set to 0.7 m because the Sigma objective can cover the plate length 1.0 m at 0.7 m owing to its wide field of view angle. Since the printed line patterns and lenticular plate can have different line widths from their nominal values, the line periods in section 3 are determined by counting the total numbers of lines within their specified lengths. Reference

lines are drawn with 100 mm interval on the printed paper for two purposes; one is to compensate the contraction of images which are away from the center of the wide-angle objective, and the other is to align moiré fringes from different  $z_V$  values. The reference lines can allow estimating the image contraction at larger viewing angles caused by the wide-angle objective. The contractions in each 100 mm interval will inform the amount of the compensations that should be given to the image portions of the interval. The contractions will appear more for smaller viewing distances because of larger viewing angles for a given plate lengths. The experimental sets are placed between glass plates to minimize the bending of top plates and crumples in the printed papers. This is shown in Figure 2-5. The optical axis of the camera is focused to the right edge of the top plate by making the axis in parallel to the normal direction of the top plate. For the center view the camera axis is aligned to the normal direction. Since the moiré fringes are formed in the pattern surface of the top plate, the glass plate doesn't affect the results. Figures. 2-6 and 2-7 show the experimental results of  $P_p > O_p$  and  $P_p < O_p$  cases, respectively, when the camera is centered at the right most edge of the VZFO. Furthermore, 1) the first dark moiré fringe in the right side and the reference lines in different moiré fringes are aligned in a line for the comparison with the simulation results in Figure 2-3, 2) the arrows and solid bars represent the period of the 1st moiré fringe and the distance (10 cm) between 1st and 2nd reference lines from the right most side of each moiré fringe, respectively, 3) the white broken lines represent the center of each dark fringes in each moiré fringe pattern. These lines are to ease the bad contrast problem of Figure 2-7, 4)  $t = 0.0$  mm is achieved by contacting lens array side of the lenticular plate to the printed paper and 5) the lens height is neglected because the moiré fringe pattern doesn't affect by the lenses with  $200\mu\text{m}$  height. Figure 2-6 reveals that the numbers of moiré fringes are 10.9, 9.90, 10.20 and 10.40 for  $z_V$  values of 0.7 m, 1.0 m and 2.0 m, respectively. The differences between these numbers are 0.1 for all  $z_V$  values. These differences are just within 1% of the numbers. The moiré fringes are shifting more to right side with increasing distances. For  $P_p < O_p$  case, the numbers of moiré fringes are 9.3, 10.0, 9.80, 9.60 for  $z_V$  values of 0.7 m, 1.0 m and 2.0 m, respectively, as shown in Figure 2-7. The moiré fringes shift more to the left side as  $z_V$  increases and the numbers of moiré fringes are the same for the simulation for  $z_V = 0.7$  m, and less than 0.1 for  $t = 0.0$  mm, and  $z_V = 1$  m and 2 m. As in  $P_p > O_p$  case, the difference is within the error range. This means that Eqs. (2-2) and (2-7) are correct expressions for the virtual changes in the line periods of the bottom plate patterns and moiré fringes, respectively. Figures. 2-6 and 2-7 also show that the moiré fringes are chirped, especially for  $z_V = 0.7$  m case. The moiré fringe periods decrease for Figure 2-6 and increase for Figure 2-7 as

away from the right edge.

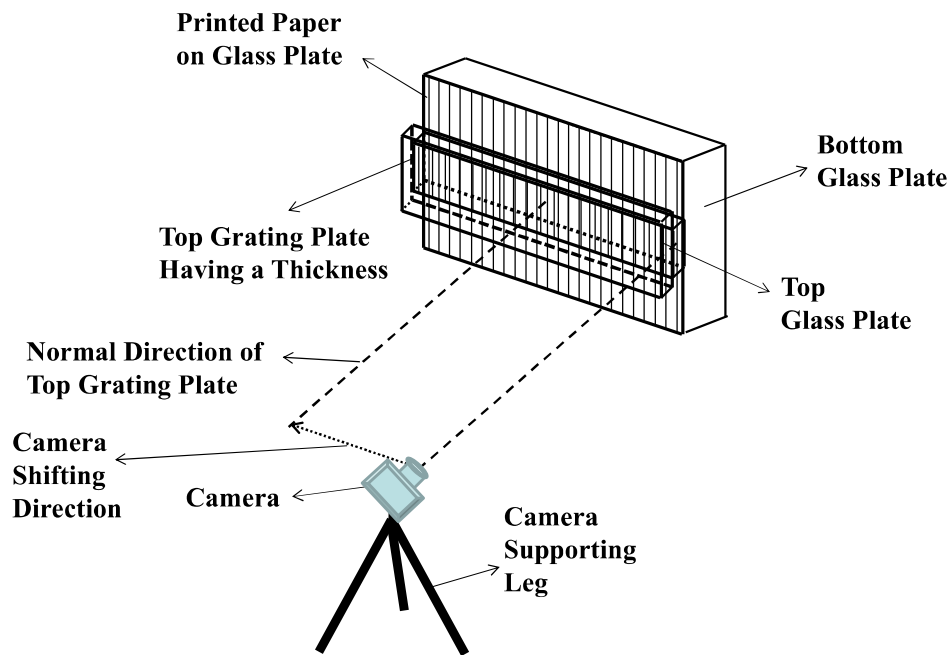


Fig. 2-5. Experimental set-up

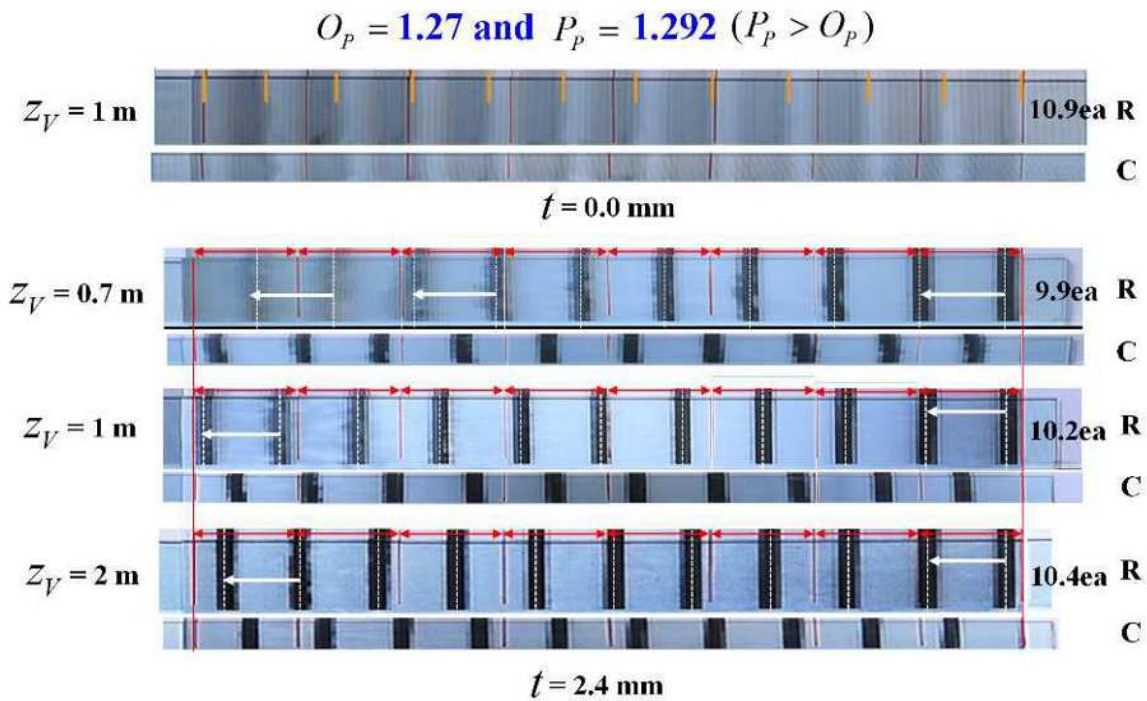


Fig. 2-6. Experimentally obtained moiré fringes for  $P_p > O_p$  case

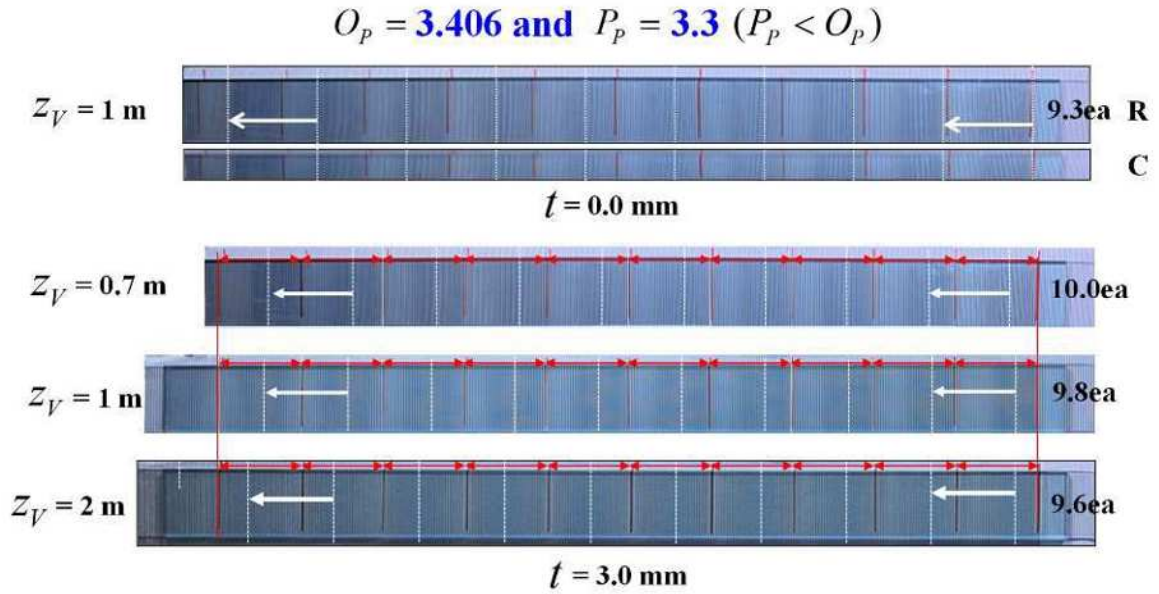


Fig. 2-7. Experimentally obtained moiré fringes for  $P_p < O_p$  case

These chirped variations are clearly noticed from 7th fringe for both figures at  $z_V = 0.7$  m. However, the variation is noticed from 6th fringe in the simulation in Figure 2-3. They have only one fringe difference. This difference is probably caused by the difficulties in defining the period of each fringe in the moiré fringes. The viewing angle corresponding to the 7th fringe is  $41.4^\circ$  ( $\tan^{-1}((88.07 \times 7)/700)$ ) and  $44.3^\circ$  ( $\tan^{-1}((97.73 \times 7)/700)$ ) for  $P_p > O_p$  and  $P_p < O_p$  cases, respectively. For  $z_V = 1.0$  m, the chirped variation is noticed from the left most fringe in the cases. So the viewing angle is given as  $39.0^\circ$  ( $\tan^{-1}(810/1000)$ ) and  $42.6^\circ$  ( $\tan^{-1}(918/1000)$ ): there are 9.8 fringes) for  $P_p > O_p$  and  $P_p < O_p$  cases, respectively. Since the viewing angles for  $z_V = 1.0$  m are smaller than those of  $z_V = 0.7$  m for the simulation, the chirped moiré fringes will always be observed when the viewing angle is more than  $44.3^\circ$  for the parameters used in this paper. However more thorough studies are required to formulate the angle with parameters responsible for the chirped moiré fringes. The white arrow in the left most fringe represents the right most fringe period. The rates of increasing and decreasing become smaller as  $z_V$  increases. For the case of  $z_V = 2$  m, the chirped moiré fringes are evidenced only at the left most fringes as shown in Figure 2-3. Figures 2-6 and 2-7 are not different from Figure 2-3. It shows exactly the same moiré fringe behaviors as shown in Figure 2-3. It clearly demonstrates that the moiré fringes are chirped. The period ratios of

the last and first fringes for  $z_V$  values of 0.7 m, 1 m and 2 m are given as 0.92, 0.96 and 0.98, respectively, for  $P_p > O_p$  case, and 1.055, 1.03 and 1.0, respectively, for  $P_p < O_p$  case. These ratios are almost the same as their corresponding cases as in Figure 2-3. The mid-position view of the moiré fringes for each  $z_V$  is also shown in Figure 2-6. “R” and “C” represents right most edge and the mid-position cases, respectively. They demonstrate that the moiré fringes are shifting as viewers change their viewing positions when the top plate has a thickness. No shifting is seen for  $t = 0.0$  mm. It appears that the shifting is more for larger distances. The maximum possible shifting will be a fringe period. Due to the shifting, all moiré fringes have the same number of dark fringes. Figures 2-6 and 2-7 clearly indicate that the chirp type period variation of the bottom plate pattern induces chirped moiré fringes which have different fringe numbers with varying viewing angles. The chirp type variation is brought by the thickness and the refracted index of the top plate, though their variation becomes lesser as the viewing distance increases. The fringes don't disappear even at large viewing distance.

## 2.5 Conclusion

Two superposed regular patterned plates can create chirped moiré fringes when the top plate has a thickness. The chirped moiré fringes are shifting as viewer's change his/her viewing position and the chirped period variations will be more or less as the viewing distance and/or viewing angle increases/decreases. These chirped moiré fringes are created because the bottom plate pattern is viewed through the top plate. The bottom pattern is refracted when it is going through the top plate to appear at the pattern plane of the top plate and its uniform period changes to a chirped period due to the refraction. The mixing between the regular top plate pattern and the chirped pattern produces a chirped moiré fringe. The chirping in moiré fringes becomes more noticeable as the viewing angle increases and the viewing distance decreases. Since the viewing angle depends on both viewing distance and the plate length, it increases as the plate length increases for a given viewing distance. At a large viewing distance, the moiré fringes can no longer show their chirped variations due to the diminished viewing angle.

The chirped moiré fringes can be used to measure the refractive index of materials and applied for anti-counterfeit because it is very sensitive to any modification.

## 3 Color moirés in contact-type three-dimensional displays

### 3.1 Introduction

Color moirés are one of hostile phenomena appearing at contact-type three-dimensional (3-D) imaging such as multiview and light field imaging equipped with a VZFO for viewing zone forming [3-1] - [3-4]. The problem is that they can be hardly eliminated because the imaging requires structurally a VZFO which should be superposed on a display panel. This structure will induce color moirés because the panel pattern can be approximated as a two-dimensional periodic colored line grid pattern by the pixel arrangement and the VZFO either a two- or one-dimensional periodic line pattern due to the boundaries between elemental lenses in lenticular and microlens array, and the periodic line array in parallax barrier [3-5]. The moirés have been considered so far as a beating phenomenon occurring whenever two films with periodic line patterns are overlapped together with or without air gap between them [3-6]. The beating phenomenon requires that the difference between the pattern periods of the two films should be smaller than the pattern period of the film with the smaller period between two films [3-7]-[3-9]. However, in the contact-type 3-D and light field imaging, 1) the line period of the VZFO line pattern is typically more than several times of that of the pixel pattern, 2) there is a material gap between two patterns, determined by the combined thickness of VZFO material and the cover glass of the display panel, and 3) the panel pattern is not a simple grating but has a near continuous RGB color pattern lined by the boundaries of sub-pixels in the horizontal and pixels in vertical directions. These differences make the moirés in the contact-type 3-D imaging behave completely differently from those in two film patterns: Since the VZFO is made from one of several plastics [3-10], it has a refractive index close to that of the cover glass of the display panels. Due to the gap induced by the VZFO material and the cover glass, the pixel pattern on the panel cannot combined with the VZFO line pattern as in two films with regular line patterns but the panel pattern will be refracted by the gap materials before it is combined with the VZFO line pattern when viewers view the display. Since the panel pattern will be more refracted as the viewing angle increases, the pixel pattern that is away from the viewing position will be more refracted. Due to this refraction effect, the pixel period is virtually decreased as the pixel distance from the viewers' positions increases. Hence the panel pattern at the pattern plane of the VZFO line pattern will be virtually chirped. This chirped panel pattern is responsible for the chirped moirés in the contact-type 3-D imaging

[3-11] and the color moirés even for the case when the panel and VZFO line patterns have the same period. Since the viewing angle changes as the viewers' relative position to the panel and the viewing distance change, the chirping degree of the chirped pixel pattern also changes. Hence the color moirés are not static but show a dynamic behavior: They are shifting as the viewers' position and the viewing distance change. Due to the large period difference between the panel and VZFO line patterns, the period of the chirped color moirés cannot be calculated with the conventional beat frequency formula for moiré period calculation. A new formula of calculating the period is needed. The formula had been derived by considering that the color moirés are the result of periodic blocking of the chirped panel pattern the VZFO line pattern [3-12]. Since the panel pattern consists of a repeated arrangement of R(red), G(Green) and B(Blue) sub-pixels and there is a small gap between sub-pixels and between pixels, the panel looks white when all the pixels in the panel is On. In this case, if the VZFO line pattern blocks periodically a part of each sub-pixel, the color balance of the pixel pattern will be broken and consequently the panel is no longer white but periodically colored. When the line width of lines in the VZFO line pattern is larger than the pixel period, the color moirés will reveal periodically aligned dark lines with the colored lines. This periodical color pattern is the color moirés in the contact-type 3-D and light field imaging [2-13]. Since these color moirés are induced by the structural layout of the contact-type displays, they are inherent and cannot be eliminated completely unless the periodicity of one of the panels and VZFO line patterns becomes irregular. So, it is necessary to find the ways of minimizing them.

There is a couple of ways of reducing color moirés. One is slanting the lines in the VZFO line pattern to have a certain angle with the panel pattern [3-14]. In this case, the color moirés become almost invisible as the angle increases to around  $26^\circ$  for the lenticular case. Since this angle was obtained under the assumption that VZFO's line and the panel patterns have the same period, the angle is not proper for the contact-type displays. However, the angle is still effective for the displays because the color moiré becomes unclear as the angle increases due to the fact that the VZFO lines pass around 1.5 sub-pixels for a pixel height. Hence the sub-pixel color changes due to the blocking will be more insignificant and the unblocked parts of the sub-pixels look combined as a white color to viewers' eyes, especially when the line width is small than the sub-pixel width as in a lenticular. The slanting is a very effective method of minimizing moirés in lenticular plate as the VZFO, but it does not guarantee that the same angle works for the parallax barrier. This way of minimizing the color moirés will result increasing in the crosstalk between different view images at viewing regions of different view images. The other is inserting

a diffuser between VZFO and the panel [3-15]. The visible moirés are effectively reduced with the diffuser but it will reduce also the image sharpness and increases the crosstalk because of the pixel boundary diminishing by the diffuser. The moirés can be further reduced as the diffusing power of the diffuser increases. However, the image sharpness will be more reduced and the crosstalk more increased.

In this paper, the color moirés in contact-type three-dimensional imaging is reviewed for the case when the slanting angle of the VZFO line pattern is  $0^\circ$ . And some experimental results of color moirés for nonzero slanting angle are introduced and their behaviors are analyzed.

### 3.2 Parts of a manuscript

As described in introduction, the pixel pattern is represented as a two-dimensional (2-D) wire grid and the VZFO either a line grid or a two-dimensional (2-D) wire grid. To find the generalized expression of two overlapped 2-D wire grids, the VZFO is also treated as a 2-D wire grid. The mathematical geometry of two overlapped wire grids is shown in Fig. 3-1.

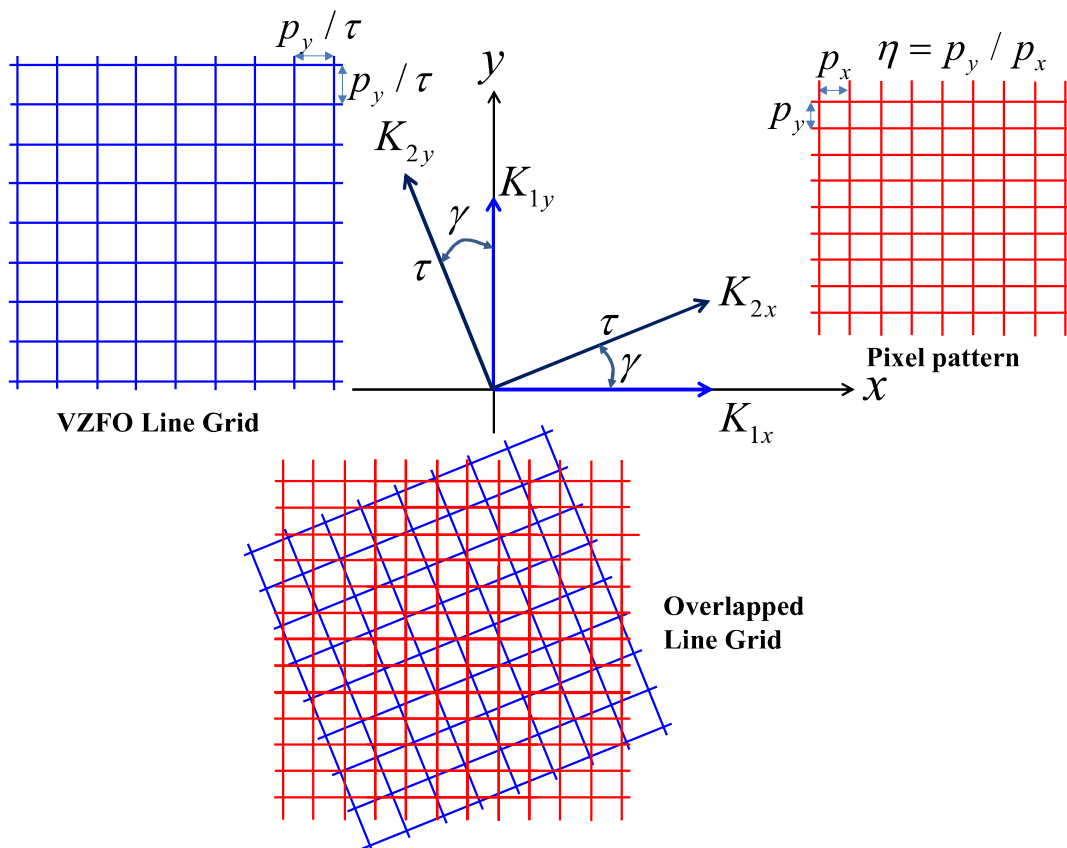


Fig. 3-1. Mathematical geometry of overlapped two grids of different dimensions.

When two wire grids are overlapped as in Fig. 1, the mathematical expression of them,  $M(x, y)$  is expressed as [3-16],

$$M(x, y) = c(1 + \cos \vec{K}_{1x} \cdot \vec{x})(1 + \cos \vec{K}_{1y} \cdot \vec{y}) \times (1 + \cos \vec{K}_{2x} \cdot \vec{x})(1 + \cos \vec{K}_{2y} \cdot \vec{y}) \quad (3-1)$$

In Eq. (3-1),  $c$  is a constant,  $\vec{K}_{1x(y)}$  and  $\vec{K}_{2x(y)}$  are the vector forms of wave numbers in  $x(y)$  direction for pixel and VZFO line patterns, respectively. They are given as  $\vec{K}_{1x(y)} = 2\pi/p_{x(y)}$  and  $\vec{K}_{2x(y)} = 2\pi/\tau p_{x(y)}$ , where  $p_x$  and  $p_y$  represents a pixel pitch in  $x$  and  $y$  directions, respectively,  $\tau$  the period ratio of VZFO line pattern to pixel pattern.  $\tau$  cannot be smaller than 1, because VZFO line period is bigger than the pixel period. In Fig. 1, the crossing angle  $\gamma$  cannot be bigger than  $45^\circ$  because the coordinate is symmetric along the  $45^\circ$  line. If the pixel aspect ratio is  $\eta$ , i.e.,  $\eta = p_y/p_x$ ,  $\vec{K}_{1x(y)} \cdot \vec{x}(y)$  and  $\vec{K}_{2x(y)} \cdot \vec{x}(y)$  are given as

$$\begin{aligned} \begin{pmatrix} \vec{K}_{1x} \cdot \vec{x} \\ \vec{K}_{1y} \cdot \vec{y} \end{pmatrix} &= k \begin{pmatrix} \eta & 0 \\ 0 & 1 \end{pmatrix} \begin{pmatrix} x \\ y \end{pmatrix} = \begin{pmatrix} \eta kx \\ ky \end{pmatrix} \quad \text{and} \\ \begin{pmatrix} \vec{K}_{2x} \cdot \vec{x} \\ \vec{K}_{2y} \cdot \vec{y} \end{pmatrix} &= \tau k \begin{pmatrix} \cos \gamma & \sin \gamma \\ -\sin \gamma & \cos \gamma \end{pmatrix} \begin{pmatrix} x \\ y \end{pmatrix} = \tau k \begin{pmatrix} x \cos \gamma + y \sin \gamma \\ -x \sin \gamma + y \cos \gamma \end{pmatrix}, \end{aligned} \quad (3-2)$$

Equation 2 requires that  $k = \frac{2\pi}{p_y}$  and  $0 < \eta$  and  $0 < \tau \leq 1$ . Hence  $\tau$  is smaller than  $\eta$ . When Eq. (3-2) is substituted to Eq. (3-1) and then simplifications are done with use of the following relationships

$$\begin{aligned} \cos(akx + bky) &= \cos\{\sqrt{a^2 + b^2}(\frac{a}{\sqrt{a^2 + b^2}}kx + \frac{b}{\sqrt{a^2 + b^2}}ky)\} \\ &= \cos\{\sqrt{a^2 + b^2}(\cos \varphi kx + \sin \varphi ky)\}, \end{aligned} \quad (3-3)$$

where  $\varphi = \tan^{-1}(b/a)$ .  $M(x, y)$  can be further simplified with use of the following relationships

$$\begin{aligned} x' &= x \cos \varphi + y \sin \varphi \\ y' &= -x \sin \varphi + y \cos \varphi, \end{aligned} \quad (3-4)$$

with these simplifications,  $M(x, y)$  can be expressed as (3-5)

$$M(x, y) = \sum_{n=1}^{41} c_n \cos(\sqrt{f_n(\tau, \gamma)} kx'(y')), \quad (3-5)$$

where  $f_n(\tau, \gamma)$  represents the multiplying factor to  $p_y$ , i.e., the pixel period in  $y$  direction to define the moiré period in the direction  $x'(y')$ . So, each of  $f_n(\tau, \gamma)$  defines moirés of various frequency components. This means

that the moirés appearing at the contact-type 3-D imaging are created by multiple interferences among waves of different periods and directions. According to Eq. (3-5), the moirés are composed of 41 different wave components of different directions. Among them,  $0, \eta_{:x}, 1_{:y}, \tau_{:x}$  and  $\tau_{:y}$  represent no VZFO case, and fundamental frequency of each direction of the two grids, respectively. Others components are the newly induced periods resulted from the overlapping. Among these components,  $\eta^2 - 2\eta\tau\cos\gamma + \tau^2|_{x'}$  has the smallest value of all for small  $\gamma$  angle range. This component is for x direction only and for the two-line pattern case. It fits the best to explain the moirés which are resulted from the beat phenomenon. The maximum moiré fringe period is given as  $P_y/(\eta^2 - 2\eta\tau\cos\gamma + \tau^2)$ . When  $\gamma = 0$ , it is reduced as  $\sqrt{f_n(\tau, \gamma)} = \eta - \tau$ . Hence the moiré fringe period is given as  $P_y/(\eta - \tau)$  in x direction. This is the conventional formula of calculating the moiré fringe period. Hence the periods of moiré fringes in different directions specified in Eq. (3-5) works only for the static moirés from two-line pattern films with no gap material between them. It is actually not much related to the color moirés in the contact-type 3-D imaging but it can only help to explain that the color moirés in the contact-type 3-D imaging are formed by moirés with many different periods when the VZFO line pattern is rotated, Eq. (3-5) cannot explain the color and dynamic behaviors of the moirés in the contact-type 3-D displays. To explain these behaviors, another method should be devised.

### 3.3 Color moirés in contact-type 3-D imaging

For the case of the static moirés, the lines in the two-line patterns are either overlapped fully or partly, or filled the spaces between lines of the patterns. These overlapping and filling create periodical sparse and dense looking areas. These are the moirés. In contrast to these overlapping and filling, the pixel pattern is simply blocked by the VZFO line pattern because the pixel pattern is almost continuous with only small gaps between pixels and sub-pixels. Due to the blocking, some sub-pixels and/ part of a sub-pixel become dark, i.e., invisible or lose its brightness. So, the color balance of the panel becomes broken by these blockings. Figure 3-2 shows the color moirés appearing at a 24-inch contact-type 3-D imaging with lenticular as the VZFO.

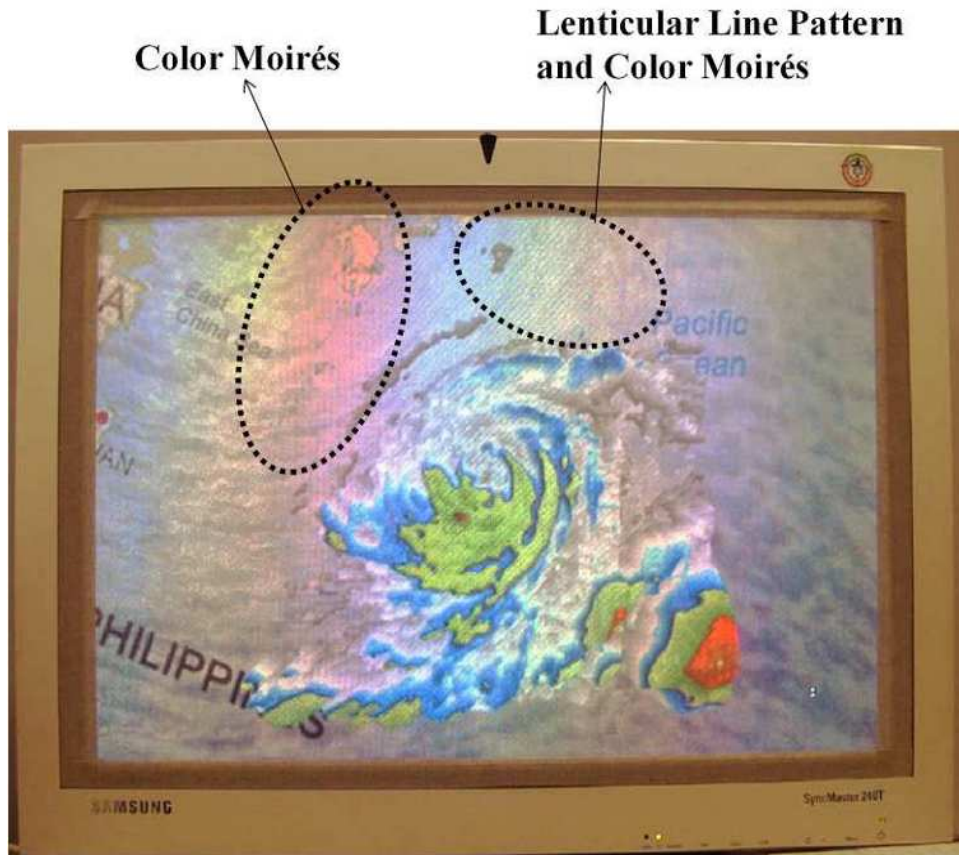


Fig. 3-2. Color moirés on a 24-inch multiview display with a lenticular VZFO.

The display has a full HD resolution. The image is covered almost with color moirés but only that in the upper left and the mid-top area reveal distinguishable color moirés. It is also shown that dark lines representing the lenticular pattern at the mid-top area. Figure 3-3 shows the color balance changes due to the blockings when the VZFO including the panel's cover glass is assumed as a film. When no blocking is done for RGB sub-pixels, the pixel reveals white color, but each sub-pixel is blocked the same amount, the pixel reveals a silver to various gray colors. When a part of R, G or B is blocked, the pixel reveals celeste, lavender and conditioner, respectively. When two of R, G and B are completely and remain is partly blocked, the pixel reveals the partly blocked sub-pixel color but it becomes darker. So, this color balance changes are the main reason of the moirés. When VZFO is a film like a parallax barrier and it is overlapped with an air gap with the pixel pattern, the resulted moirés are not different from that from the two films, except the pattern period changes. By the covering of the pixel pattern with the barrier lines, the pixel colors are projected differently to a visual device as shown in Fig. 3.

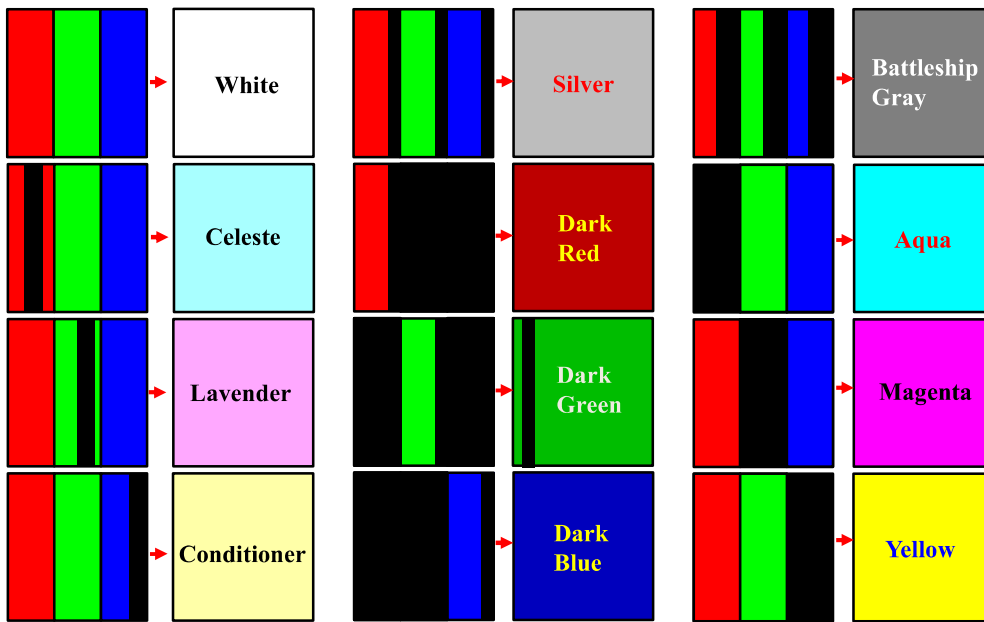


Fig. 3-3. Color balance changes due to blockings of sub-pixels or a part of sub-pixel.

This is shown in Fig. 3-4. Figure 3-4 depicts the gap effect. When the gap is  $g_{ap}$ , the viewing distance is  $Z_V$  and the focal length of a viewer's eye is  $f_{eye}$ , then the periods of VZFO line and pixel patterns are changed by the factors  $f_{eye}/Z_V$  and  $f_{eye}/(Z_V + t)$  [3-17], respectively. When the VZFO has a thickness with a refractive index, the pixel pattern is refracted first to go through the VZFO to be viewed by the viewers.

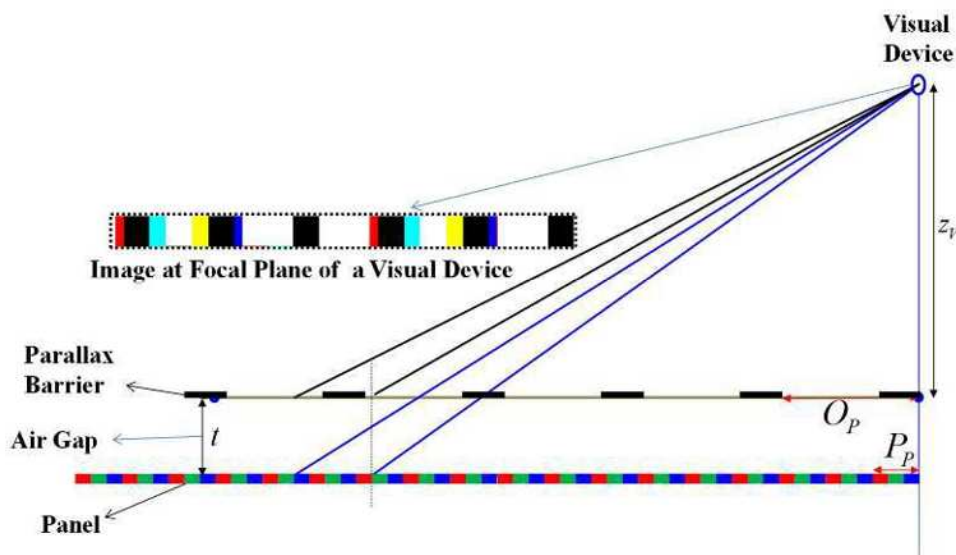
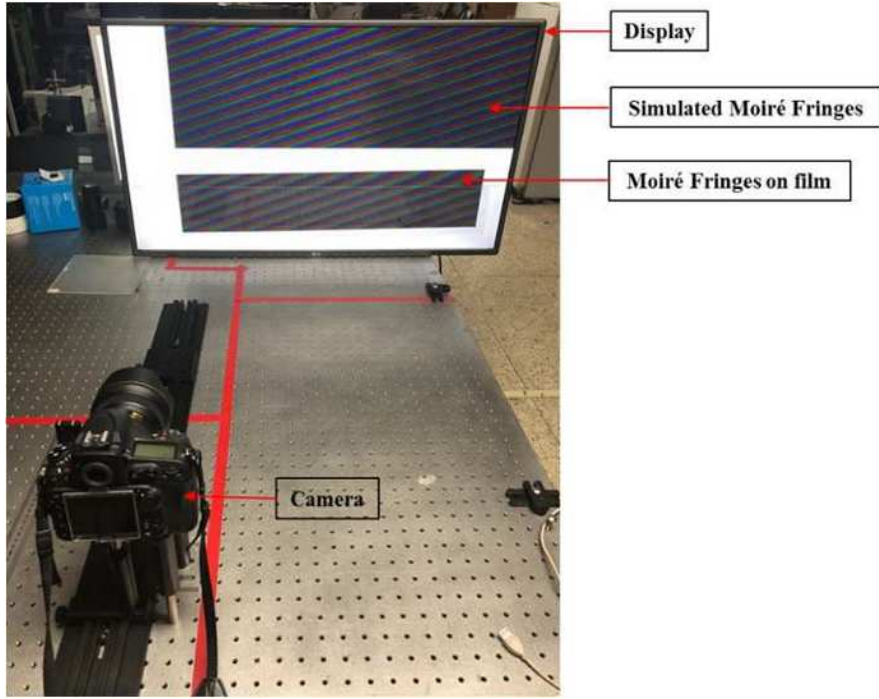


Fig. 3-4. Optical geometry of depicting Gap-effect.





(b)

Fig. 3-5. Optical geometry of viewing the pixel pattern through the VZFO and calculating the chirped pixel pattern(a), The experimental set-up(b).

In Fig. 3-5, when a viewer at the viewing distance  $Z_V$  along the normal line of the panel aligns his/her eye to the center of the panel, C, the  $n^{th}$  pixel from C, which is specified by BB' will be translated to AA' at the pattern plane of the VZFO due to the refraction. AA' becomes slightly shorter than BB'. Hence the panel's pixel pattern is chirped as shown in the bottom side of Fig. 3-5. Let the period of VZFO line pattern and pixel period are  $O_p$  and  $P_p$ , respectively, the length of AA' as  $P_p(n)$ ,  $\theta(n)(\theta_r(n))$  and  $\theta(n-1)(\theta_r(n-1))$  as the viewing angle (refraction angle) of seeing  $n^{th}$  and  $(n-1)^{th}$  pixels, respectively and  $t$  the VZFO thickness including the glass,  $P_p(n)$ , is given as [3-4]

$$P_p(n) = P_p - t(\tan \theta_r(n) - \tan \theta_r(n-1))$$

$$\theta_r(n) = \sin^{-1}\left(\frac{1}{m} \sin \theta(n)\right)$$

$$\theta_r(n-1) = \sin^{-1}\left(\frac{1}{m} \sin \theta(n-1)\right), \quad (3-6)$$

where  $m$  is the refractive index of the VZFO material calculated as mentioned above. Eq. (3-6) informs that since

the pixel size is very small compared with the distance  $Z_V$ , as the viewing angle  $\theta(n)$  increases, the difference between  $\theta(n)$  and  $\theta(n - 1)$  becomes smaller,  $P_p(n)$  closes to  $P_p$ . Hence the chirping is more for smaller viewing angles but less as the viewing angle increases. The virtual decrease in the panel's pixel pattern is just given as  $t \tan \theta_r(n)$ , i.e.,  $t \tan\{\sin^{-1}((1/m) \sin \theta(n))\}$ . So, the chirping amount depends on the VZFO thickness and the viewing angle. Since  $t$  can be several millimeters for large size 3-D TV and each pixel is much smaller than  $t$ , but the chirping amount is still too small for the panel size. Hence it is difficult to view the chirping effect with a small size panel. The chirping effect is more visible as the viewing angle and the moiré fringe period increase. This is shown in Fig. 3-6. Fig. 3-6 is obtained by moiré simulation. The chirping effect is more visible as the viewing angle increases, i.e., the viewing distance decreases and/or the fringe period increases.

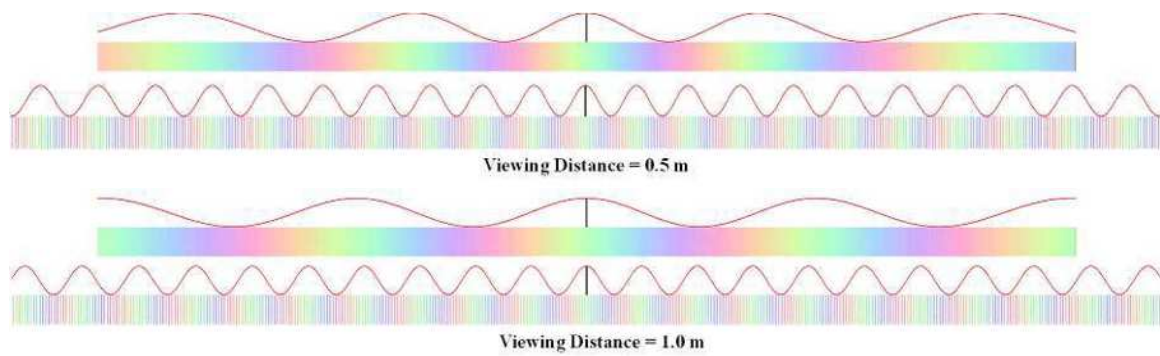


Fig. 3-6. Examples of chirped moirés.

To show the chirping effect more clearly, the moiré fringe periods are specified by the waves on the top of each moiré. The chirping effect is very visible when  $O_p$  and  $P_p$  are the same. This is shown in Fig. 3-7. Figure 3-7 is color strips of a simulated color moirés when both  $O_p$  and  $P_p$  are 0.4833 mm,  $t = 0.68$  mm and  $m = 1.5412$  for the three  $Z_V$  values of 500 mm, 1 m and 2 m. The accuracy of this simulation is demonstrated by experiments [3-17]. The color patterns in the central areas of the color strips in Fig. 3-7 for the three viewing distances are the same. Since the viewing angle becomes bigger as the distance decreases, the area of the color pattern becomes wider as the distance increases. As the panel size increases, i.e., the viewing angle increases, the color changing rate of the moirés will be very low because of very small variations in  $P_p(n)$  values. There will be almost no difference between  $P_p(n)$  and  $P_p$ . In this situation, the chirping effect will be diminished as shown in Fig. 3-7.

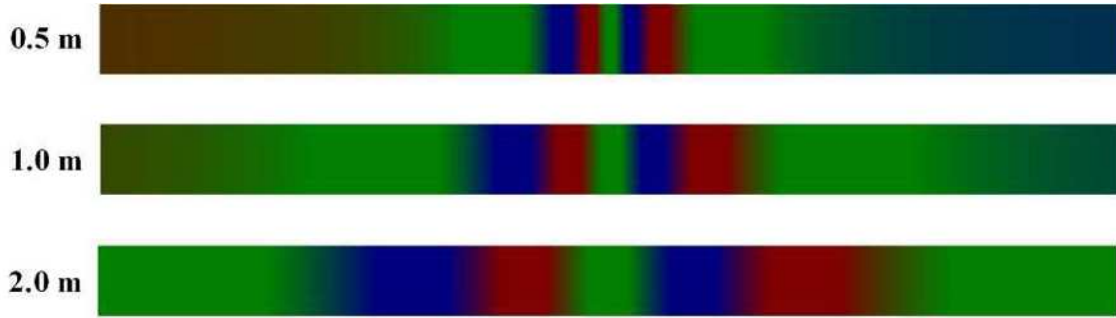


Fig. 3-7. Chirped moirés when the periods of pixel and VZFO line patterns are the same.

### 3.4 A formula for the moiré fringe periods

As mentioned before, the moiré fringe period  $P_m(x)$  is expressed as [3-12]

$$P_m(x) = [\cos\{\pi(\frac{P_{px}(x)}{P_p} - \frac{Ax}{3O_p})\}]^2, \quad (3-7)$$

Where  $P_{px}(x)$  is the fitting function of  $P_p(n)$ ,  $x$  is the distance from C in Fig. 3-3 and  $A$  is given as

$$\begin{aligned} A &= k \text{ when } 0 \leq R \leq S_p/2 \\ A &= k + 1 \text{ when } S_p/2 \leq R < S_p \\ k &= [O_p/S_p] \text{ and } O_p = kS_p + R \quad (0 \leq R < S_p), \end{aligned} \quad (3-8)$$

In Eq. (3-8),  $k$  is the integer value from  $O_p/S_p$ , where  $S_p$  is the sub-pixel period and  $R$  is the remains from  $O_p/S_p$ . Eq. (3-8) is the factor which make difference between the conventional  $(\eta - \tau)P_p$  and the color moirés formulas for the moiré fringe period. With the Eq. (3-8), Eq. (3-7) becomes the same as Eq. (1) for  $\gamma = 0$  case. With use of Eqs. (3-7) and (3-8), the  $P_m(n)$  for the case of a parallax barrier with  $O_p = 1.4509$  mm and barrier width of 0.2415 mm is shown in Fig. 8 for two viewing distances of 500 mm and 1 m. Simulation and film mean that the moirés are simulated and experimentally obtained with the parallax barrier film, respectively. The color patterns of both simulated and experimentally obtained moirés match very well to each other.

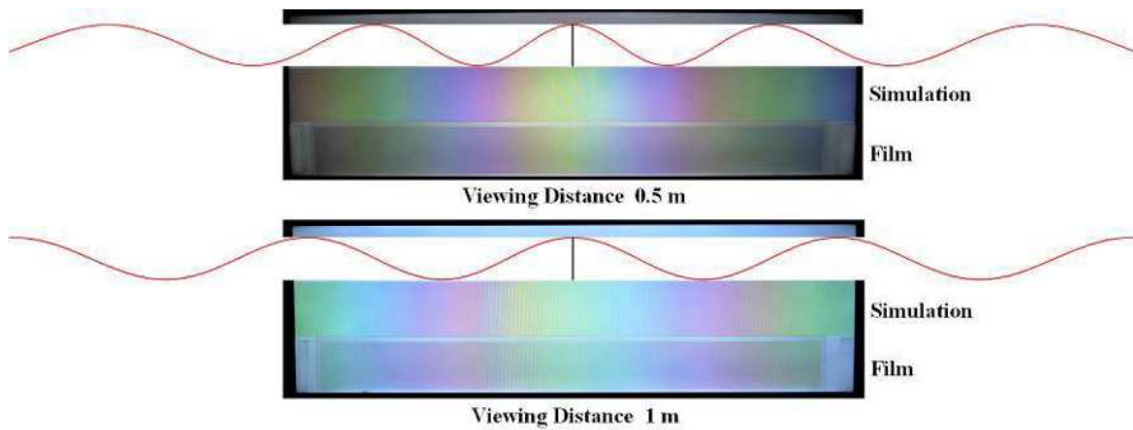


Fig. 3-8. Moirés fringe periods: Film and simulated moirés have the same fringe periods.

The moiré fringe periods are given as the waves in Fig. 3-8. For the case of Fig. 3-7, i.e.,  $O_p = P_p$  case, the fringe period can also be calculated with Eq. (3-7). This is shown in Fig. 3-9 for only near the central part of the moirés at the 0.5 m and 1 m viewing distances in Fig. 3-7.

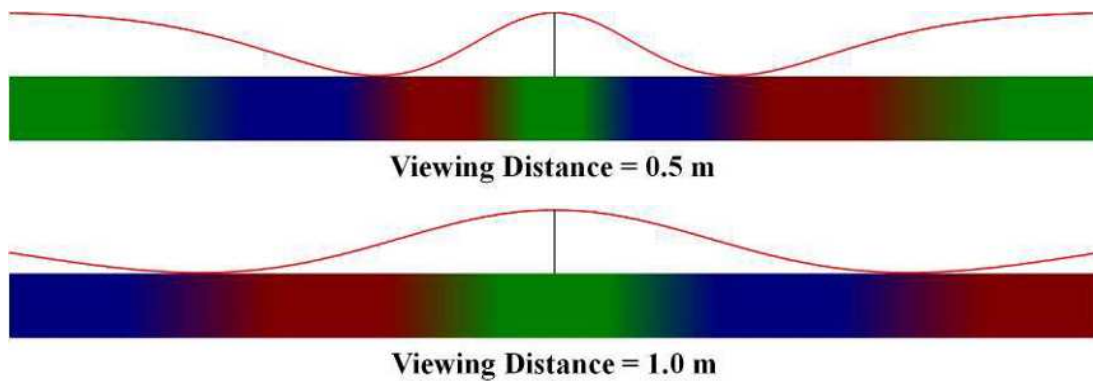


Fig. 3-9. Fringe periods of the chirped moirés in Fig. 3-7

### 3.5 Moiré characteristic for different VZFO

The color moirés in the contact type 3-D imaging has somewhat different characteristics for different VZFOs. As mentioned in section 3, the color moirés are the results of the pixel pattern blocking by the VZFO line pattern. The blocking will be more as the line thickness increases. In the lenticular, the line pattern is formed by the boundary lines between lenslets. The thicknesses of these boundary lines are not known but it is assumed that it will be very small and the lenslets are transparent. The microlens array is the same as the lenticular, except it is

two-dimensional [3-19]. For the case of parallax barriers, it forms a grating pattern but the thickness of barrier lines is more than the grating lines. In the parallax barrier, the image will be sharper as the slit width decreases but in practice, the barrier thickness is around  $2/3$  to  $3/4$  of the line period to keep the image brightness to a certain level. Fig. 3-10 shows the comparison between the equivalent geometrical patterns of lenticular and parallax barrier. The geometrical patterns are conjugate to each other. By these reasons, it can be said that the color moirés in lenticular is caused by the boundary lines but for the parallax barrier by the open slits, i.e., the gap between two barrier lines. Hence the equivalent line patterns of the lenticular and the parallax barrier are complementary to each other.

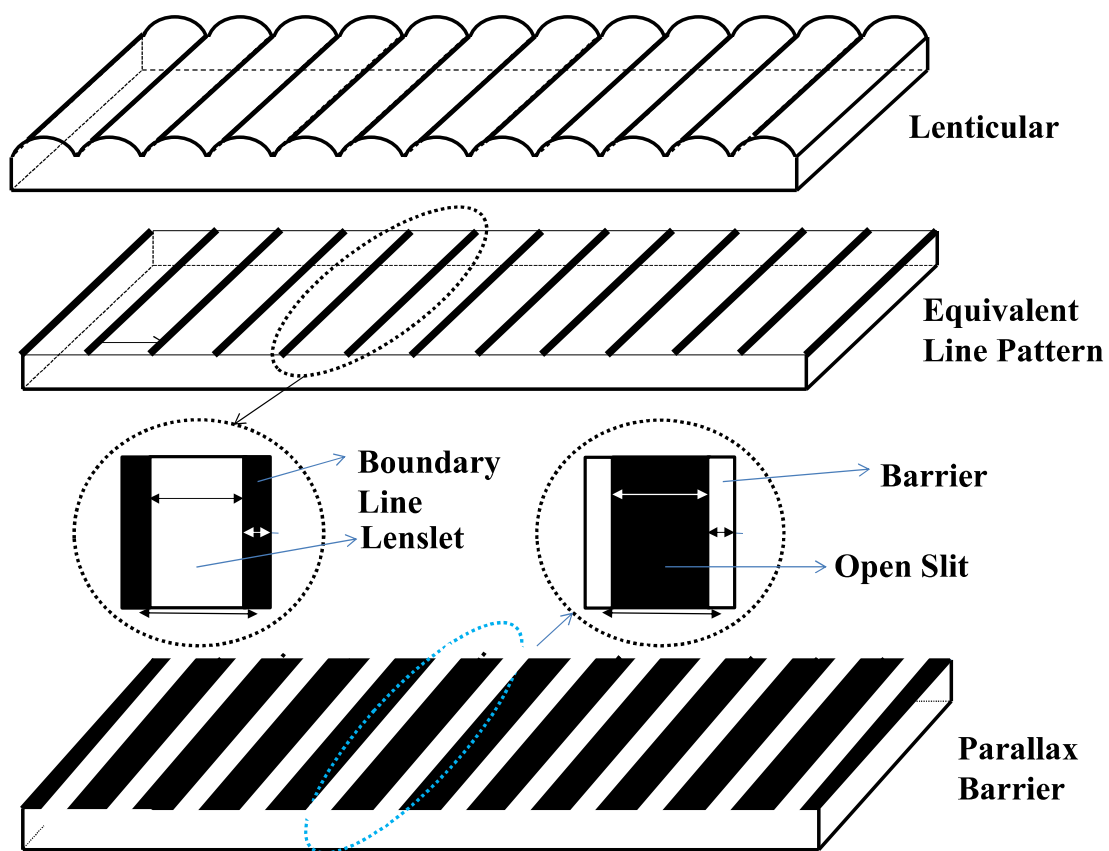


Fig. 3-10. Comparison between equivalent geometrical patterns of lenticular and parallax barrier.

Since the boundary line thickness in the lenticular can be less than 0.1 of the line period, the blockings by the lines do not cause too much color changes. As the result, the moiré contrast becomes very small compared with the displayed image. Hence the presence of the color moirés can be hardly identified. For the case of the parallax

barrier, since the displayed image is mostly covered by the barrier lines and the image is seen through the open slits, the moiré is very visible. This is shown in Fig. 3-10. Figure 3-10 compares the line thickness effect on the moiré contrasts for the case of  $O_p = 3.4$  mm. For this comparison, six-line thicknesses of 0.0805 mm, 0.1611 mm, 0.3222 mm, 3.3195 mm, 3.2389 mm and 3.0778 mm are used, and both simulated and experimentally obtained moirés with the film are also given. There are no differences between the simulation and the experiment. The first three-line thicknesses are complementary to the last three in their currently order because the sum of each complementary thickness corresponds to 3.4 mm. So, the first three thicknesses are for the lenticular and the last three for the parallax barrier. The image is displayed at 42-inch LCD monitor having full HD pixel resolution, i.e.,  $1920 \times 1080$  and pixel size of 0.4833 mm. For the first three-line thicknesses, the image does not look affected by the moirés, except the line pattern for 0.3222  $\mu\text{m}$  case. This is obvious because the line thickness is smaller than a pixel pitch. Most of the image is viewed with no color change through the open slits. However, for the last three, the moirés are more visible than the image. The image brightness is reduced further as the lint thickness increases and it looks that the moirés are modulated by the image due to very small open slit sizes which are smaller than a pixel pitch. When the open slit size is bigger than a pixel, a part of the image will be viewed without any color change through each open slit.

### **3.6 Moiré reductions methods**

As mentioned in introduction, there are two known methods of reducing moirés in the contact-type 3-D imaging: One is aligning the line direction of VZFO's line pattern to have a certain angle with the vertical or horizontal) pixel lines and the other inserting a diffuser between VZFO and the cover glass of the pixel. The former method is effective in reducing visibly the moirés but it will reduce the active pixels along the slanted VZFO line pattern and increase crosstalk [3-18]. The color moirés seen at 0.5 m from the panel at the aligning angle range of  $0^\circ$  to  $19^\circ$  in  $3^\circ$  interval for both lenticular and parallax barrier are shown in Fig. 3-11. Figure 3-11 is obtained experimentally. It clearly shows that the color moirés look disappearing as the angle increases, this is true because the repeating rate of the three primary colors is increasing as the angle increases.

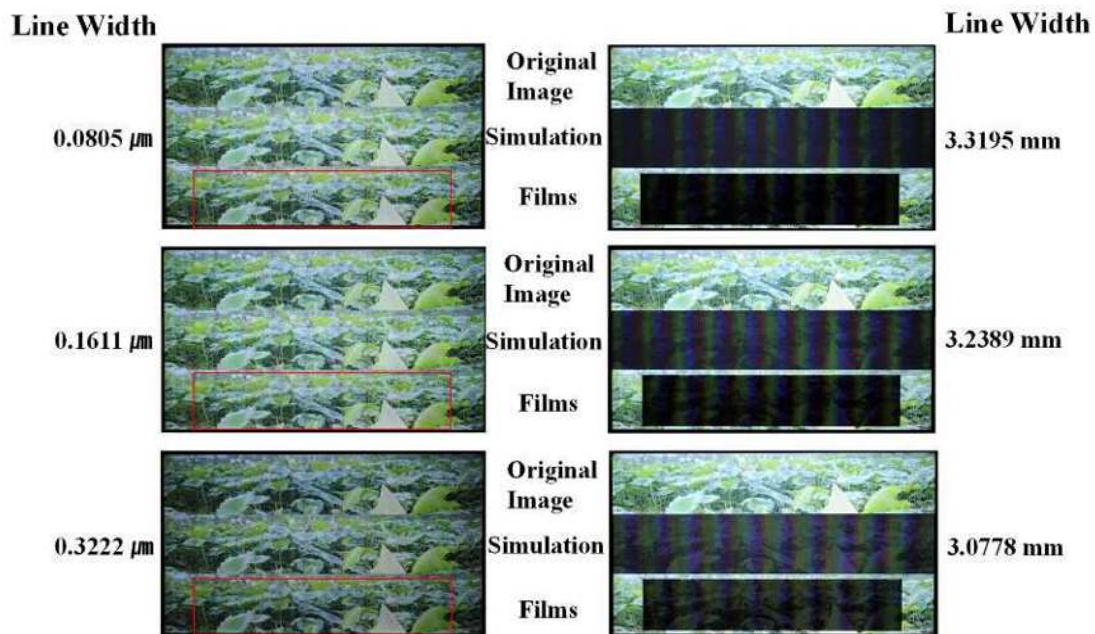


Fig. 3-11. Comparisons of moirés for different line thickness.

For the  $0^\circ$  case, each open slit (boundary line) opens(blocks) only the same column pixels or sub-pixels because the typical LCD panel consists of a repeated array of RGB sub-pixel columns. Hence as the angle increases, they open(blocks) more neighboring columns. As the consequence, the same color length is reduced to smaller than a pixel height, i.e., when a boundary or barrier line passes a sub-pixel pitch within a pixel height. This can happen when the angle is greater than  $18.44^\circ$  ( $\tan^{-1}(1/3)$ ). The RGB colors become closer as the angle increases and they can be easily combined as a white or a gray. This is why the color between barrier lines and along the boundary lines looks gray in the parallax barrier and almost invisible in the lenticular. For the case of the lenticular, the width of an elemental lens is much wider than a boundary line thickness, the gray pixels along the boundary lines are hardly identifiable. The moiré contrast is very low compared with the background. Hence the image looks having the same color as shown in Fig. 3-12. This is why it is difficult to trace color moiré components in the images in the left side of Fig. 3-11. Fig. 3-12 informs that if the boundary line thickness can be made very small or eliminated in the lenticular and microlens array, the moirés can be made almost invisible or eliminated. But it is hard to minimize the moirés in parallax barrier.

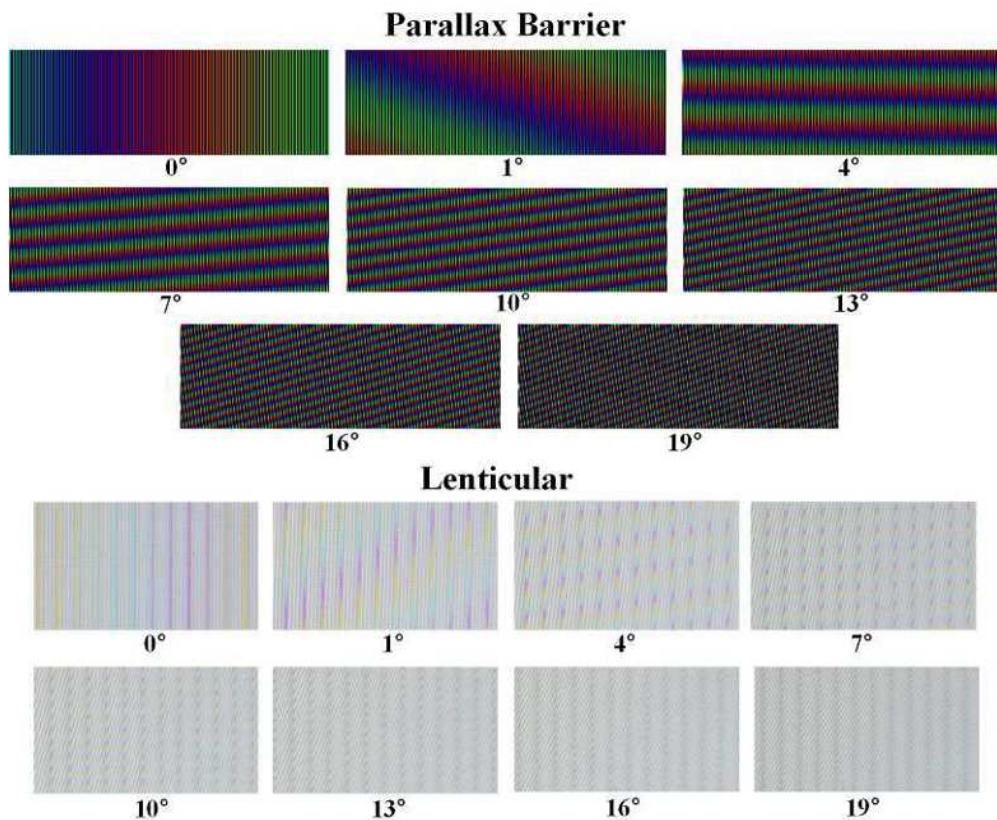


Fig. 3-12. Moirés reduction with increasing aligning angle between pixel and VZFO line patterns.

A diffuser between the panel and the VZFO is a very effective in reducing the color moirés. The diffuser is actually breaking the regularity of the pixel pattern by diffusing the boundaries between pixels/sub-pixels. The problem is the diminishing in the pixel boundary. If the pixel boundary is diminished, the viewing region for each view image will not be clearly defined as the consequence, the crosstalk between neighboring images can be increased. Furthermore, the image sharpness can be lost. The effect of diffusers on the color moirés is shown in Fig. 3-13 for four different diffusers of different characteristics as specified by the number 1 to 4 for the lenticular case. It looks that the moiré reduction has been done equally without regarding the diffuser characteristics, the color moirés are almost disappeared.

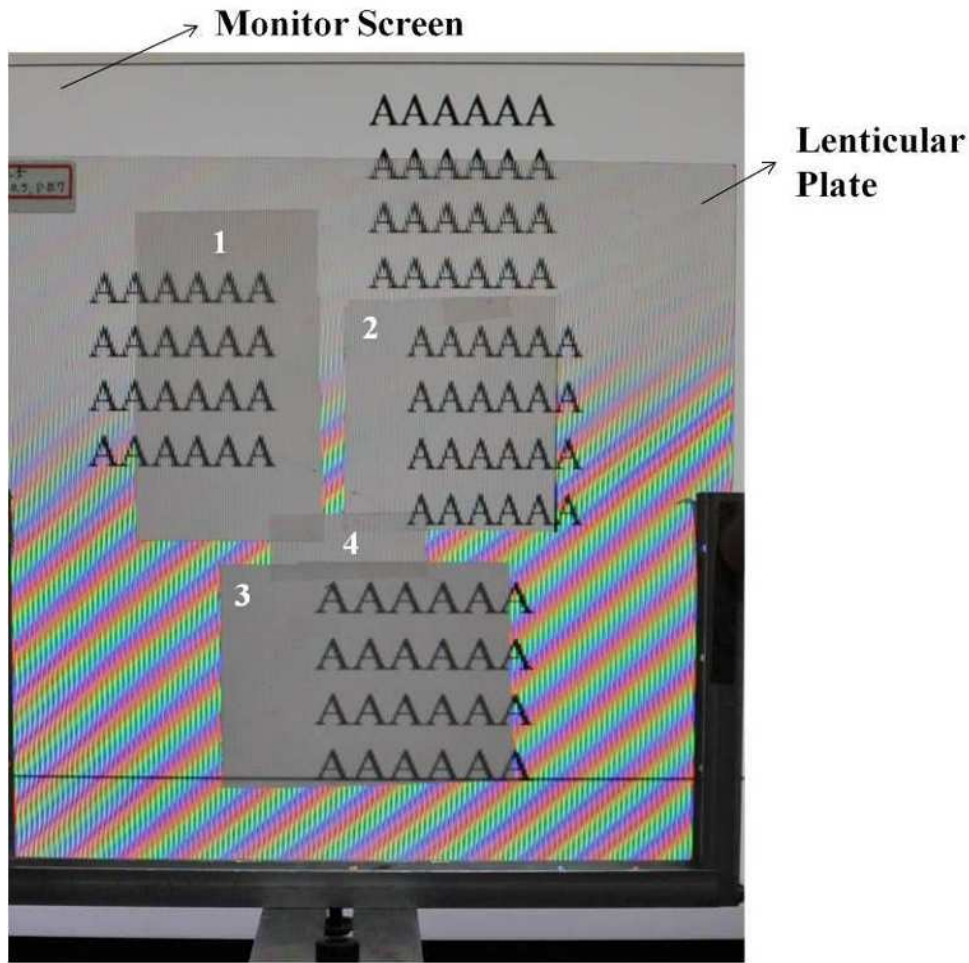


Fig. 3-13. Moirés reductions with diffuser of different characteristics.

### 3.7 Conclusions

The color moirés in contact-type 3-D imaging behave differently from the conventional moirés based on the beat phenomenon. The presence of VZFO material thickness, a large period difference between the pixel and VZFO's equivalent line patterns and blocked pixel pattern by the VZFO line pattern. This color moirés cannot be eliminated because of basic structure of the imaging but can be minimized with two known methods of 1) aligning the VZFO line pattern to have a certain angle with the pixel patter and 2) inserting a diffuser between VZFO and the panel though they can bring the problem of increasing the crosstalk between neighboring images, and decreasing active pixel numbers and image sharpness. So, it is necessary to develop a quantifying method of moirés and to set the allowable amount moirés for the given 3-D displays in future.

## 4 Fringe periods of color moirés in contact-type 3-D displays

### 4.1 Introduction

The thickness, i.e., widths of the lines forming the line pattern and plate thickness of viewing zone forming optics (VZFO) in the contact-type 3-D displays [4-1], are the main sources of causing moirés in them [4-2], [4-3]. In the 3-D displays, when a VZFO is superposed on the top of a flat display panel, two inseparable physical interactions appear between the pixel pattern in the panel and VZFO's line pattern formed by elemental lenses or line slits: The first interaction is that a part of the light coming from pixels is blocked by the boundary lines between adjacent elemental lenses or the gaps between the slits. Due to this blocking, the colors appearing through the VZFO becomes different from those on the display panel and the brightness of the image through the VZFO becomes reduced in proportional to the blocking amount, in compared with that on the panel. The second interaction is the mixing between the VZFO's line pattern and the pixel pattern. This mixing induces moirés. Since the two patterns are having different periods, the VZFO's line pattern will either overlap or align side by side to the pixel pattern. This overlapping will make parts of the pixel pattern invisible. Hence as the width of the dark lines forming the VZFO's line pattern increases, the invisible parts will also be widened and the gaps between the aligned lines will be reduced. These overlapping and aligning create sparse and dense regions, i.e., bright and dark regions. If the VZFO and pixel patterns are periodically drawn as line grating patterns, these densely and sparsely mixed regions appear periodically. This periodical appearance of dense and sparse regions is named as moirés. So, for the creation of moirés, it is necessary to make the two patterns to be mixed together and to appear at a plane. This is why the moirés induced by the gap effect are interpreted within the image planes of visual devices [4-4]. In the 3-D displays, the moirés are colored and their fringes are chirped because the VZFO has a finite thickness with a certain refractive index and the lines in its pattern have a width. These make the mixing to appear differently from the gap effect. The VZFO thickness makes the panel pattern to refract toward viewer's eyes when a viewer watches the panel [4-3]. Hence the panel's pixel pattern virtually appears at the pattern plane of the VZFO and is mixed with the VZFO pattern to form the moirés. This also explains why the moiré fringes look floating above the image on the panel. The refraction also causes the panel pattern at the VZFO's pattern plane to have a different form from its pattern at the panel plane. The pattern is virtually contracted by the refraction process when it passes

through the VZFO. The contraction will be more as the viewing angle of the pattern increases. Hence the contracted pattern has the form of a chirp signal. The chirping starts from the normal direction of viewing the panel and the viewing angle changes with the viewing distance. By this reason, the moiré fringes are also shifting as a viewer changes his/her viewing position and the fringe periods change as the viewing distance changes. The amount of contraction is functions of viewer's viewing angle, thickness and refractive index of VZFO. Due to this chirping, the moiré fringes are also chirped and they appear even when the periods of two patterns are the same. The colors in the moiré fringes are mainly caused by the line width because the sub-pixel colors are differently blocked by the width [4-2]. Hence the thickness of the VZFO and the line width of VZFO's line pattern are the main source of viewing position dependent color moiré fringes. The problem with these color moiré fringes is that they are harmful to the 3-D displays [4-5]-[4-8] because of their hostile behaviors of deteriorating the 3-D image quality. However, there is not a proper way of characterizing the moiré fringes. The fringe period is the first parameter used to characterize moirés appearing when two regular line patterns are overlapped together. However, the conventional beat frequency formula cannot describe the fringe period of the color moirés appearing at the contact-type 3-D displays. This is because the moirés are chirped and the period of VZFO line pattern is usually more than two times of that of the pixel pattern in the display panel for the multiview images. The formula can work only when the periods of the two-line patterns have a small difference to initiate a beat frequency. This is only formula known so far but when the periods of the two-line patterns have a large difference as the contact-type 3-D displays, it does not work. A new formula is needed to describe the 3-D displays case.

In this paper, a new mathematical formula to calculate the fringe periods of the color moirés appearing at the contact-type 3-D displays is derived. And the accuracy of the formula is shown with several VZFO line patterns having different line periods for given display panels.

## **4.2 Derivation of moiré fringe periods in the contact-type 3-D displays**

The main source of causing color moirés in contact-type 3-D displays has already been mentioned in the introduction but they work differently for different types of VZFO, such as lenticular and parallax barrier. In the lenticular and parallax barrier, the line patterns are formed by the boundary lines between elemental lenses and line slits, respectively. The width and the transparency of the boundary lines are not known but it is considered as very thin compared with the pitch of the elemental lenses. However, the slit width is typically in the range of one

third to one quarter of the distance between slits to maximize the image brightness in the parallax barrier. This makes the dark line width of the parallax barrier be in the range of two thirds to three quarters of the distance. The moirés are induced by the boundary lines between elemental lenses for the lenticular, but by line slits for the parallax barrier. Since the boundary lines are dark and the slit lines are bright, the moiré fringes have higher brightness for parallax barrier than for the lenticular. This means that moiré fringes in the parallax barrier can be brighter than the image on the display panel but darker in the lenticular. However, the relative brightness of the moiré fringes in the lenticular and parallax barrier depends mainly on the pitch sizes of the barriers and elemental lenses relative to the pixel pitch. Hence the effect of moirés on the quality of images in the contact-type displays having the lenticular as their VZFO will be smaller than those having parallax barrier as their VZFO. Since moirés are having periodic fringe patterns, their periods are deeply involved in determining their contrasts and visibility. As the periods become smaller, they become more visible because the intensity and color variations in moiré laden images will appear more frequently. When the pitch of a sub-pixel and the period of elemental optics in VZFO are specified as  $S_p$  and  $O_p$ , respectively, the conventional beat frequency formula [4-9], [4-10] describes the fringe period as,  $|1/3S_p - 1/O_p|$ . But this formula does not work for predicting the periods of the moirés appearing at the contact-type 3-D displays because the period of elemental optics in the VZFO is much larger than that of the pixels in the panel. This is obvious because the moirés are formed only by the boundary lines of the elemental optics. So, the new formula should offset the large period difference between the VZFO line pattern and the pixel pattern. The period difference can be offset by the following way:  $O_p = [O_p/S_p]S_p + R$  ( $0 \leq R < S_p$ ), where  $R$  is remainder and  $k = [O_p/S_p]$  represents the integer value produced by dividing  $S_p$  into  $O_p$ . Then the moiré fringe period  $P_M$  when the VZFO has no thickness, is expressed as,

$$P_M = 3 \left| \frac{O_p S_p}{O_p - A S_p} \right| = 3 \left| \frac{1}{3S_p} - \frac{1}{3O_p/A} \right| = \left| \frac{1}{P_p} - \frac{A}{3O_p} \right| \quad (4-1)$$

where factor 3 counts for RGB sub-pixels, and the pixel size  $P_p$  is  $3S_p$  and  $A$  is given as,

$$\begin{aligned} A &= k \text{ when } 0 \leq R \leq S_p/2 \\ A &= k + 1 \text{ when } S_p/2 \leq R < S_p \end{aligned} \quad (4-2)$$

Equation (4-1) is different from conventional beat frequency approach of calculating moiré fringe period by the factor  $A/3$ . Without this factor, moiré fringe period can be smaller than  $O_p$  when  $O_p > 2S_p$ . This is contradicting to the beat frequency concept. Equation (4-1) can be derived by the following way too: Since  $R$  is the remainder,  $S_p/R$  elemental optics are needed to sweep a sub-pixel width for the case when  $0 \leq R \leq S_p/2$ . This represents

the case when the period of the bottom pattern is smaller than that of the top pattern. However, when  $S_p/2 \leq R < S_p$ , the number of elemental optics required to sweep out  $S_p$  is not  $S_p/R$  but  $S_p/(S_p - R)$ . For this reason, the 2nd relationship in Eq. (4-2) should be used, though it forces the denominator  $O_p - AS_p$  in Eq. (4-1) to have a negative value. Hence this represents the case when the period of the bottom pattern is bigger than that of the top pattern. Equation (4-1) is obtained by substituting either  $(S_p/R)O_p$  or  $\{S_p/(S_p - R)\}O_p$  for  $R$  based on the criterion specified in Eq. (4-2). With Eq. (4-2), the waveform of the moiré fringe in the conventional formula  $\cos^2\{\pi(1/P_p - 1/O_p)x\}$  [4-3] should be replaced by  $\cos^2\{\pi(1/P_p - A/3O_p)x\}$ , where  $x$  is the distance along the horizontal direction of the display panel, from the point which corresponds to the normal position of viewer's an eye on the panel. When VZFO thickness is considered, the pixel pitch  $P_p$  will be no longer constant but it will virtually vary along the horizontal direction due to the refraction phenomenon. The graphical illustration of the pixel pitch variation is shown in Fig. 4-1. The physical structure of the contact-type 3-D displays consists of a display panel and a VZFO which is superposed on the panel. In this structure, the panel's pixel array looks appearing at the VZFO's line pattern plane due to the refraction effect and it is blocked by the line pattern to form a color moiré as explained in previous section. The refraction effect forces the pixel pitch to be contracted slightly.

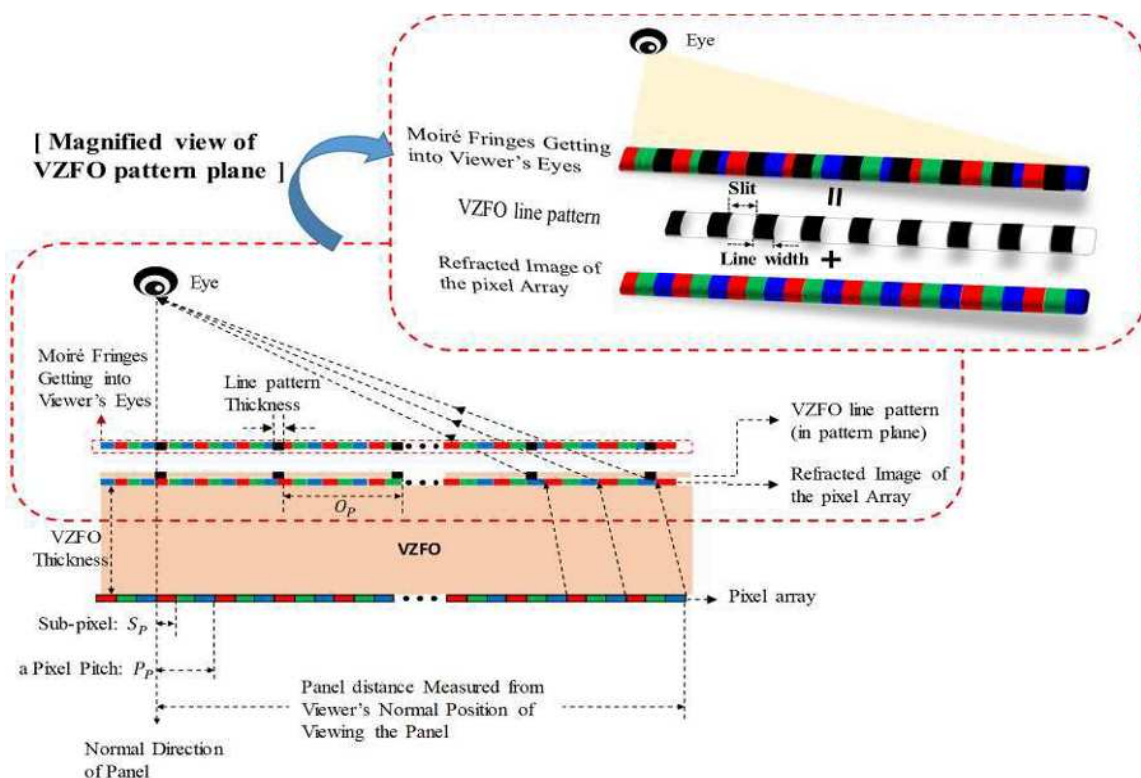


Fig. 4-1. A geometry of forming moiré fringes

The amount of the contraction depends on the thickness and the refractive index of the VZFO's medium, and the panel distance from the viewer's normal position of viewing the panel. As a result, the pixel pitch on the pattern plane shrinks more in the close distances from the viewing position but less in the farther distances. This means that the pixel pitch is virtually chirped. The color moiré fringes are created by the superposition of the virtually chirped pixel pattern and the VZFO's line pattern. They are nothing but the virtually chirped pixel pattern blocked by the barriers, i.e., lines on the VZFO's line pattern. In the gap between neighboring barrier lines, the moiré fringes represent the virtually chirped pixel pattern. Hence if the gap width is more than two times of the pixel pitch, at least a pixel will be untouched. This is the reason why the current beat frequency formula fails to calculate the periods of the moiré fringes. If the virtually varying pixel pitch is represented as  $P(x)$ , it can turn to a continuous function by an interpolation and have a chirped signal form. If  $P(x)$  is normalized as  $P_p/P(x)$ , its chirped signal phase is expressed as  $P_{Px}(x) = \int \{P_p/P(x)\} dx$  [4-11]. In this case, the moiré fringe  $P_M(x)$  in a continuous waveform will be written as,

$$P_M(x) = [\cos\{\pi(\frac{P_{Px}(x)}{P_p} - \frac{Ax}{3O_p})\}]^2 \quad (4-3)$$

In Eq. (4-3), since  $P_{Px}(x)/P_p$  is the function of  $P(x)$  and  $A/3O_p$  is  $1/P_p$  when  $O_p$  is an integer multiple of  $S_p$ ,  $P_M(x)$  is only determined by  $P(x)$ . This means that  $P_M(x)$  will have the same value when  $O_p$  is any integer multiple of  $S_p$ . The VZFO thickness turns visually the uniform pixel pattern into a chirped pixel pattern as  $x$  increases, as explained in the previous section. In Eq. (4-3),  $P_M(x)$  will be zero when  $P_{Px}(x)/P_p - (A/3O_p)x$  equals either  $2l + 0.5$  or  $2l + 1.5$ , where  $l = 0, 1, 2, 3, \dots$ . Since the periods of  $P_M(x)$ ,  $P_M(k)$  is defined as the distance between  $x$  values corresponding to the two-phase values, they are calculated as,

$$P_M(l) = \frac{3O_p}{AP_p} \{P_{Px}(x_{2l+1.5}) - P_{Px}(x_{2l+0.5})\} - \frac{3O_p}{A}, \quad (4-4)$$

In the contact-type multiview 3-D displays, the relationship between periods of pixel cell/elemental image and the elemental optic in VZFO is given as [12],

$$\frac{d}{d+f} = \frac{O_p}{nS_p} = \frac{[O_p/S_p]S_p + R}{nS_p} \quad (4-5)$$

where  $d$ ,  $f$  and  $n$  are the designed viewing distance and focal length of VZFO and the number of multiview images loaded on the panel, respectively, when the images are loaded by sub-pixel base. From Eq. (4-5),  $f/d = 1 - O_p/nS_p$ . Equation (4-5) can be rewritten as,

$$\frac{d}{d+f} = \frac{kS_p+R}{nS_p} \cong 1 - \frac{f}{d} \quad (4-6)$$

Eq. (4-6) is derived by assuming that  $d \gg f$ . In Eq. 6, since  $R < S_p$  and  $k$  cannot be larger than  $n$  [12], if  $k = n - j$ , where  $j$  is an integer, Equation 6 can be rewritten as,

$$\frac{(n-j)S_p+R}{nS_p} = 1 - \frac{jS_p-R}{nS_p} \cong 1 - \frac{f}{d} \quad (4-7)$$

The 2nd and 3rd terms in Eq. (4-7) indicate that  $(jS_p - R)/nS_p \cong f/d$ . This relationship is solved for  $R = jS_p - nS_p(f/d) = S_p(j - nf/d)$ . From this relationship, Eq. (4-4) will be rewritten as,

$$P_M(l) = \frac{n(1-f/d)}{A} \{P_{Px}(x_{2l+1.5}) - P_{Px}(x_{2l+0.5}) - P_P\} \quad (4-8)$$

The contact-type multiview 3-D displays are classified into two groups by their optical configurations such as parallel and radial: The parallel group satisfies the relationship  $O_p = nS_p$  and the radial group  $O_p < nS_p$ . The parallel group includes those displays having an elemental image as their basic image unit and the radial those having a pixel cell [4-13]. For the case of  $O_p = nS_p$ ,  $k = n$ , i.e.,  $A = n$ . Hence Eq. (4-8) can be rewritten as,

$$P_M(l) = (1 - f/d) \{P_{Px}(x_{2l+1.5}) - P_{Px}(x_{2l+0.5}) - P_P\} \quad (4-9)$$

For the radial,  $O_p$  is slightly smaller than  $nS_p$ . The difference between  $O_p$  and  $nS_p$  is a few microns in the radial configuration in most cases. It is smaller than a sub-pixel. This means that  $j = 1$  and  $S_p/2 \leq R < S_p$ . In this case,  $A$  is given as  $k + j (= 1) = n$ . Hence Eq. (4-9) is still valid. Equation (4-9) relates the moiré fringe periods with the system parameters of the contact-type multiview 3-D displays. It informs that the periods of the moiré fringes appearing at the displays are also affected by the viewing distance and focal length of VZFO. Equation (4-9) indicates that as  $f/d$  becomes smaller, i.e., the designed viewing distance  $d$  increases, the moiré fringe period will be slightly increased.

### 4.3 Experimental set-up

With the equations developed at section 2, the moiré fringe periods are calculated for five different VZFO line patterns having the nominal period values of 0.4833 mm, 3.4 mm, 1.608 mm, 1.4499 mm and 1.4509 mm as shown in Table 4-1. VZFO line patterns are drawn on polystyrene films having thickness of 0.18 mm with a photoplotter (UCAMCO Calibrator NaNOII series). The manufacturer's specification indicates that it has more than 20,000 DPI (Dot per Inch) resolution [4-14]. This resolution value corresponds to near 0.001 mm. All these films, except 1.608 mm, are superposed on the 42-inch monitor having a full HD resolution (1920 X 1080). To

stick the film on the glass surface of the monitor as evenly as possible, a transparent plastic plate is fixed to the monitor and the film is inserted in between the plate and the glass surface. The thickness of VZFO is set to 0.68 mm by considering the protection glass thickness of the monitor, 0.5 mm. The refractive index of the VZFO is set to 1.5412 by taking arithmetic average of the refractive indexes of the film (1.6) and the glass (1.52). The film length of 0.4833 mm and 3.4 mm line periods is 750 mm and others 830 mm. For the 1.608 mm, the film was bended to fit to the monitor size. The sub-pixel pitch of the monitor is 0.1611  $\mu\text{m}$ . For the 1.608 mm, it is superposed on a 28-inch UHD monitor with the resolution 3840 X 2160. The nominal value of the pixel size of the monitor is 0.16 mm but in this paper 0.1617 mm is used by dividing its nominal width value 620.93 mm by its horizontal pixel resolution 3840. This pixel value matches well with current experiment. The pattern period values indicate that 0.4833 mm and 1.4499 mm are corresponding to integer multiple of a pixel/a sub-pixel size, i.e., 0.4833 mm a pixel (three sub-pixels) and 1.4499 mm 3 pixels (9 sub-pixels), 3.4 mm ( $3.4/0.1611 = 21 \times 0.1611 + 0.0169$  mm) and 1.4509 mm ( $1.4509/0.1611 = 9 \times 0.1611 + 0.001$  mm) represent  $0 \leq R \leq S_p/2$  case and 1.608 mm ( $1.608/0.1617 = 9 \times 0.1617 + 0.1527$  mm)  $S_p/2 \leq R < S_p$  case. For the cases of 0.4833 mm and 3.4 mm, two different line thicknesses of 0.0805 mm and 0.4028 mm for 0.4833 mm, and 0.3222 mm and 3.0778 mm for 3.4 mm are used. These values are to demonstrate the line thickness effects on moiré fringe colors and their contrasts. All these values are tabulated in Table 1 with the fringe periods obtained with Eq. (4-1) and line thickness values. In table 4-2, the symbols used in this paper are summarized.

Table 4-1. Fringe Periods calculated by equation and symbol definition

Order	Line period(mm) ( $O_p$ )	Line Thickness (mm)	Fringe Period when t = 0 (mm) ( $P_M$ )	Pixel Size (mm) ( $P_p$ )	Remark (Fth: Film Length)
1	0.4833	0.0805	Infinity	0.4833	42 inch panel Fth=750 mm
		0.4028	Infinity		
2	3.4	3.0778	97.232	0.4833	42 inch panel Fth=750 mm
		0.3222	97.232		
3	1.4499	0.2415	Infinity	0.4833	Fth=830 mm
4	1.4509	0.2415	701.22	0.4833	Fth=830 mm
5	1.608	1.072	28.8904	0.1617	UHD 28 inch

Table 4-2. Symbol definition

Symbol	Definition	Symbol	Definition
$P_p$	Pixel size	d	Designed viewing distance
$S_p$	Pitch of a sub-pixel	f	Focal length of VZFO
$O_p$	Period of elemental optics	n	Number of Multiview images loaded on the panel
R	Remainder		

The color moiré fringes appearing when each of the films on Table 4-1 is superposed on its appropriate monitor are viewed with a NIKON camera (D700) equipped with a wide field of view objective (G-type AF-S zoom – Nikkor lens) [4-15]. The optical axis of the camera is aligned to the normal direction of the monitor. The viewing distance, i.e., the camera distance from the pattern plane of the VZFO is set to 500 mm and 1,000 mm to show the fringe period variations with the viewing distance and the accuracy of Eq. (4-4). The viewing distance of the moiré fringes is defined to the pattern plane where the fringes are formed.

#### 4.4 Experimental results

There are several factors of reducing the moiré fringe contrasts; 1) decrease in the line thickness, 2) the presence of extra plastic plate to hold the film tight to the monitor and 3) the camera imaging. The reduction will be more as the viewing distance increases. Furthermore, the boundary between different colors can be hardly defined with the film because it cannot be attached completely to the monitor surface for all its length. This makes the direct comparison of the moiré fringe periods with the calculated by Eq. (4-3) difficult. To ease this difficulty, moiré fringes appearing when the films of different line periods and thicknesses are superposed on the monitors, is simulated and displayed simultaneously with the films on the monitors. In this way, the colors and the boundary between different colors of two moiré fringes can be easily compared. The waveform of the calculated moiré fringe periods by Eq. (4-3) is drawn above the original simulated moiré fringes in the following figures. Both the waveform and the simulated fringes are calculated to cover two times of the monitor widths to show at least a complete moiré fringe period. The starting point of calculating each moiré fringe and its period are the center point of the monitor. A vertical line in the center of the waveform which depicts the calculated fringe periods in

each of the following figures, represents the center point. If the two moiré fringes on the monitor match to each other and the waveform also matches with the simulated, it can be said that Eq. (4-3) is a correct formula for predicting the periods of the moiré fringes induced when two regular pattern plates having a large difference in their periods are superposed. The lengths of the films are specified by two arrow headed lines in following figures to identify clearly the moiré fringes induced by the films. The moiré fringe simulation has been done with the same technique used in reference 4-2.

Figure 4-2 compares moiré fringes between the simulated and experimentally obtained (Noted by “with film” in each figure) to verify the accuracy of the fringe periods calculated by Eq. (4-4) for the case when the film with the line period 3.4 mm is superposed on the 42-inch monitor. Fig. 4-2(a) and (b) is for comparing the relative brightness of the moiré fringes, i.e., the contrast of the moiré fringes for two different line thicknesses of 3.0776 mm and 0.3222 mm viewed at viewing distances of 500 mm and 1,000 mm, respectively. As shown in Fig. 4-2 (a) and (b), the 0.3222 mm reveals barely visible moiré fringes but for the 3.0776 mm clearly visible moiré fringes. The simulated moiré fringes on the monitor look lost their details compared with the original and even different. However, the two moiré fringes on the monitor look matched closely in both colors and their boundaries.

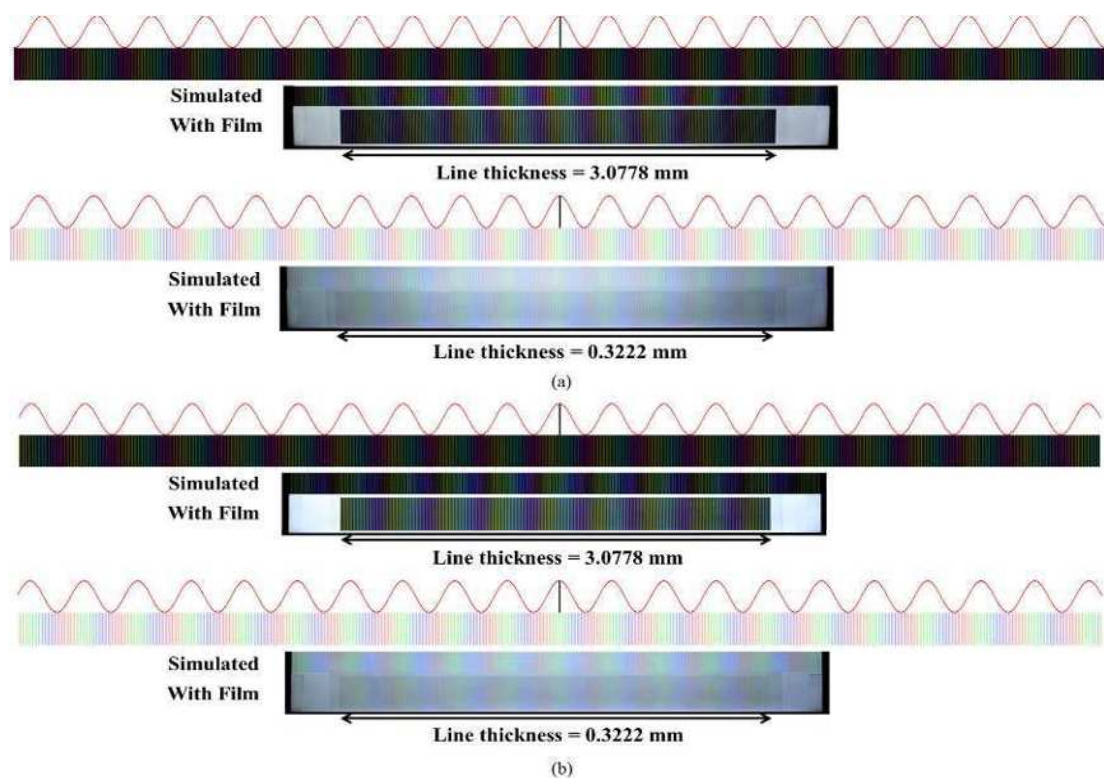


Fig. 4-2. Moiré fringes for VZFO line period of 3.4 mm: (a) Viewed at 500 mm and (b) Viewed at 1,000 mm.

Since the line thickness of 3.0776 mm brings the slit width of 0.3222 mm, and 0.3222 mm 3.0776 mm, the former can be considered as representing the parallax barrier and the latter the lenticular. Figure 4-2 (a) and (b) informs that the parallax barrier can bring much more visible moirés than the lenticular, though the simulated moiré fringes on the monitor appears fainter than the original due to the photographing, the color compositions and periods of the moiré fringes from the simulated and the film, match well to each other at both viewing distances. The periods of the moiré fringes are plotted on the top of each simulated moiré fringes as a waveform. Each period of the waveform represents exactly one of the repeatedly appearing color groups, i.e., one of the moiré fringes. As mentioned before, the moiré fringes are calculated for two times of the monitor width ( $0.4833 \text{ mm} \times 1920 \times 2 \cong 1,856 \text{ mm}$ ), However, since the camera's optical axis corresponds to the normal direction of the monitor surface, the periods will be symmetric along a line drawn vertically at the center of the monitor. The vertical line in each waveform represents the center line. The number of moiré fringes is slightly more than 21 for the viewing distance 500 mm but less than 21 for 1,000mm. As expected, the fringe periods are affected by the viewing distances but not by the line thickness. The fringe periods are slightly increased with increasing distances. In Fig. 4-3, the moiré fringe periods between peak points of the waveforms along the right (left) side of the center line are depicted for both viewing distances. The horizontal axis represents fringe numbers counted from the center and the vertical axis period of each fringe. Figure 4-3 indicates that the periods increase as away from the center line. This clearly demonstrates that the fringes are negatively chirped. The periods of the moiré fringes for the 500 mm is shorter than those of the 1,000 mm until  $x \approx 750 \text{ mm}$ , but they surpass those for the 1,000 mm for farther than the 750 mm. This is because the period increment is more for the 500 mm than the 1,000 mm. As the viewing angle increases, the viewing angle increment induced by a pixel distance affects the angle less and less. Hence the period increment will be almost saturated as the distance increases further.

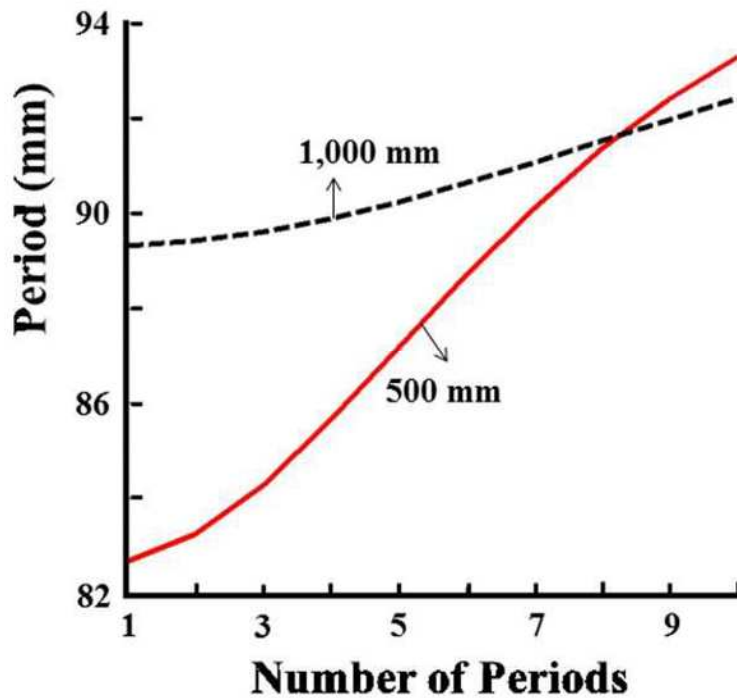


Fig. 4-3. Moiré fringe periods for VZFO line period of 3.4 mm.

Figures 4-4, 4-5 and 4-6 also compare moiré fringes between the simulated and experimentally obtained as in Fig. 4-2. Figure 4-4 is the case when the line periods are integer multiples of the 42-inch monitor's pixel/sub-pixel pitch. The films with the line periods of 0.4833 mm and 1.4499 mm are the case for the integer multiples as shown in Table 1. Figure 4-4(a) and (b) is the 0.4833 mm case viewed at 500 mm and 1,000mm, respectively, and each of them contains the moiré fringes for two different line thickness (Width) of 0.4028 mm and 0.0805 mm to compare the fringe contrasts. Figure 4(c) depicts the 1.4499 mm case when the moiré fringes are viewed at both 500 mm and 1,000mm distances. These line periods should noninducing moiré fringes when the VZFO has no thickness as indicated by Eq. (4-1). However, Fig. 4-4 shows distinctive color moiré fringes. These fringes are caused by the thickness of the VZFO. Figure 4-4(a) and (b) also shows that the line thickness difference induces the difference in color compositions and contrasts of the moiré fringes. The distinctive R. G. B colors for the line thickness of 0.4028 mm are much more visible than the sky blue, yellow and violet for the 0.0805 mm. Since these colors appear repeatedly, they are forming a moiré fringe for the given line thickness. Figure 4-4(c) also reveals low contrast moiré fringes due to relatively narrow lines, i.e., 0.2415 mm compared with the line period.

The colors consisted of a moiré fringe are not different from the line thickness 0.0805 mm of the 0.4833 mm, except more visible color transition regions. In Fig. 4-4, the color compositions of the moiré fringes from the simulated and the film match well to each other at both viewing distances but the color boundaries are not well defined for the film. This results a small mismatch between the simulated and the film, especially for the 0.0805 mm of the 0.4833 mm and the 1.4499 mm cases when they are viewed at 1,000mm. Added on these mismatches, the low contrast of the moiré fringes on the monitor makes hard to recognize them, even for the simulated. These mismatches will always be there because gaps and pattern line mismatches between the film and the monitor surface can be hardly avoidable. The film does not have a perfect flatness. In this regard, it is considered that moiré fringes on the simulated and the film match well. As specified by the waveform, a period of the waveform for each case covers exactly the three colors representing a moiré fringe. The periods of the moiré fringes are given as 602.432 mm and 1,204.964 mm for the 500 mm and the 1,000mm, respectively. The fringe period of the 1,000mm is slightly more than two times of that of 500 mm and much longer than the monitor width. The fringe periods of the moirés in Fig. 4-4(c) are not different from those of Fig. 4-4(a) and (b) as indicated by Eq. (4-3). For the case of the viewing distance 500 mm, the second peak of the waveform appears at 990.771 mm from the center line. Since the distance between the 1st maximum and minimum points of the waveform is 301.216 mm, the distance between the 1st minimum and 2nd maximum points will be 689.555 mm. This value is even bigger than the first fringe period 602.432 mm. This indicates that the period of the next fringe will be longer than the first. The moiré fringes are chirped. The fringes for the 1,000mm will also be chirped. Figures 4-2 and 4-4 clearly indicate that the contrast of the moiré fringes decreases as the line thickness decreases for the given VZFO line period  $O_p$ .

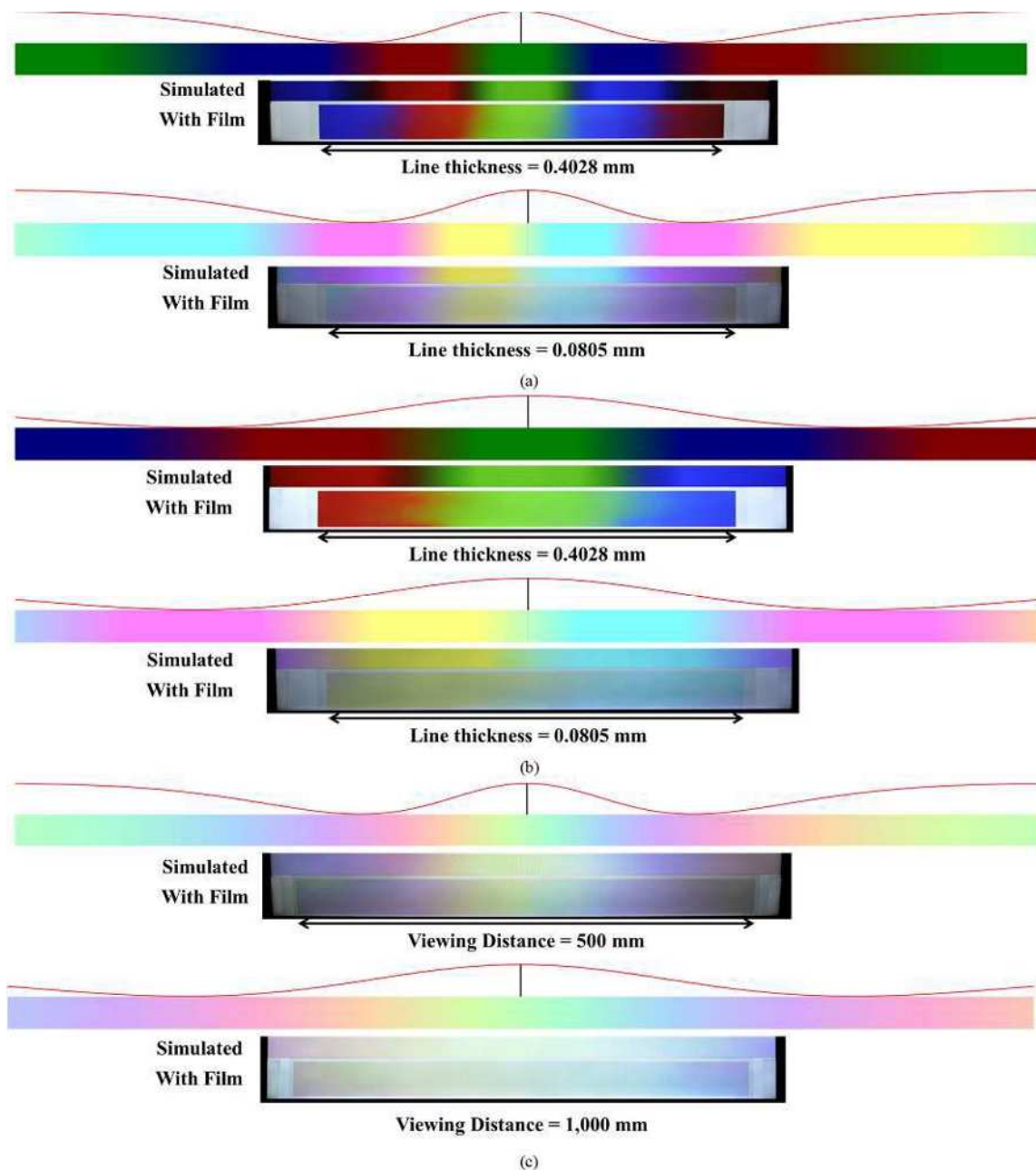


Fig. 4-4. Moiré fringes for the case when the VZFO line period is integer multiples of a sub-pixel pitch

The moiré fringes for the line period of 1.4509 mm are depicted in Fig. 4-5 for viewing distances of 500 mm and 1,000mm. Since the 1.4509 mm is almost the same as the 1.4499 mm and the line thickness 0.2415 mm is the same as Fig. 4-4(c), the colors consisting of the moiré fringes are not different from those in Fig. 4-4(c), except their shorter periods. The moiré fringes on the monitor are not clearly visible as in Fig. 4-4(c) but they are still comparable. The colors and color regions of the moiré fringes match well to each other. The period of the moiré

fringe in the mid area is increased to 369.87 mm (455.02 mm) from 312.46 mm (429.89 mm) at the viewing distance 500 mm (1,000mm). The periods specified by the waveforms are increasing as the viewing angle/the viewing distance increases. However, each of these periods covers exactly the three colors of sky blue, yellow and violet. This behavior of the moiré fringe is the same as that in Figs. 4-2 and 4-4. The moiré fringes for the 1.608 mm which is superposed on the UHD panel are depicted in Fig. 4-6 for two viewing distances of 500 mm and 1,000mm. This is the case of  $A = k + 1$  according to Eq. (4-2), since  $1.608 \text{ mm} = 10 \times 0.1617 \text{ mm} - 0.009 \text{ mm}$ . This case is different from Figs. 4-2 and 4-5 which represent  $A = k$  cases. The  $-0.009 \text{ mm}$  means that the period of the top plate (VZFO) pattern is bigger than that of the bottom plate (Monitor) pattern.

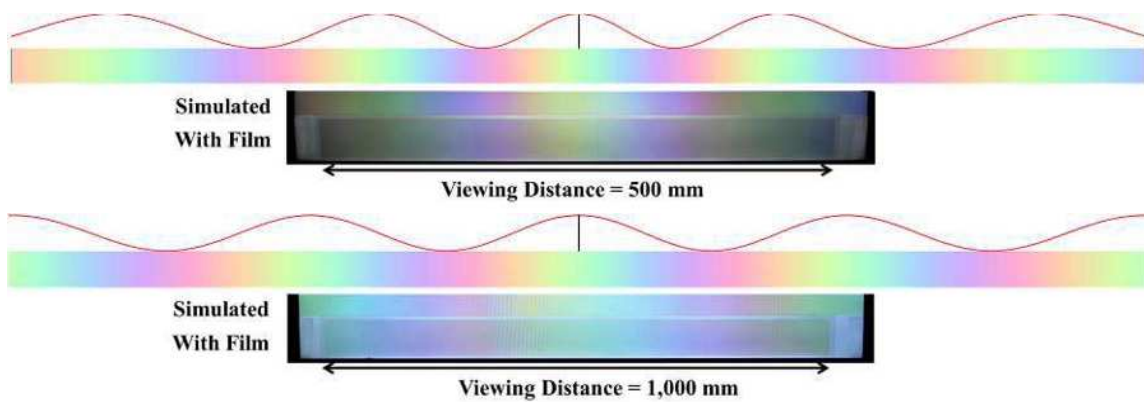


Fig. 4-5. Moiré fringes for VZFO line period of 1.4509 mm.

Figure 4-6 shows a very visible color pattern which is appearing repeatedly. The color pattern is a moiré fringe. There are some fringe distortions due to the bending of the films at the right side and also the fringes from the film are slightly shifted to the left compared with the simulated for both distances, though 1,000 mm reveals less shifting. This shifting is hardly adjusted to minimize the distortions by the bending, even with the plastic plate to tighten the film on the monitor.

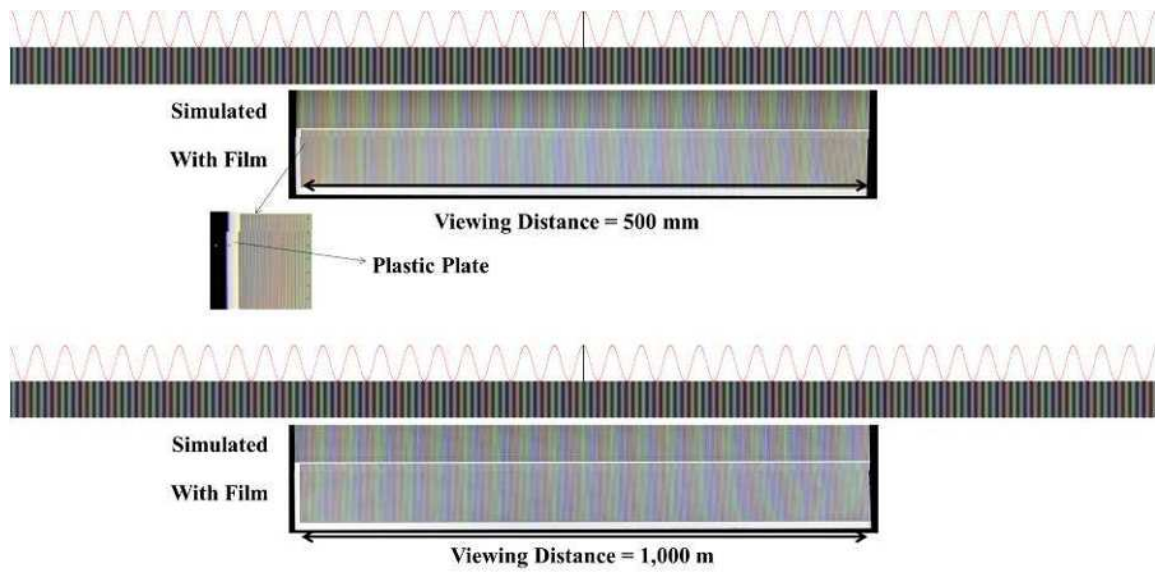


Fig. 4-6. Moiré fringes for VZFO line period of 1.608 mm.

Other than this shifting, the colors and periods of the moiré fringes from the film and the simulated are closely matched to each other. Each period of the waveform of the given distance are also accurately representing the length of the color pattern. There are approximately 38 moiré fringes for the distance 500 mm and 40 for 1,000mm. This means that the periods of the moiré fringes for the 500 mm are slightly longer than those for the 1,000mm. The periods of the moiré fringes for the 500 mm and 1,000mm are compared in Fig. 4-7. In Fig. 4-7, the moiré fringe periods between peak points of the waveforms along the right (left) side of the center line are depicted for both viewing distances. The horizontal axis represents fringe numbers counted from the center and the vertical axis period of each fringe. The periods decrease as away from the center line. Hence the fringes are positively chirped. The periods of the moiré fringes for the 500 mm is longer than those of the 1,000mm to the simulated distance range but they become closer to each other as the distance increases. The periods for the 500 mm will be smaller than those for the 1,000mm as the distance increases further. This is because the period decrement is more for the 500 mm than the 1,000mm. The fringe behaviors of Fig. 4-6 are completely opposite to the those of Figs. 4-2 and 4-5.

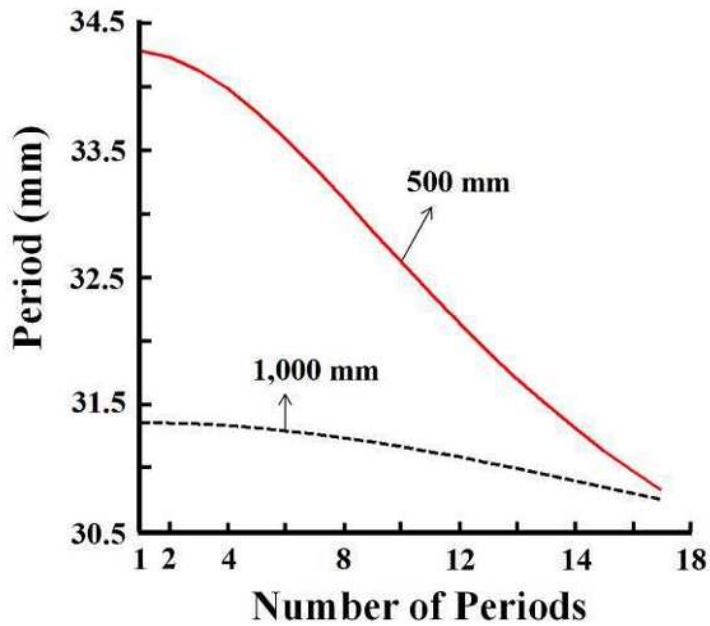


Fig. 4-7. Moiré fringe periods for VZFO line period of 1.608 mm.

#### 4.5 Conclusion

The color moiré fringes appearing in the contact-type 3-D displays, can be characterized by equation (4-4). This is because Eq. (4-4) can accurately predict the periods of the color moiré fringes. The equation informs that 1) the moiré fringes are chirped, 2) when the period of a line pattern is any integer multiple of another line pattern, the moiré fringe period is the same without regarding to the integer number and 3) the behaviors of the moiré fringes when  $R$ , i.e., the remainder is less than an half of the sub-pixel pitch are opposite to those when  $R$  is more than an half. Furthermore, the contrast of the moiré fringes decreases as the line thickness decreases for a given VZFO line period.

## 5 Simulation of slanted color moirés in IP-type 3-D displays

### 5.1 Introduction

The moirés appearing at the IP-type 3-D and light field displays are color moirés due to the periodic blocking of the pixel pattern in the display panel by the Viewing zone forming optics (VZFO) line pattern [5-1]. Since the moirés are the worst factor of deteriorating image quality in the 3-D displays, it is desired to eliminate them completely. But it is not possible in current 3-D displays because they are inherent to the displays due to their structural requirements. Hence many methods have been developed to minimize the color moirés [5-2]-[5-8] but they are mainly grouped into two such as 1) slanting the VZFO line pattern [5-2]-[5-5] and 2) adding a diffuser between the panel and the VZFO [5-6]-[5-8]. These methods are effective in reducing the visual contrast of the moirés but they require a cost of increasing crosstalk between different view images. Between the two methods, slanting the VZFO line pattern to have a certain angle with the pixel pattern in the panel has been popularly used by many researchers [5-2]-[5-5], [5-9] due to its effectiveness in correcting the unbalance between horizontal and vertical resolutions of each view image in the horizontal parallax only 3-D displays [5-9], though the number of active pixels will be reduced due to the fact that the pixels along the boundary lines are divided into two parts for two different viewing regions. It is known that when the angle is around  $9.4^\circ$  for the panels with a square type pixel arrangement, the horizontal resolution of each view image is increased three times by sacrificing the vertical resolution to the same amount. However, the angle is not the one to minimize the moiré contrast because the minimization can be attained at the larger slanting angle than the  $9.4^\circ$ . Many slanting angles such as near  $26^\circ$  [5-2],  $17^\circ$  [5-3],  $24.1^\circ$  [5-4] and  $22.6^\circ$  [5-5] has been reported as the minimization angles for the case of using a lenticular or microlens array for the VZFO. These angles are found experimentally and fit only for reporters' displays without considering the thickness of the VZFO, i.e. the chirping effect, their applicability's to other 3-D displays are not known. The angle  $26^\circ$  is actually found mathematically as the angle maximizing the moiré fringe period under the condition that the period of the VZFO's line pattern is almost the same as that of the pixel pattern. Hence the angle cannot guarantee that it can minimize the color moirés in typical IP-type multiview 3-D and light field displays because the period of the VZFO's line pattern is larger than that of the pixel pattern. However, since it is true that the moirés decrease as the slanting angle increases, there must be other reasons why the moiré

contrast reduces as the slanting angle increases. This reason can be found by devising an algorithm of simulating the behaviors of moirés for the slanting angle range of  $0^\circ$  to  $45^\circ$ . But no algorithm is available so far, except the  $0^\circ$  case [5-1].

This paper introduces an algorithm to simulate the slanting color moirés for the angle range of  $0^\circ$  to  $45^\circ$ , verifies experimentally the algorithm's accuracy with use a grating, and finds the reason of the moiré contrast reduction with the increasing slanting angles.

## **5.2 Behaviors of the color moirés**

The color moirés appearing at the IP-type multiview 3-D and light field displays behave differently from those in two overlapped line gratings. In the line gratings, the lines in the top grating are overlapped completely, partly to those in bottom grating and/or block the spaces between lines of the top to form the black and white moirés [5-8]. However, in the 3-D displays, the color moirés are induced by periodic blocking of whole or parts of the pixel pattern in a display panel by the lines in the VZFO line pattern. Among the frequently used VZFOs such as lenticular, microlens array and parallax barrier plates, the lines in a lenticular and microlens array are boundary lines between elemental lenses, and those in a parallax barrier are the barrier lines. These lines are not directly on the top of the pixel pattern in the panel but through the medium forming the VZFO and the cover glass of the panel. The medium has a thickness to make the focal length of the VZFO, i.e., elemental lenses correspond to the sum of its thickness and the cover glass's thickness. Since when a viewer views the 3-D display, he/she can see the pixels on the panel through the VZFO, some pixels or parts of a pixel will be blocked by the boundary or barrier lines. The amount of the blockings depends on the line thicknesses, i.e., the line widths. The thicknesses of the boundary lines are much thinner than those of the barrier lines. When each of the lines covers more than a pixel, the completely covered pixels appear to be dark. However, the partly blocked pixels change their colors and brightness, because the color brightness of one or all sub-pixels consisting of a pixel will be reduced by the blockings. As a consequence, the color of each pixel will be viewed differently from its original color. Since the lines are periodically arranged, the color changes are also appearing periodically. This is the color moirés in the 3-D displays. The periods of these color moirés cannot be calculated with the typical beat frequency formula [5-11] because 1) the period of the VZFO line pattern is much longer than the pixel pitch and 2) the color moirés are

chirped, i.e., the periods of the color moirés either reduce or increase as the viewing angle increases due to the VZFO thickness and the VZFO medium's refractive index [5-12]. The beat frequency formula requires that the period difference between the VZFO and pixel line pattern should be smaller than the period of the pixel line pattern but the VZFO's line period is at least several times of the pixel period in a typical IP-type multiview 3-D display. The period difference between the VZFO lines and pixels is bigger than the pixels. Hence the beat frequency formula cannot be applied to the color moirés. This is why a new formula of calculating the period was developed by dividing the line period by an integer which is obtained from dividing the line period by the subpixel pitch [5-13]. But this new formula is only valid for the small size panels because the color moirés are chirped. The chirping is the result of virtual contraction of pixel/subpixel pitch when viewers view the display because the pixel pattern is viewed through the VZFO. Hence the color moirés in 3-D displays are not even physical but also visual phenomena. Since the pixel/subpixel is refracted to the direction of viewers' eyes, the pixel/subpixel pitch is perceived as smaller than its real size. The amount of the virtual contraction will be more as the viewing angle increases, i.e., the panel size increases. However, it becomes smaller as the viewing distance increases because the viewing angle reduces as the viewing distance increases. This changing nature of the moirés with viewing angle and position makes them more recognizable. This makes the color moirés very cumbersome in IP-type multiview 3-D and light field displays because of the moirés' hostile influence to their image quality [5-1].

### 5.3 Moiré fringe simulation

As mentioned above, the color moirés are created by the color changes incurred by whole or partly blocked subpixels by the lines in the VZFO line pattern. The blocking reduces the brightness of the blocked sub-pixels in proportional to the blocked areas. This brightness change is the main reason of the pixel color change. Hence to simulate the color moirés, it is necessary to calculate the blocked area. Calculation of the area will not be hard because the lines in VZFO line pattern are in parallel to each other. The blocked area is calculated as followings: When the lines are arranged vertically, i.e., when the slanting angle is  $0^\circ$ , the line can cover either a sub-pixel or two sub-pixels, for the case when the line thickness is smaller than a sub-pixel pitch. For a sub-pixel case, when the full brightness of each sub-pixel which makes a pixel to have a white color is 1.0, the blocked area  $A_r$  and the reduced color brightness  $B_R$  due to the blocked area are calculated as,

$$A_r = P_p l_w : i = 1 \text{ to } N$$

$$B_R = \{P_p S_p(i \text{ or } i + j) - A_r\} / P_p S_p(i \text{ or } i + j) \quad (5-1)$$

where  $P_p, S_p(i)$  and  $l_w$  are a pixel pitch, its sub-pixel pitch and a line width of the VZFO line pattern, respectively. Since the pixel pattern is chirped, each sub-pixel pitch is different from its neighbors. For the two sub-pixels case, if  $a$  % and  $b$  % ( $a + b = 100\%$ ) of  $l_w$  cover two adjacent sub-pixels, the blocked area of each sub-pixel is calculated as  $aA_r$  and  $bA_r$ , respectively. The color brightness of two adjacent sub-pixels are obtained by replacing  $A_r$  in equation (5-1) with  $aA_r$  and  $bA_r$ . When the line width is more than a sub-pixel pitch, the blocked areas of sub-pixels crossed by the line edges are calculated by equation (1) and those sub-pixels which are within the line width  $l_w$  will be considered as having the brightness value of 0.0. If the sub-pixels within the open slit area is completely uncovered by  $l_w$ , they have the brightness value of 1.0. Equation (5-1) is repeated for the next lines. For the case when the VZFO line pattern is slanted with an angle, it is necessary to consider the crossed sub-pixels by the line edges during its moving to a pixel height to find the blocked area. In this case, the line width and the line period become  $l'_w = l_w / \cos \theta$  and  $O'_p = O_p / \cos \theta$ , respectively. Figure 1 shows the case when the VZFO line pattern with 4 lines is crossed by a pixel line in horizontal direction with an angle  $\theta$ . The line width of each of 4 lines is longer than that of a sub-pixel. If the left edge of the line 2 is crossed at the bottom of the sub-pixel  $S_p(i)$  and the top of the sub-pixel  $S_p(i + i_1)$  at the points A1 and A2, respectively, and at points C1 and D1 with the left edge lines of sub-pixels  $S_p(i + 1)$  and  $S_p(i + i_1)$ , respectively, the areas under the left edge of the line 2 for the sub-pixels  $S_p(i)$  to  $S_p(i + i_1)$  are calculated as following: If the distance between the point A1 to the right side edge of  $S_p(i)$  is  $l_1$  and A2 is  $l_2$  distance away from the left side edge of  $S_p(i + i_1)$ , the areas under the line edge are calculated as,

$$SP_{SUM} = \sum_{k=1}^{i_1-1} S_p(k), SUMA = l_1 + l_2 + SP_{SUM}$$

$$\bar{C}_1 = P_p l_1 / SUMA, \bar{D}_1 = P_p l_2 / SUMA$$

$$A_{S_p(i)} = 0.5 l_1 \bar{C}_1, A_{S_p(i+i_1)} = P_p S_p(i + i_1) - 0.5 l_2 \bar{D}_1$$

$$A_{S_p(i+j)} = l_1 \bar{C}_1 + 0.5 \frac{P_p - \bar{C}_1 - \bar{D}_1}{SP_{SUM}} (S_p(i + j))^2 : j = 1$$

$$A_{S_p(i+j)} = l_1 \bar{C}_1 + \frac{P_p - \bar{C}_1 - \bar{D}_1}{SP_{SUM}} \{ \sum_{k=1}^{j-1} (S_p(i + k))^2 + 0.5 (S_p(i + j))^2 \} : j = 2 \text{ to } i_1 - 1 \quad (5-2)$$

where  $\bar{C}_1$  and  $\bar{D}_1$  are the distances of the points C1 from the bottom of the pixel line and D1 from top of the pixel line, respectively. The areas of sub-pixels under the right-side edge of the line 2 are also calculated the same way as the left side edge. If the right edge of the line 2 in the VZFO line pattern is crossed at the bottom of the sub-pixel  $S_p(i + i_2)$  and the top of the sub-pixel  $S_p(i + i_3)$  at the points B1 and B2, respectively, and at points C2 and D2 with the left edge lines of sub-pixels  $S_p(i + i_2 + 1)$  and  $S_p(i + i_3)$ , respectively, the areas under the right edge of the line 2 for the sub-pixels  $S_p(i + i_2)$  to  $S_p(i + i_3)$  are calculated as following: If the distance between the point B1 to the right edge of  $S_p(i + i_2)$  is  $l_3$  and B2 is  $l_4$  distance away from the left edge of  $S_p(i + i_3)$ , the areas under the right edge are calculated as,

$$\begin{aligned}
SP_{SUM} &= \sum_{k=i_2+1}^{i_3-1} S_p(k), SUMA = l_3 + l_4 + SP_{SUM} \\
\bar{C}_2 &= P_p l_3 / SUMA, \bar{D}_2 = P_p l_4 / SUMA \\
A_{S_p(i+i_2)} &= 0.5 l_3 \bar{C}_2, A_{S_p(i+i_3)} = P_p S_p(i + i_3) - 0.5 l_4 \bar{D}_2 \\
A_{S_p(i+j)} &= l_3 \bar{C}_2 + \frac{P_p - \bar{C}_2 - \bar{D}_2}{SP_{SUM}} 0.5 (S_p(i + j))^2 : j = i_2 + 1 \\
A_{S_p(i+j)} &= l_3 \bar{C}_2 + \frac{P_p - \bar{C}_2 - \bar{D}_2}{SP_{SUM}} \{ \sum_{k=i_2+1}^{j-1} (S_p(i + k))^2 + 0.5 (S_p(i + j))^2 \} : j = i_2 + 2 \text{ to } i_3 - 1 \quad (5-3)
\end{aligned}$$

where  $\bar{C}_2$  and  $\bar{D}_2$  are the distances of the points C2 from the bottom of the pixel line and D2 from top of the pixel line, respectively. From equation (2) and equation (3), the blocked area of each sub-pixel by the lines of the VZFO line pattern is calculated as,

$$\begin{aligned}
A_r &= A_{S_p(j)} + P_p S_p(j) - A'_{S_p(j)} : j = i \text{ to } i_0 \\
A_r &= A_{S_p(j)} : j = i_0 + 1 \text{ to } i_4 - 1 \text{ if } i_2 = i_1 + 1 \\
A_r &= A_{S_p(j)} : j = i_0 + 1 \text{ to } i_1 \text{ or } j = i_2 \text{ to } i_4 - 1, A_r = 1.0 : j = i_1 + 1 \text{ to } i_2 - 1 \text{ if } i_2 > i_1 + 1 \\
A_r &= P_p S_p(j) - A_{S_p(j)} + A''_{S_p(j)} : j = i_4 \text{ to } i_3 \quad (5-4)
\end{aligned}$$

where  $A'_{S_p(j)}$  and  $A''_{S_p(j)}$  are the sub-pixel areas under the right edge of line 1 and the left edge of line 3, respectively and the sub-pixel locations specified by  $i_0$  and  $i_4$  are shown in Figure 1. The equation (5-4) is repeated for other lines. The number of sub-pixels corresponding to  $i_1 - i$  ( $i_3 - i_2$ ) cannot be more than 5 for the slanting angle range of  $0^\circ$  to  $45^\circ$  even the chirping effect is considered because the slanting angles of crossing one, two and three sub-pixels in horizontal direction for a pixel height are approximately given as  $18.4^\circ$

$(\tan^{-1}(1/3))$ ,  $33.7^\circ(\tan^{-1}(2/3))$  and  $45^\circ(\tan^{-1}(3/3))$ , respectively, However, for the case of the slanting angle  $1^\circ$ , the line crosses around 57 the same color sub-pixels in vertical direction within a sub-pixel width. This means that the color moirés become more visible as the angle decreases.

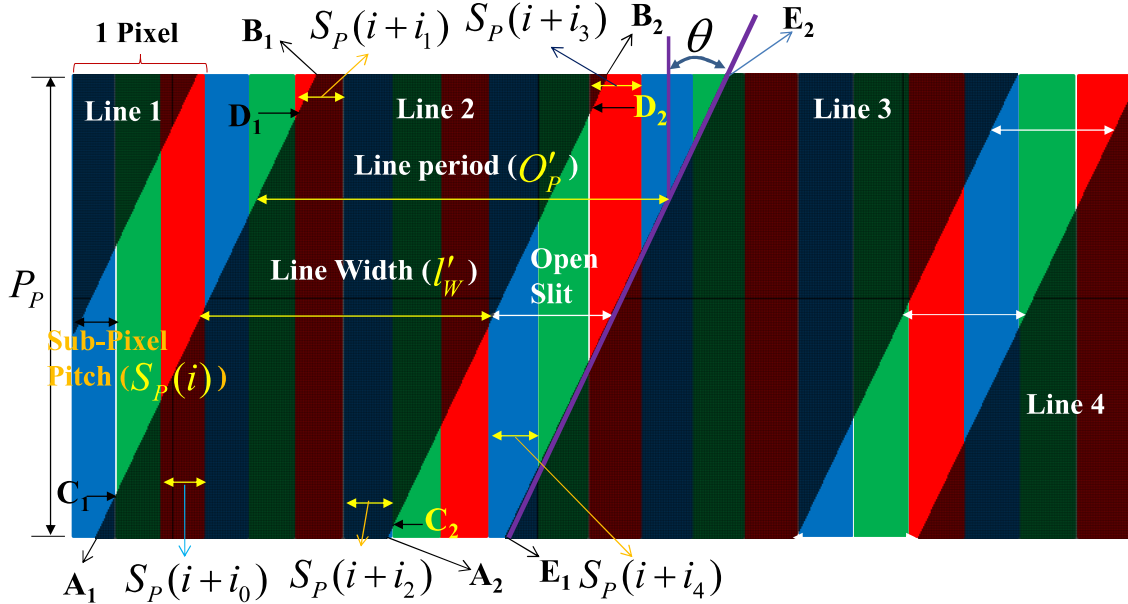


Fig. 5-1. A VZFO line pattern on a pixel pattern

#### 5.4 Moiré fringe simulation

In Figures 5-2 and 5-3, the color moirés viewed at 500 mm distance from left edge of the display panel are simulated from Equations. (5-2) to (5-4) and they are compared with those from a grating for slanting angles of  $1^\circ$ ,  $5^\circ$ ,  $15^\circ$ ,  $25^\circ$ ,  $35^\circ$  and  $45^\circ$ . The grating is a line array of  $O_p = 3.4$  mm and  $l_w = 3.2389$  mm, printed on a polyester film with thickness of 0.18 mm. It has the refractive index of 1.6, Since the grating is directly layered on a 42-inch Full HD monitor from LG and surface glass thickness of the monitor is 0.5 mm with refractive index of 1.52, the thickness of the VZFO medium is calculated as 0.68 mm with refractive index of 1.54 as the arithmetic average.

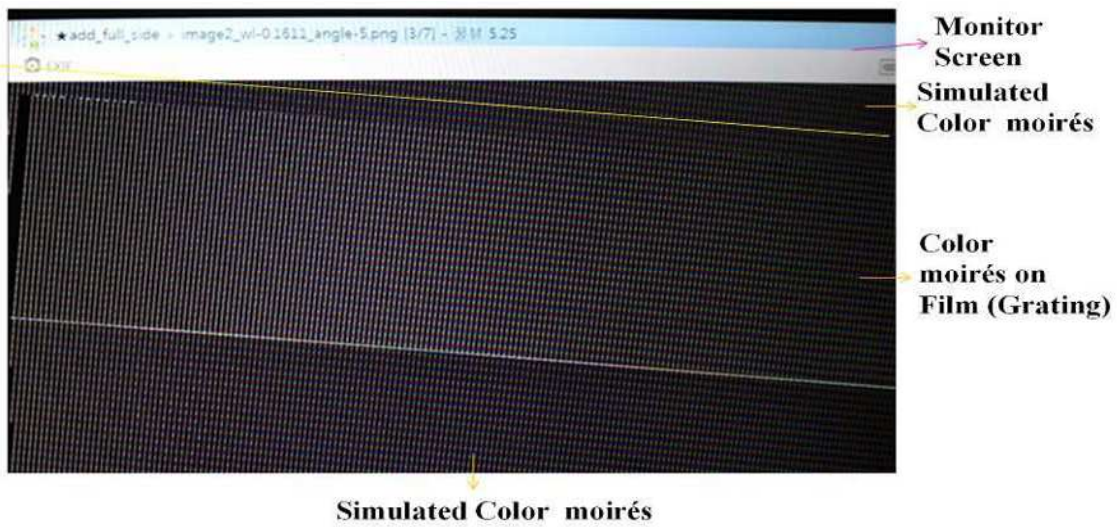


Fig. 5-2. Comparisons of color moirés from simulated and a grating on a panel for 5° slanting angle.

The grating is selected because it reveals the color moirés with a high contrast through the slanting angle range. For the comparison, the part of the simulated color moirés corresponding to the area of the grating are cut to display the moirés to the side of those from the grating. In this way, a line by line comparison between the simulated and the grating color moirés can be done. Figure 5-2 is the camera image of the color moirés on the monitor for the 5° slanting angle. The camera is set at 500 mm distance from the monitor surface by aligning its optical axis normal to the center left edge of the monitor to show the chirping in the color moiré fringes from the grating. The distance between color lines and colors forming each line are the same for both moirés. In Figure 5-3, comparisons between color moirés at slanting angles such as 1°, 15°, 25°, 35° and 45° are done. The image for each angle is magnified and its small part is cut to include both color moirés from the simulated and the grating to show the matching details between them. The top right part of each image is the color moirés from the grating. Figure 5-3 clearly shows that the moirés from the simulation and the grating are the same to each other for the slanting angles, except a small color differences caused by the extra light reflection from the film surface. Figure 5-3 also shows that the colors become almost invisible for the angles not less than 15°. However, it is difficult to tell that at what angle range the contrast of the color moirés is minimized because Figure 5-3 is the camera images. To find the angle range, the magnified image of the simulated color moirés for the slanting angles of 17°, 26°, 35° and 45° are compared.

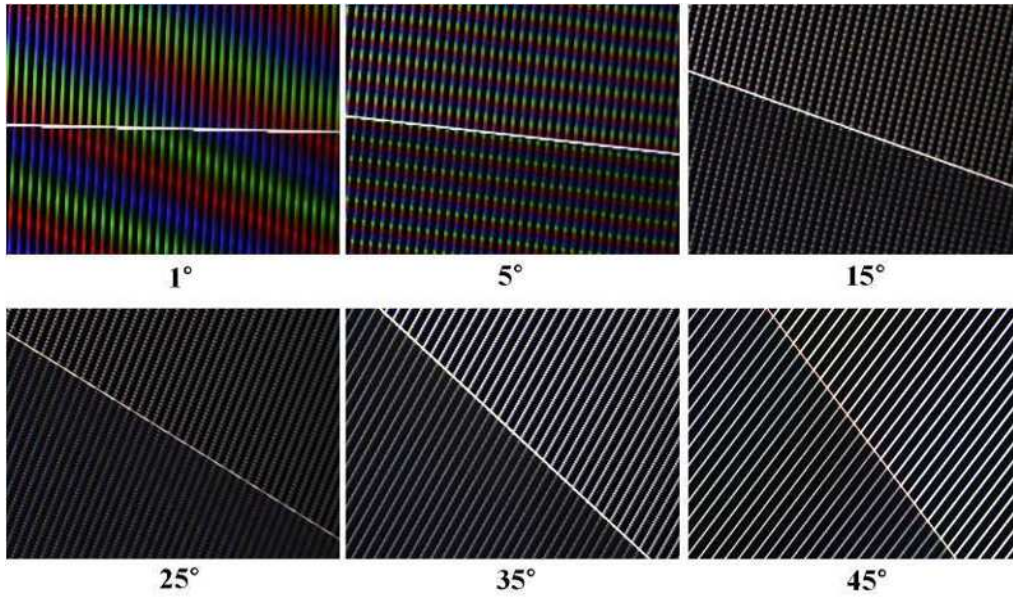


Fig. 5-3. Comparisons of color moirés from simulated and a grating on a panel for other slanting angles.

To compare color contrast of moiré patterns for the slanting angles, the leftmost pixel line in vertical direction (the bottom pixel line in horizontal direction) from each slanting angle including  $0^\circ$  are arranged from top to bottom as the angle order for the cases of the grating in Figure 5-3 and the grating with  $O_p = 0.4833$  mm and  $l_w = 0.4028$  mm as shown in Figures 5-4 and 5-5.

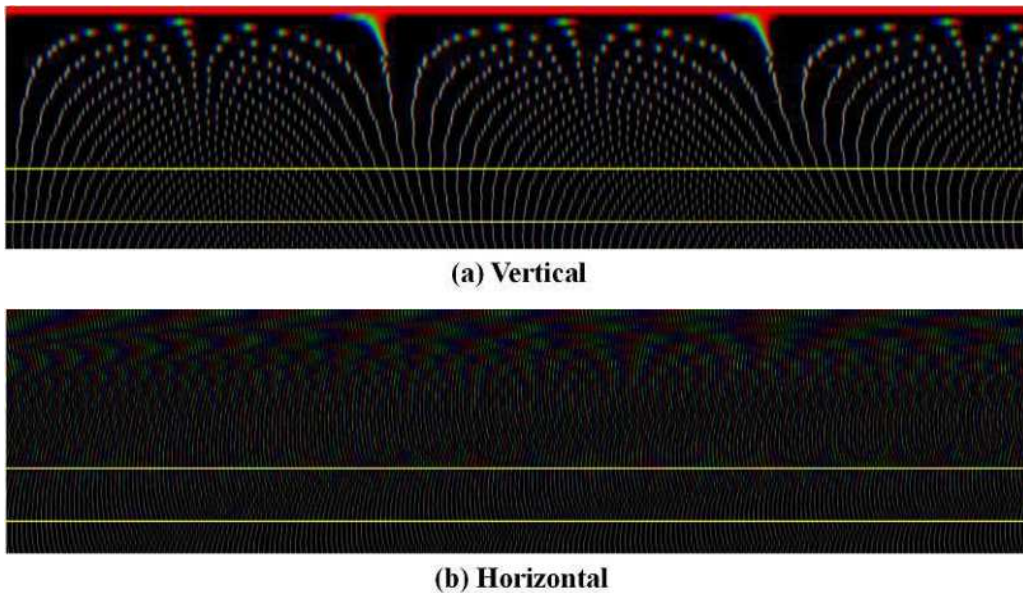


Fig. 5-4. Angular behaviour of colour moirés for the case of a grating with  $O_p = 3.4$  mm and  $l_w = 3.2389$  mm

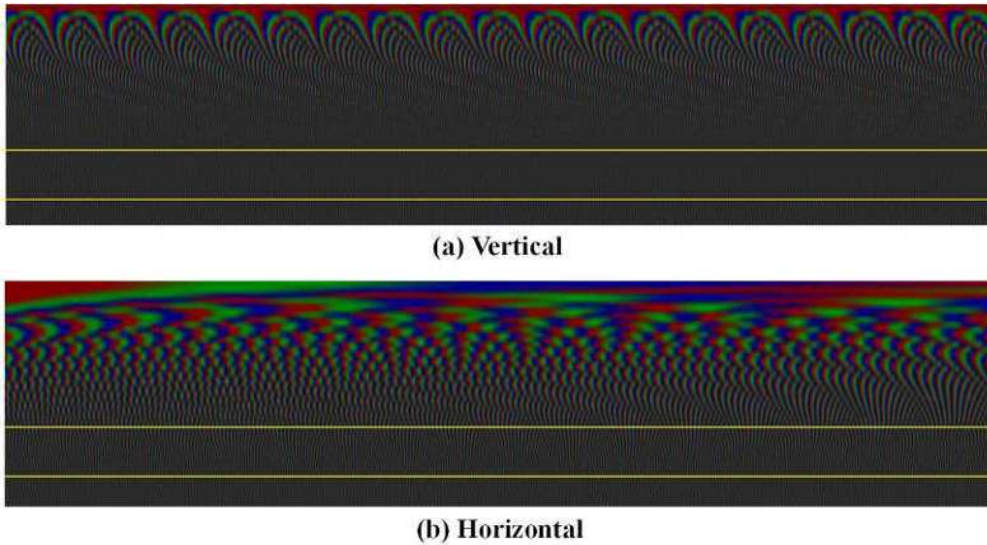


Fig. 5-5. Angular behavior of color moirés for the case of a grating with  $O_p = 0.4833$  mm and  $l_w = 0.4028$  mm

Figures 5-4(a) and 5-5(a) are for the vertical pixel line, and Figures 5-4(b) and 5-5(b) for the horizontal pixel line. Two horizontal lines in each figure represent the angle range  $31^\circ$  to  $40^\circ$ . These Figures show very unique colored line patterns. The color patterns change periodically. Figures 5-4(a) and 5-5(a) show that the patterns are periodic but Figures 5-4(b) and 5-5(b) do not look apparent. However, the patterns are also periodic because the color moiré patterns from the same number pixel lines of different slant angles have the same patterns as those in Figures 5-4(b) and 5-5(b), except their phases. The color patterns in Figures 5-4 and 5-5 can be used to paint images to have a unique color combination as shown in Figure 5-6.



(a) Original image



(b) Color Moiré added image

Fig. 5-6. A Unique color combination image with color moiré. (a) Original image, (b) Color Moiré added image

Figure 5-6(a) shows a word “Rainbow”. The 7 letters are colored red to violet in the letter order. When the 7 letters are combined with the color pattern in Figure 5-5(a), they have unique color patterns as shown in Figure 5-6(b). These color patterns can be hardly obtained with a hologram. Figures 5-4 and 5-5 indicate that the color contrasts are diminishing as the angle increases. However, it is difficult to define the angle for the lowest color contrasts. But the color contrasts look smaller in the angle range  $31^\circ$  to  $40^\circ$  compared with other angle ranges. This is confirmed by Figure 5-7. Figure 5-7 shows the color moiré pattern for both  $l_w = 3.2389$  mm ((a)) and  $l_w = 0.1611$  mm ((b)) when  $O_p = 3.4$  mm. Figure 5-7(a) and (b) represents a parallax barrier and a lenticular, respectively. They show that the color moiré characteristics are not different but color compositions are reversed. They have a conjugate relationship because the sum of two-line widths equals to the line period  $O_p$ . It is clear in Figure 5-7(a) and (b) that the distinction between color points in each color lines diminishes as the angle increases. This means that the color contrast becomes lower as the angle increases, that is, the color contrast is lowest at  $45^\circ$ . But the color contrast for  $45^\circ$  is more than other angles because each color line is colored differently as shown in Figure 5-7 (c). Figure 5-7(c) is the magnified image of Figure 5-7 (a).

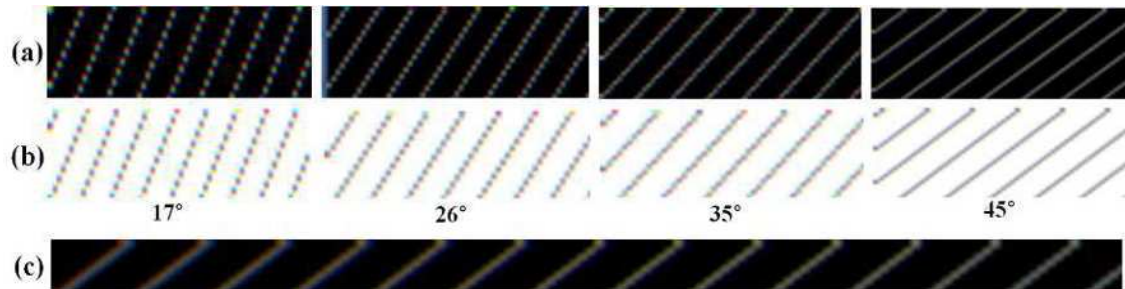


Fig. 5-7. Comparison of Color moiré contrasts of different slanting angles

It clearly shows that each line is differently colored. This means that the color contrast at  $35^\circ$  is visually the lowest. In fact, the color moiré contrasts in the slanting angle range of  $31^\circ$  to  $40^\circ$  are not too different as shown in Figures 5-4 and 5-5. Hence it is necessary to develop a quantitative method of finding the minimization angle in future. The current simulation result does not match with the previous results. The color contrast reduction with the increasing slanting angles is realized because the two edges of each line in the VZFO line pattern can cross RGB sub-pixels which are close to each other. Hence, they will have more chances of being combined as a white or a

gray rather than a single color. The simulation can also be used to simulate the color moirés in 2-D gratings. Since a 2-D grating is considered as two overlapped line gratings, the simulation can be done by overlapping the color moiré pattern of one-line grating to that of another line grating. In this case, one of the color moiré patterns should be rotated to  $180^\circ$  along a horizontal line of the image to reflect line direction of its corresponding line grating. This combined simulation is displayed on the panel with the two overlapped line gratings of  $O_p = 0.4833$  mm, and  $l_w = 0.4028$  mm and  $0.3222$  mm with the crossing angle of  $10^\circ$ , i.e.,  $\pm 5^\circ$  along a vertical line. Figure 8 shows the result. No difference between two color moiré patterns from the simulation and the crossed line gratings, except fringe distortion due to uneven overlapping of two gratings and color position shifting due to extra thickness originated from the top grating at near the right side.

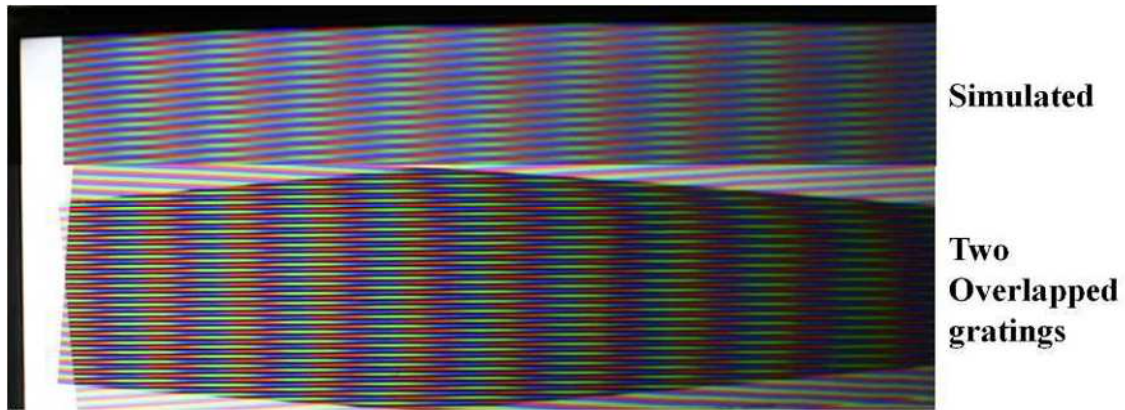


Fig. 5-8. Comparison of the color moirés from a 2-D grating and the simulation

## 5.5 Conclusion

Color moirés appearing at IP-type 3-D displays are induced from the periodic blocking of the pixel pattern in the panel by the equivalent line pattern of the VZFO. This concept was proved by the simulation algorithm because it is accurately predicting the color moirés from any combination of VZFO line and pixel patterns, and can help to find the ways of minimizing the color moirés in 3-D displays. The simulation results inform that the angles used before to minimize the color moirés are different from the angle which is considered as minimizing the color moiré contrast in this paper. It is considered that the color moiré patterns can be used to in anti-counterfeiting areas because they have almost the same properties as the current hologram. It can generate tremendous number of different moving color patterns.

## **6. Holographic and light field imaging as future 3D displays**

### **6.1 Introduction**

3-D imaging has been developed to bring the image that we perceive from our living space to home with as small as possible alterations and considered as the main imaging technology of future. The 3-D imaging methods developed before late 1980th are stereoscopic imaging for theatrical use, volumetric imaging for special purposes and holographic imaging for art and metrological applications. The 3-D imaging methods developed since late 1980th are mainly for home use and they are mostly realized on a flat panel display from mid-1990th [6-1], [6-2]. The advantage of using the flat panel displays is that the 3-D image can be displayed together with the plane image which is a reference plane image of a 3-D image. Hence 2-D/3-D compatible displays based on a flat panel displays, and electro-holography based on a digital display chip such as SLM, DMD and LCD are currently the major research subjects in 3-D imaging. Some of the methods have almost been matured technically, but they are still staggering in the market. The stereoscopic TV based on polarization and shutter glasses, and mobile phones based on parallax barrier are in market, and the TV had already been televised [6-3], [6-5]. But the decreasing interests on the TV make them to be an extra imaging function of the flat panel displays for plane images, and the Multiview 3-D displays could not even have a chance to be in mass production lines. Many reasons could be found for this reality but the unnatural viewing condition such as restrictions in viewing position changes, inconveniencies of wearing the glasses, unnatural depth sense and distorted images accompanied with viewers viewing position changes [6-6], [6-7] will be the major reasons for the stereoscopic TV and the inferior image quality compared with the plane image for the Multiview. In fact, the continuously increasing panel size, higher resolution, brighter and more uniform brightness distribution in flat panel displays have been continuously improving the qualities of plane images and strengthening the psychologically induced depth sense in the images. The quality of the 3-D images has also been improved by the flat panel displays but the improvement speed is much lower than that of the plane images. This speed difference makes the relative image quality of the 3-D images much worse than that of the plane images. But this is not only reason why the 3-D imaging is still suffering in finding a way to stand alone in the market, even with the number of 3-D imaging methods with the matured technologies. The more

plausible reason is that the 3-D imaging has not utilized its only merit over the plane image, the depth sense fully. The current 3-D imaging can only provide virtual depth sense which can cause discomfort and eye fatigue induced by Vergence-Accommodation(V-A) conflict [6-8], except holographic and light field imaging. The 3-D imaging should provide depth sense conforming to the natural viewing condition. This is what the holographic and the light field displays are aimed for. The natural viewing condition can also be achieved with the stereoscopic imaging method wearing the polarization glasses by making two pinholes of a close distance covered with different color filters on each eye side polarizer [6-9]. But the presences of the eyeglasses and color filters will be a problem for the method. The holographic imaging is a concise name of electro-holographic imaging which uses a digital display chip to display a hologram. The imaging has been known as the most complete 3-D imaging method devised by mankind [6-10]. It can create a reconstructed image with a spatial position and real entity. The imaging can provide images conforming to a natural viewing condition. But with the currently available digital display chips, the holographic imaging cannot demonstrate its actual capability. On the contrary, the light field display is one of Multiview displays, that can provide a continuous parallax and very wide focusable depth range but its name has been very confusingly used so far. This makes difficult to imagine what actually the light field meant. In fact, the light fields formed by visible light rays of various wavelengths from objects and scenes in our environments enable human to view and recognize them. The lights from a display also form light fields in its front space. Hence any display can be named as light field display. However, the word “Light Field” was used to express the light rays in different spatial positions [6-11]. And it was adopted in computer graphics for the purpose of representing the rendering process involved with the light rays [12], since then it has been consistently used in the computer graphics to represent the process. But in the 3-D imaging, the “light field display” was used to name several types 3-D displays such as utilizing 1) a 360° rotating imager [6-13], [6-14], 2) Multiview images [6-15] and 3) typical IP [6-16]-[6-18]. The name “light field display” is also used by Holografica for its 3-D displays [6-19], [6-20]. But in this review, the light field display will be used as another name of the super multiview display [6-21]. The light field and electro-holographic imaging are considered as very promising 3-D imaging methods in future. The promising in them is mostly coming from their abilities to provide a continuous parallax which is a core requirement of fulfilling the natural viewing condition, and a large focusable image depth that is at least exceeding the focusable depth range allowed by the depth of field (DOF) of viewers’ eyes when viewing a stereoscopic image. This large depth guarantees no eye fatigue by V-A conflict.

In this review, the parameters defining the image quality of 3-D imaging are defined, and the development histories of the holographic and light field images are described along with the brief history of other 3-D images. The characteristics of two imaging are compared in detail and future perspective of the two imaging is also described.

## **6.2 Parameters defining the quality of 3-D images**

In the 3-D imaging, the parameters of estimating the image quality will be 1) the focusable image depth range causing no eye fatigue, 2) smoothness in parallax changes, 3) the viewing zone angle range with no image distortion and brightness decrease, 4) the range of viewing zone in depth direction, 5) image clearness and sharpness, 6) various image distortions and crosstalk in both transversal and depth directions, 7) the image resolution in both transversal and depth directions, and 8) image brightness. The quality will be better if these parameter values are higher, except the distortions and crosstalk. They should be kept as small as possible for the quality point of view. The parameters, except 1), 2) and 7) are also applicable to plane images and their values for 3-D images should be comparable to those of the plane images, though the depth resolution is applicable only to the 3-D images. But none of the currently developed 3-D imaging can provide parameter values comparable to those of the plane images and satisfactory to their own requirements. Among the above parameters, the focusable image depth range is defined as the depth of field of viewers' eyes, i.e., the depth range between front and rear spaces of the display panel/screen, where viewers can accommodate and verge their eyes without losing image clearness [6-22]. It is known that when diopter  $D$  is defined as  $1/r$ , where  $r$  is the viewing distance from the image panel/screen, expressed in meter unit [6-23], the DOF is approximately given as  $D \pm 0.3D$  for the stereoscopic images [6-24]. So, the floating images within DOF can be viewed without the V-A conflict. Hence the focusable depth range should be extended more than the distance range specified by  $r/1.3 \sim r/0.7$  as illustrated in Fig. 6-1. Fig. 6-1 is a geometrical presentation of the focusable depth range. The depth range can be extended to the point at which the distance from viewers is enough to make them to fuse the images from the display panel/screen. The extended focusable image depth range is specified as SM (super-multiview) zone as in Fig. 6-1. The extension is achieved by projecting at least two different view images at the same time to the pupil of a viewer's each eye. In the holographic images, the reconstructed image has a real spatial position and a certain volume. Hence the focusable image depth range can be extended to the distance set by the available display space. If this range increases more and more, the eye fatigue induced by the VA conflict will be reduced further. The smoothness in parallax changes implies that the 3-D image should provide as many as possible different view

images to a viewer's each eye at a same time in corresponding to the natural viewing condition. The natural viewing allows the viewer's each eye to get a continuous parallax, i.e., almost infinite number of different view images at a same time. The holographic image can probably provide enough number of different view images to meet the condition but for other 3-D images, the condition can be hardly realized because in practice it is impossible to display an infinite number of different view images through the display panel. It is not known that how many different view images are projected to the pupil of a viewer's each eye in the light field images claimed so far [6-25]-[6-27], but four images are at most [6-28].

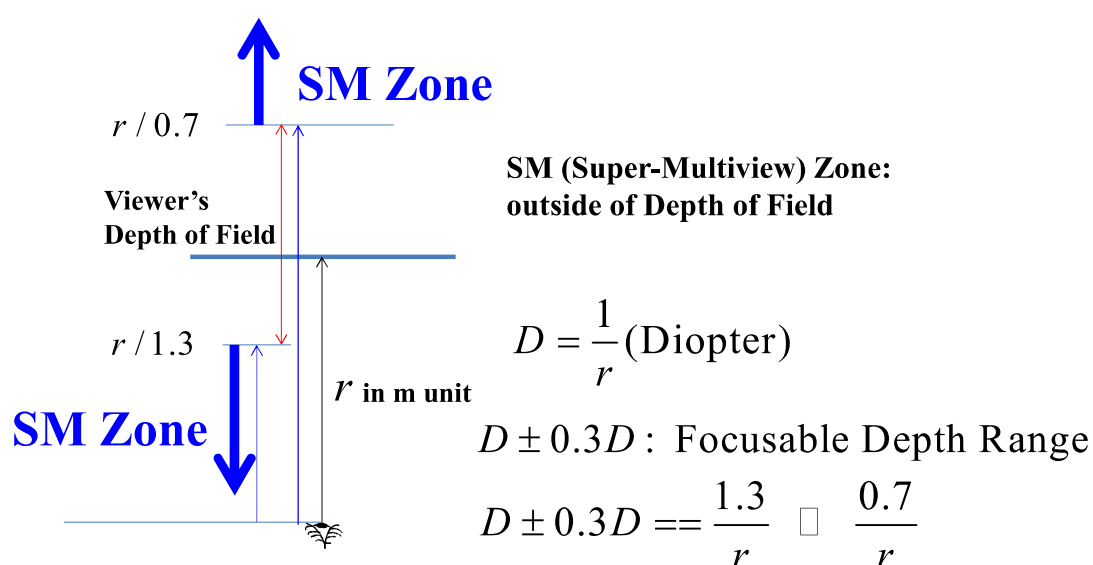


Fig. 6-1. Graphical illustration of DOF and SM zone

The continuous parallax is what makes the light field images comparable to the holographic images and different from the current Multiview images. The viewing zone angle range defines the angle range that allows viewers whom are standing in front of the display panel to move around to perceive 3-D images from the image on a display panel/screen. This angle is related to the field of view (FOV) of the VZFO (Viewing zone forming optics such as parallax barrier/lenticular/microlens array plate used in Multiview imaging) [6-29]-[6-31] and different from viewing angle which is related to the panel/screen size [6-32]. It is within the angle range  $0^\circ \sim 180^\circ$ . It should close to  $180^\circ$  to cover almost entire front space of the display panel/screen as the flat panel display, for an ideal

3-D display. However, the range will be hardly attained with 3-D images because the depth range is achieved by sacrificing the angle. In the electro-holography based on the SLMs or DMDs [6-33]-[6-35], the angle can be less than 30° even with the SLM of having 1µm pixel size. The range of viewing zone in depth direction defines that of viewing distances range within the viewing zone. This range is not well defined in Multiview 3-D images but defined clearly in holographic images. The image resolutions of 3-D images in transversal direction are worse than the plane image because 3-D images share pixels for different view images. For the holographic images the resolution is much worse due to the presence of astigmatism. The astigmatism also deteriorates the depth resolution which is unique for the 3-D images. The resolution depends on the pixel size and camera distance in a camera array for the multiview images in the Multiview displays [6-36]. The other parameters are related with the presence of the continuous parallax, and pixel size and resolution. As the size decreases and resolution increases, the parameter values will be increased.

### **6.3 History of 3D imaging: From stereo imaging to light field displays**

The principle of achieving depth sense with a stereo image pair was known before the 18 centuries [6-37]. This principle was actualized as a stereoscope [6-38] in Mid-19 century. Since then several stereoscopic imaging methods based on special eyeglasses such as anaglyph, polarization, gray level difference, i.e., Pulfrich effect [6-39] and interlaced on-off shutter [6-40], and those based on VZFO such as parallax barrier [6-41] and lenticular plates had been introduced [6-42]. Along with these stereoscopic imaging methods, holographic and volumetric imaging methods had also been developed from 1960th [6-43], [6-44]. The volumetric imaging methods allow displaying 3-D images with a real volume but they needed either a translating or /rotating screen/panel, or an imaging chamber or a layered screens/panels to create their image spaces where images can be displayed. The image spaces require a physical volume filled with a special gas [6-45] or other phase materials [6-46], with a moving mechanism of an active or a passive screen [6-47], [6-48], or with layered functional plates [6-49]. The difficulties of creating the image spaces are the bottleneck of further progresses in this imaging. The eyeglasses based stereoscopic imaging methods are still popular but they are not too friendly to viewers because they induce fatigues to the viewers' eyes and other problems mentioned before. While the VZFO based stereoscopic images has been applied to mobile phones and there is a mobile phone equipped with a stereo camera [6-50], [6-51] but they impose a strong restriction on the viewers' eye positions. To ease the problems in stereoscopic images, Multiview and electro-holographic imaging methods had been developed from late 1980th [6-52]-[6-54]. The

Multiview imaging methods allow viewers' viewing position changes without wearing special glasses and minimizing the image distortions accompanied with the changes by providing both binocular and motion parallaxes together to viewers. The methods were realized in many different ways [6-1], but currently the contact-type which has the structure of a flat display panel layered with one of the VZFOs mentioned above or a 2-D microlens array which was introduced in early 20 century [6-55], on the top of the panel as shown in Fig. 6-2 is the main stream. Fig. 6-2 shows the panel structure of the contact-type 3-D displays when a lenticular or microlens array is used as the VZFO. The VZFO has a finite thickness. Its thickness comprises the glass plate to protect the liquid crystal layer. The contact-type multiview imaging methods utilizing parallax barrier or lenticular plate as the VZFO and a multiview camera array as the source of the multiview images were named as Multiview (MV), and when the microlens array is used both as the VZFO and the source of multiview images with an image detector its under were named as Integral Photography (IP) [6-55]. The microlens array combined with the image detector has been developed as a plenoptic camera [6-56]-[6-58]. And also, the differences between MV and IP had been diminished because the lenticular plate was also used as the VZFO in IP under the name of 1-D IP [6-59].

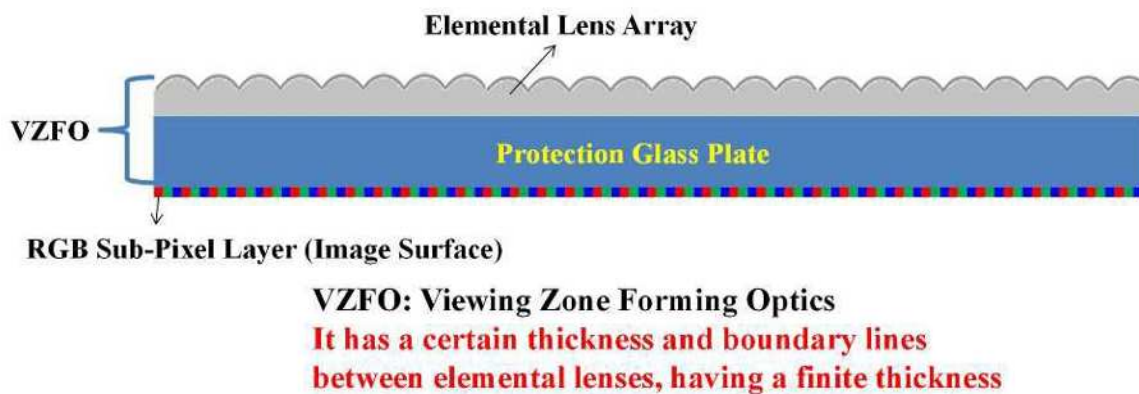
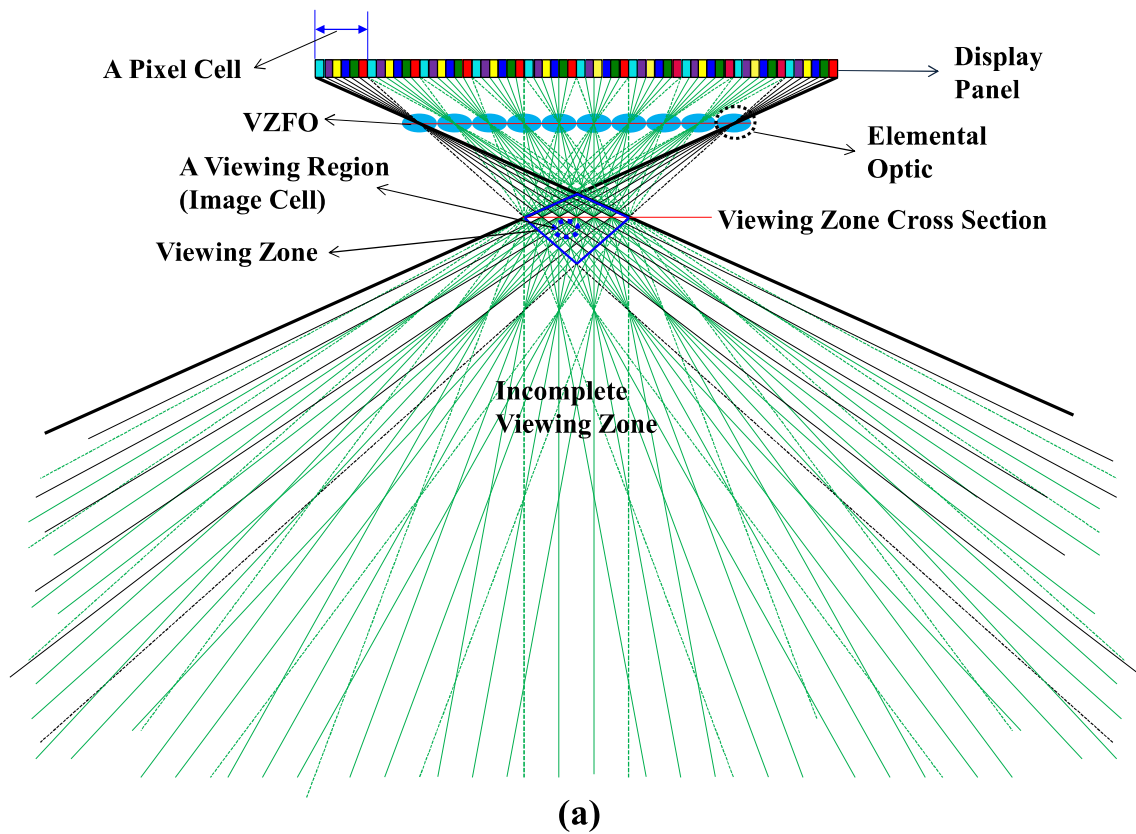


Fig. 6-2: Typical structure of contact-type Multiview 3-D displays

However, there are still differences between them because their optical configurations and image compositions on the display panel [6-60] are different. The MV has a radial configuration and the IP a parallel. This configuration difference is originated from the relative size of a pixel cell (elemental image), which is the basic image unit of MV (IP) [6-61], to that of an elemental optic which consists of the VZFO. In the MV (IP), the sizes of pixel cell

(elemental image) in both horizontal and vertical directions are slightly bigger than (the same as) those of the elemental optic as shown in Fig. 6-3. Fig. 6-3 compares the optical geometries for forming viewing zones in MV (Fig. 6-3(a)) and IP (Fig. 6-3(b)). Each pixel cell (Elemental Image) is consisted of 6 pixels (8 pixels) and projected to its front space by its front elemental optics to form viewing zones. When considering a pixel cell (Elemental Image) and its front elemental optic, they work like a projector. Hence the projectors are radially aligned in MV and in parallel in IP to form the viewing zone. The viewing zone is defined as the space where the magnified images of all pixel cells (elemental images) are crossing together. The boundary of this view zone is defined by the crossing between the left (top) and right (bottom) most pixel cells (elemental images). The viewing zone in MV is given as the diamond shape space near the center of the geometry, but that in IP the pyramidal shape space in the bottom of the geometry.



(a)

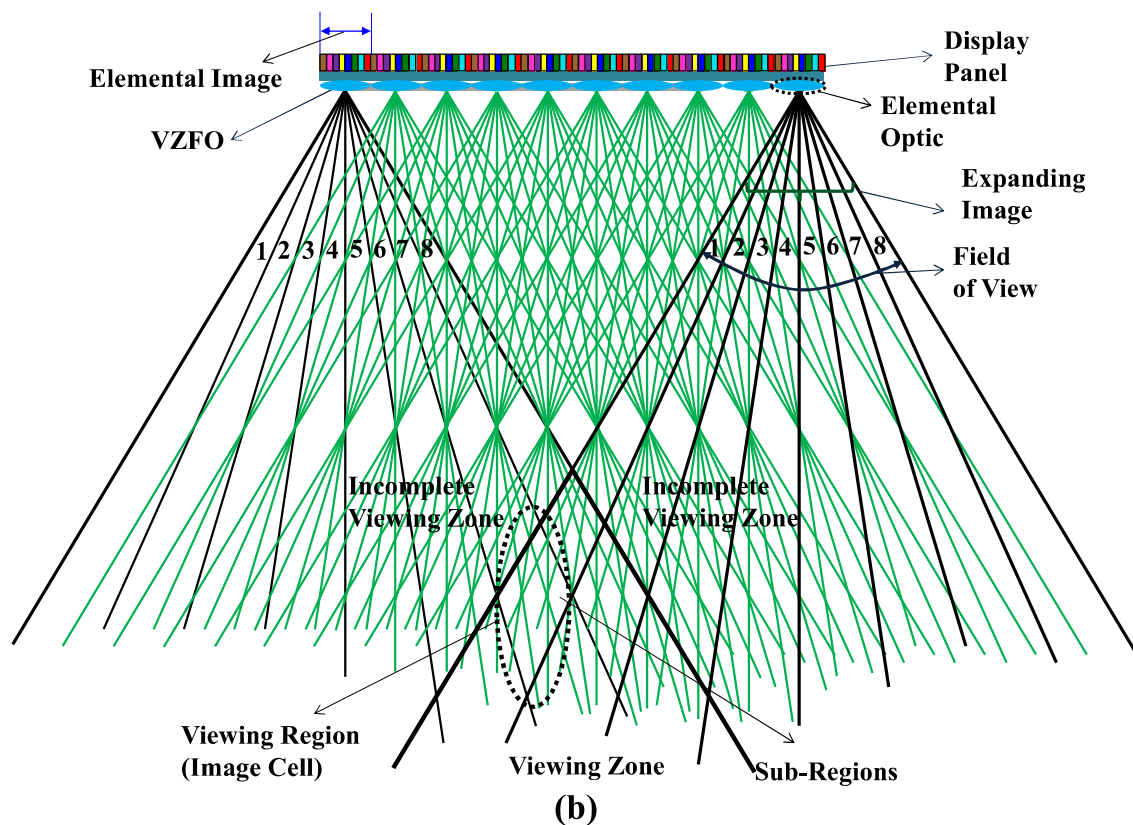


Fig. 6-3: Viewing zone forming geometries of contact-type Multiview 3-D displays having (a) Radial (MV) and (b) Parallel configurations

The viewing zone of IP will appear much longer distance from the panel as the number of elemental images increases and its internal pattern matches completely to the upper part of MV's viewing zone when the viewing zone is divided into two by the line representing the viewing zone cross section (VZFO) [6-62]. The incomplete viewing zones are the places where a part of pixel cells (elemental images) are viewed. When the chief rays from each pixel cell (elemental image) are considered as shown in Fig. 6-3, it is possible to assume that the pixel cell (elemental image) is focused at the center of each elemental optic and starts to expand from the focused point. It is possible to represent the viewing zone forming geometry of MV and IP by an array of point images corresponding to the array of the pixel cells (elemental images). Each point image is located at the center of each elemental optic in the VZFO. However, the optical configuration difference is not the main feature of discriminating the MV and IP because IP has also adopted the radial optical configuration [6-63] due to the

difficulties of forming the viewing zone corresponding to the optimum viewing distance in IP. In fact, since the difference between the pixel cell and the elemental optic is just a few microns [6-64], the optical configuration difference between MV and IP is also not very prominent. Hence the remained difference between them is the image compositions in the pixel cell and the elemental image. The image composition of an elemental image is the inverted image of a view image viewed at the position of an elemental optic in VZFO. And that of a pixel cell is the same position pixel from each of the multiview images aligned to the inverted order of the cameras in the multiview camera array that generates the multiview images. The display panels for MV and IP are composed of pixel cells in the order of pixels in a view image and of elemental images in the order of the elemental optics in the VZFO, respectively [6-65]. As indicated before, the multiview 3-D imaging methods improved some problems involved with the stereoscopic imaging, but the presence of the VZFO introduced other problems such as reduced brightness, reduced resolution for each view image and annoyances in viewing. Added on these, they are not free from eye fatigues and the image jump caused by inappropriate parallax changes between multiview images incurred by the finite number of different view images, when viewers change their viewing positions. To resolve these problems, active parallax barrier [6-66] 6lenticular [67], LCD lens array [6-68] and electro-wet lens array [6-69] are introduced, instead of improving the quality of the VZFO, a method of eliminating the VZFO with use of a point light source array had also been introduced [6-70]. The problem of the point light source array method is that the output aperture of each light source should be smaller than the basic resolution elemental in a display panel, i.e., pixel or sub-pixel to insure the full use of the panel's pixel resource. With the improvements in VZFO, the Multiview imaging methods are further developed as a super-multiview imaging [6-71]. The basic idea of the super-multiview is projecting at least two different view images at the same time to viewers' each eye through different pupil positions without overlapping as shown in Fig. 6-4. Figure 6-4 shows the concept of the super-multiview imaging.

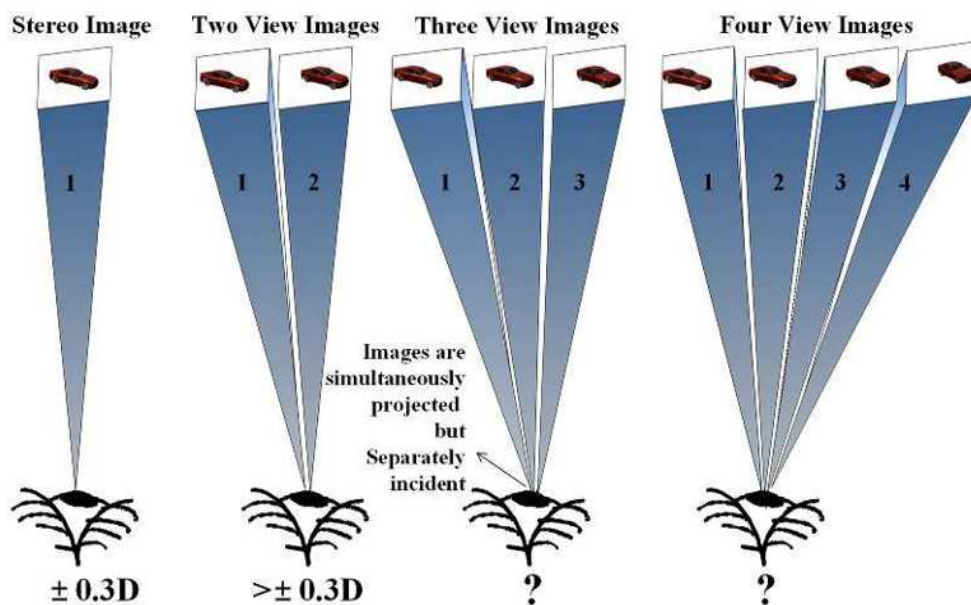


Fig. 6-4: The concept of super Multiview imaging

For the stereoscopic imaging, only a view image is projected to each eye but the super-multiview imaging 2, 3, 4 and more view images will be projected to each eye. This idea is to simulate the natural viewing condition to achieve a continuous parallax. This condition represents a typical phenomenon appearing at the input aperture of an imaging device such as a camera, microscope or a binocular since every point of the input aperture of the device consists of a view image formed by a ray from each point of an object/a scene. Hence there are an infinite number of different view images at the aperture. So, does the pupil of viewers' each eye. The continuous parallax is induced by these infinite numbers of different view images and it can possibly induce a monocular depth sense too [6-72]. This means that accommodation is also obtained with the continuous parallax. The super-multiview concept was introduced in mid-1990th with a display named focused light array (FLA) [6-73]. The equivalent optical configuration and image composition of FLA is in principle the same as 1-D IP and MV, respectively. Each of the pixel cells composing a frame of an image is made as a focused image and then the image points are displayed on a directional diffusive screen by the scanning action of an x-y scanner. The FLA introduced 45 different view images in horizontal direction but no evidence was found that FLA provides a continuous parallax within its viewing region [6-74]. Following the FLA, a display named as Hologvizio was introduced [6-75]. This display hired an array of projectors aligned as the IP's elemental image array at the VZFO. Hence the image from

a projector is shifted a certain distance corresponding to the period of projectors in the array from its adjacent projectors' images. It claims that the display can provide a continuous parallax. However, the basic principle of this display is just the same as the IP. The compositions of the perceived image from Hologvizio will be very similar to that from FLA. This display was followed by a display named as multiple images display (MID) which displays more than 200 different view images was introduced [6-27]. The equivalent optical configuration and image composition of MID are not different from those of FLA, except the number of different view images and their multiplexing schemes. The multiview images in MID are presented based on a spatial-multiplexing scheme but the FLA a time-multiplexing scheme. The images in MID are horizontally aligned and each of them is collimated then projected radially to a diffusive plate. All images have the same size as the diffusive plate and are aligned such that the center of each image is matched to that of the plate with the same angle distance from its adjacent images. In this way, it can be considered that the same position pixels in the images will be overlapped together at the diffuser plate. Hence the composition of the overlapped pixels is the same as that of a pixel in the FLA. MID claimed that it can extend the depth of field to the SM zone as shown in Fig. 6-1 [6-76]. However, whether MID conforms to a super-multiview concept or not has not been verified because it was not known that how many different view images are getting into the pupil of viewers' each eye simultaneously. In Fig. 6-5, the image projection geometries of Hologvizio, and FLA and MID are compared. In the FLA and MID, the multiview images are collimated and projected on the diffuser screen with a small angle difference as shown in Fig. 6-5(a), A 2-D array of point images are formed at the screen by the matching pixels from different images. The 2-D array of point images formed at the screen have the same number pixels and each point image expands in parallel with the same expanding angle. In Hologvizio, the images are projected without collimation by shifting one after another for a small distance in horizontal direction as shown in Fig. 6-5(b). The images are also forming a 2-D array of point images on the screen by overlapping pixels from different images as in Fig. 6-5(a). The number of pixels in a point image reduces as goes to the both edge sides, and the expanding angles of the point images are not the same and their propagation directions are also different. The projection geometry difference between them induces just small differences as described above. The FLA, MID and Hologvizio are having the same image projection geometry as the 1-D IP but pixel composition of each point image is the same as the pixel cell in MV.

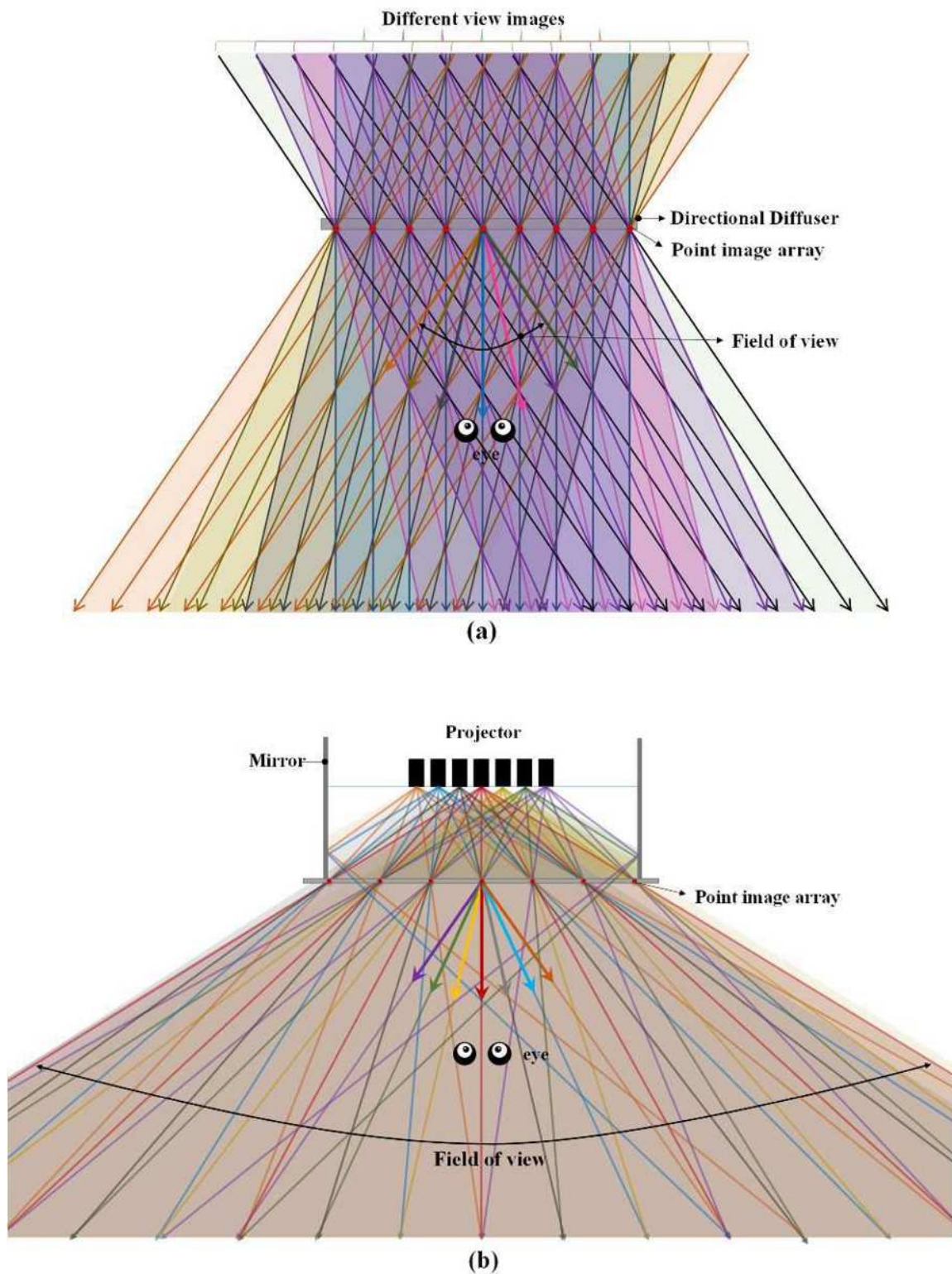


Fig. 6-5: The image projection geometries of (a) FLA and MID, and (b) Hologvizio

The IP image projection geometry is found only in the 2-D stereo-hologram such as Zebra hologram [6-77]. The image recorded on the 2-D stereo-hologram is a 2-D multiview image array. When a reconstruction light illuminates the hologram, the 2-D point hologram array turns to a 2-D point image array as in IP. The hologram has the same multiview image arrangement and image cell structure as those of IP, though the number of image points and the resolution of each image point of the hologram are much more than those of IP, and the number and size of the image cell are more and smaller, respectively, than those in the IP. This is why the hologram has not been displayed on a flat panel display so far. But the reconstructed image from this hologram will be the best subject of testing the presence of a continuous parallax and focusable depth range extension. But no result in this direction has been reported with the hologram.

In the continuous parallax point of view, the super-multiview and the holographic images will not be different, because the natural viewing condition is considered as an inherent property of a hologram. The hologram is recorded at the input aperture plane of a camera's objective, it contains an infinite number of different view images. Hence the hologram is considered as providing the continuous parallax but it is difficult to verify the presence in the current electro-holography based on a digital display chip due to its small viewing zone angle. The idea of electro-holography, i.e., displaying hologram on a display device came around year 1965 by a group of researchers from AT&T Bell lab. [6-78]. However, this idea could not be realized due to the lack of a display media for a hologram. This idea was revived under the name of holographic video in Mid-1980th with use of an AOM (Acousto-Optic Modulator) made from TeO<sub>2</sub> [6-79]. The holographic video had been continued to the end of 1990th [6-80]-[6-82] but it was eventually stopped due to difficulties in finding a better AOM to display a hologram for bigger and more resolved reconstructed images with wider viewing zone angle, and in aligning moving components to stop image flowing. The high cost of achieving a frame of hologram and incompatibility to a flat panel display were not free from the stopping. In this period, a new method of displaying a hologram on LCDs was also developed [6-83], though it was hard to view the reconstructed image because of the LCD's large pixel size that exceeds more than 30  $\mu\text{m}$ . This LCD based electro-holography paved the load to the current electro-holography based on digital display chips mentioned before. However, the electro-holography has many problems incurred by the chip's small size to display hologram, astigmatism involved with the reconstructed image [6-84] and small viewing zone angle caused by a large pixel size [6-85] along with the diffraction effect induced by the digital pixel structure of the chips. But these will be the solvable problems in future because there

already introduced a display chip with 1  $\mu\text{m}$  pixel size [6-86]. In the digital projection chips, the number of different view images to be recorded on the chip is smaller than those on a photographic plate/film. Since each pixel can record a view image, each chip can record different view images corresponding to its pixel resolution. However, since each pixel has only a recording layer, the number of recordable object points on the pixel will be much less than those on the emulsion layer in photographic plate/film, which has a finite thickness [6-87]. Hence for the continuous parallax, the pixel size and resolution need to be as small and high as possible, respectively, and the pixel should have a multilayer structure to record phase information.

#### **6.4 The condition to be a light field display: The transition from integral photography to light field display**

Our living space is filled with electromagnetic waves of various wavelengths from nature and man-made radiation sources. We are living within the electromagnetic field formed by the waves. The visible light is a part of the waves that allows us to see our surrounding space through the light field formed by the waves. In the displays, the visible lights from a display panel/screen forms a light field in its front space. A viewer who watches a display panel at a certain location of the front space can only perceive the lights forming the light field at the position. This is shown in Fig. 6-6. Fig. 6-6 compares the light fields formed in front space of a display panel for a plane image in MV and IP. The fields are shown for 7 distances of 100 mm, 150 mm, 250 mm, 330 mm, 450 mm, 500 mm and 750 mm from the panel when different color strips are displayed on the panel as the different view images. For the MV (IP), a pixel cell (elemental image) consists of red, green, blue and yellow strips, and for the plane image, two color combinations such as the same color arrangement as MV and blue-green strips as shown in Fig. 6-6 are displayed.

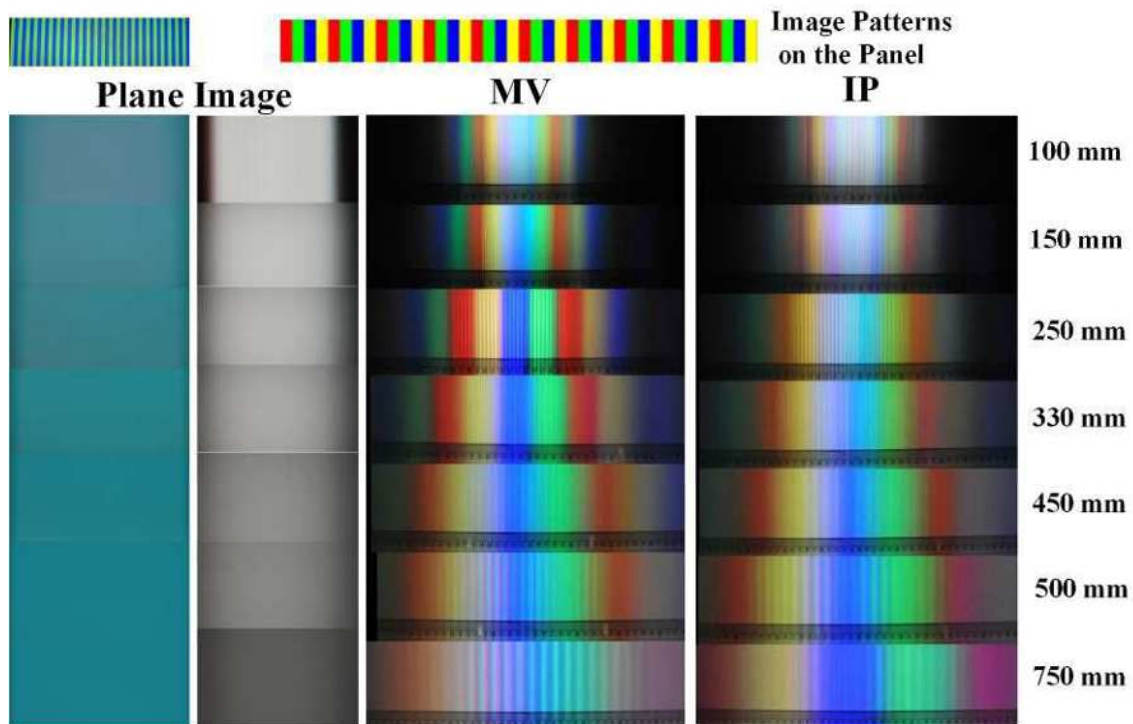


Fig. 6-6. Light fields formed in front space of a display panel for plane image, MV and IP geometries

The images are those on a diffuser plate located at each distance specified above. For the plane images, the green and blue (R, G, B and yellow) strips on the panel are diffused together and the light field has already turned to a cyan color (white) at 100 mm from the panel. It is well known that the mixings of green and blue, and R, G, B primary colors create cyan and white colors, respectively. But the presence of yellow in R, G, B and yellow strips is not noticed. The light field does not change its color with different distances and directions, except its brightness. The brightness reduces as the distance increases. Viewers' two eyes will get the same color, i.e., the same scene. This means that no depth sense will be perceived with the plane image. For the MV and IP, the R, G, B and yellow strips in each pixel cell (elemental image) is expanded radially (in parallel) as shown in Fig. 6-3 by the elemental optics in VZFO while keeping their colors and relative positions to other color strips, and mixed with the expanding color strips from other pixel cells (elemental images). The mixing informs that different view images will be mixed [6-88]. In IP, the mixed color strips will be separated again and the same color strips from different pixel cells (elemental images) will be overlapped to each other as the distance increases. This separation occurs

when a color strip in each pixel cell (elemental image) is expanded more than the horizontal size of the image on the panel. The images at 450 mm, 500 mm and 750 mm shows that the area of each color strip increases as the distance increases. This indicates that the same color strips from different elemental images are overlapped more and more. The image at 750 mm shows that the red, green, blue and yellow color strips from left to right appear almost continuously and they are repeating to show the presence of side viewing zones. This is because each elemental image is not even projected by its immediate front elemental optic but also by adjacent elemental optics to the front [6-89]. For the MV, the color strips from different pixel cells are mixed but they separated again that the clear overlapping of the same color strips from different pixel cells appears at 250 mm due to its radial projection arrangement. After the separation, they are mixed more and more as the distance increases. The color orders are the same as the image at 750 mm in IP, and they are repeating as mentioned above. The color strips from different pixel cells are mixed again as the distance increases. The same color overlapping is also shown in the images at 150 mm to 330 mm though they show color mixings at the boundaries of different color strips. Hence this range can be considered as the viewing space where different view images are separately viewed. This range corresponds to a diamond shaped white regions along the line indicating the VZFO and their vicinities in Fig. 6-3 (a). In this range, the light field is divided into the number of different view images on the panel and each divided light field is formed by the lights mostly coming from a view image converged to the light field location. Other than the range within the viewing zone, the light fields are formed by mixing between the lights coming from pixels of different view images. The light field images of MV and IP inform that if each color represents a view image, each image will be separately projected to the corresponding eye if the width of each color sector does not exceed a viewer's interocular distance. When it is assumed that a viewer locates his/her left eye at the green and right eye at the red color light fields, the left and right eyes see only green and red strips, respectively, in all pixel cells (elemental images) in the panel. This is the typical way of perceiving depth sense in the 3-D imaging methods having the parallax as their main depth cue. Viewers need to accommodate their eyes within the focusable depth range surrounding the panel to see more clearly the image corresponding to each eye. This is why the perceived image has a virtual depth. If the width is smaller than a pupil diameter of the viewer's an eye, more than two different view images can get into the viewer's each eye simultaneously without overlapping. The separation between different color strips is represented by each smaller viewing space specified as viewing region within the viewing zone in Fig. 6-3. This smaller viewing space is form by the crossings between pixels of

composing the left and right most pixel cells/elemental images. The number of the smaller viewing spaces in the viewing zone is equal to the square of the different view images on the panel for MV and to the number of pixels within the elemental image plus a half of the number obtained by squaring the pixels within an elemental image for IP [6-90]. The pixel composition of the light field at each of smaller viewing spaces is one pixel or one sub-pixel shift from that of its adjacent light fields. So, the pixel composition is an image unit that the viewers will perceive. Hence each of the smaller viewing spaces is named as an image cell for its pixel/sub-pixel composition representing a view image [6-91]. If the size of each image cell in horizontal direction is smaller than the pupil size of a viewer, more than two image cells can be gotten into the viewer's eyes, i.e., more than two different images with the minimal disparity between them. In that case, he/she will perceive a continuous parallax. This is the claims laid by MID, FLA and Holovizio. However to make two image cells to get into the pupil, the pixel size  $p$  of the display panel should be less than  $5 \mu\text{m}$  for the case when the viewing distance  $d$ , focal length of the elemental optics,  $f$  and the pupil diameter of viewer's eye is 1,000 mm, 3 mm and 3 mm, respectively, by the relationship  $pd/f \leq (3.0/2)$  mm. This relationship is obtained by considering that the panel is at the focal plane of VZFO as in typical contact-type 3-D displays [6-92]. As the panel size increases and the viewing distance will also be moved away from the panel. This means that the pixel size should be smaller than  $5 \mu\text{m}$ . If it also requires more than two different view images to get into the pupil, the pixel size should be much smaller than  $5 \mu\text{m}$ . Figures 6-3 and 6-5 also informs that the super-multiview imaging can be realized more easily in MV than in IP, because the sizes of the image cells are much smaller in MV than in IP due to the converging action of the radial configuration. The display conforming to the super-multiview concept is named as the super-multiview display [6-93], i.e., the light field display.

### **6.5 The difference in light field characteristics between Holographic and light field images**

The light fields from a holographic display are different from those in IP and MV as shown in Fig. 6-7. Figure 6-7 shows the light fields from an on-axis hologram on a DMD with pixel resolution of 1280 X 800 and pixel size of  $7.637 \mu\text{m}$  [6-94], along the propagation direction of the reconstructed image, when a collimated laser beam is normally illuminates the hologram. The hologram is a CGH (Computer Generated Hologram) [6-95]. The light field images are for six points objects aligned in a horizontal direction. The points are located at 500 mm from the hologram. The number in each image represents the distance from the hologram in mm unit.

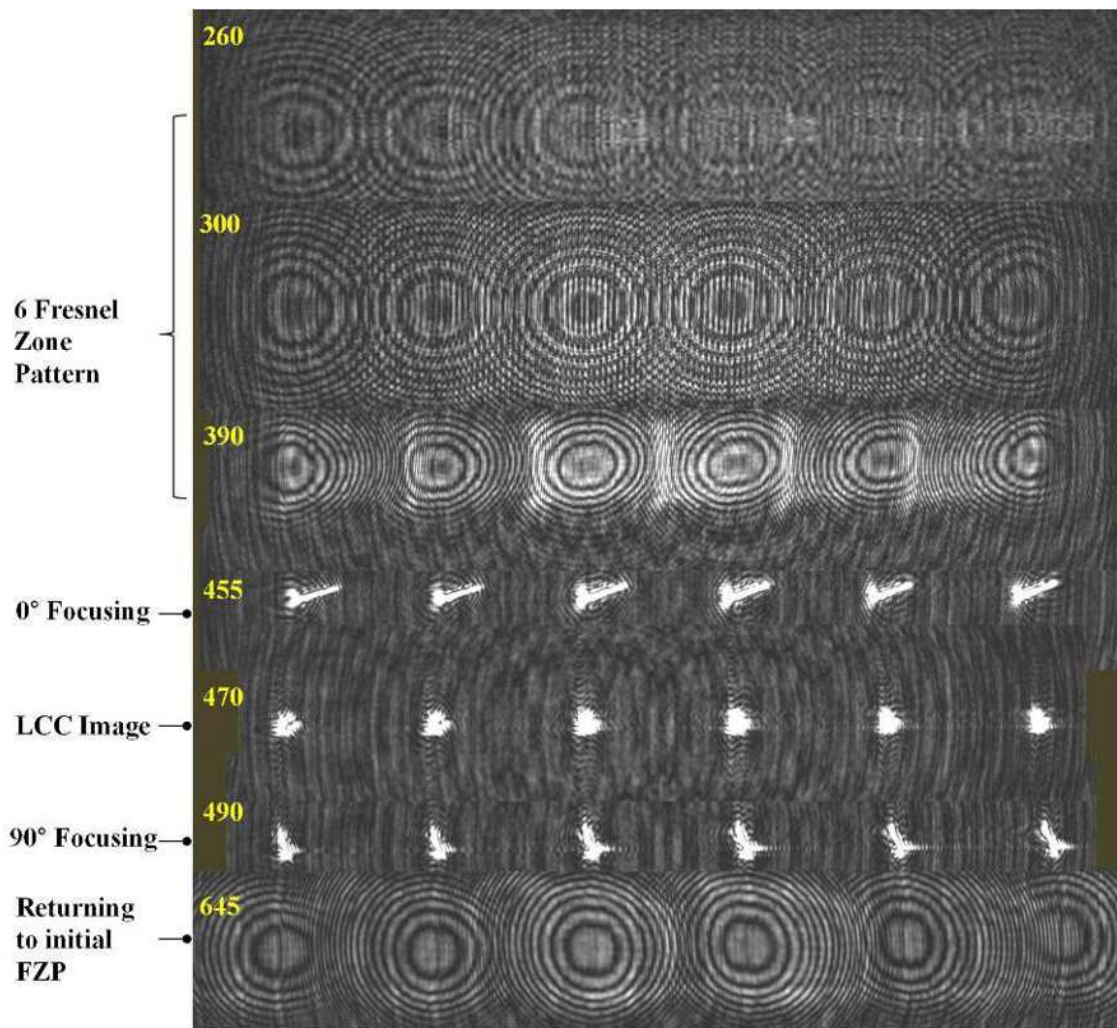


Fig. 6-7: Light fields formed in front space of a DMD for a holographic imaging

The images show the process of forming the reconstructed image: The hologram reconstructs 6 FZPs corresponding to the six points when it was illuminated by the reconstruction beam. Each of these FZPs is independently converged to form a focused image of its corresponding point at the original location of the point. The images at 260 mm, 300 mm and 390 mm show the converging because the size of each FZP is reduced as the distance increases. The reconstructed image appears at 470 mm and is the least circle of confusion (LCC) [6-96] image because it accompanies the focused images in  $0^\circ$  direction at 455 mm and in  $90^\circ$  direction at 490 mm. The focused image is not a point but it has a finite area. After focusing, the images expand more and more as the distance increases until recovering their initial FZPs as shown in the image at 645 mm and then disappear. Since

the rays from each FZP will trace back to their original paths to reconstruct the image of a corresponding object point, the FZP should be converged to the point. But the presence of astigmatism makes the rays hardly focus to a point. This means that the reconstructed images cannot be formed by ideal light points. This is why it is difficult to find a focused image position. As the result, the resolution including the depth direction of the reconstructed image in the electro-holography is strongly related with the astigmatism. The reason for the presence of the astigmatism in DMD is considered as the finite size of each pixel. Added on this the digital nature of the device and the operating principle of the DMD can be other contributing reasons for the astigmatism. Figure 6-7 also shows that the image at 260 mm has much lower brightness than images at other distances. This means that each light field is formed by the coherent addition of rays from each pixel, i.e., each ray has phase information. This is what makes the reconstructed image from the hologram to have a spatial position and a real entity. Each image point composing the reconstructed image is formed by a ray from each pixel in the DMD and from all pixels. The number of rays composing of each image point is corresponding to the pixel resolution of the DMD because each pixel has the size of less than 10  $\mu\text{m}$  and comprises a view image of the object. Hence each image point of the reconstructed image emits rays the same way as in point images in Fig. 6-5, though the image point arrangement is different from Hologvisio and FLA/MID because the arrangement forms the object image. Since the number of rays from each pixel can be more than the pixels in each pixel cell or elemental image, and the reconstructed image is viewed through a very narrow viewing zone angle, this is why the reconstructed image will probably provide continuous parallax when it is viewed at the viewing zone. When a hologram is displayed on a display panel, each pixel of the panel works as a point hologram of a view image of an object seen at its position in the panel. Hence the hologram in the display panel is a kind of 2-D stereo-holograms. In fact, all analog holograms on photographic plates/films can also be considered as a 2-D point hologram array, i.e., a 2-D stereo-hologram. But the distance between adjacent points is too small to discriminate them. In the analog hologram, the image distance can be comparable to its grain sizes. This is much smaller than the current pixel size of the display chips. Since the distance between images is corresponding to a pixel size and the pixel size in current display chip is in the micron range, the disparity between images may be small enough to recognize the disparity between neighboring images. However, this micron range is still too big compared with the image distance on our pupils in the natural environment and the grain size in the photographic plate/film which is in the 10th nanometer range [6-97]. The point hologram represents an image point similar to the focused rays on the center of each elemental

optic in MV and IP as shown in Fig. 3. This is why it is considered that a 2-D multiview image array as in IP and MV will be formed when the hologram on the display panel is reconstructed. However, the characteristics of each image from the hologram and MV/IP are not the same because the images from the hologram consist of rays from object points and have their own phase information but those from IP and MV an array of pixels with no phase information. The light fields of different distances in Fig. 7 is formed by the coherent addition of each view image which is reconstructed by the rays from a pixel, with those from other pixels. Each of the fields has a spatial position and a real entity. But in a light field display, the 3-D image is simply perceived by the image on the display panel through the light field. Only the image on the panel has a spatial position and real entity. As mentioned before the viewing zone angle is a parameter of determining the quality of the 3-D images. In the holographic imaging, the angle can hardly exceed more than  $30^\circ$ , even with a high pixel density panel with the pixel size of as small as  $1\ \mu\text{m}$ . A demagnifying optics can be used to increase the angle but the optics presence will make the imaging system bulkier and the image size much smaller than the panel size. The light field imaging does not need the demagnifying optics and the displayable image may not be smaller than the panel size but it is still not free from the angle problem. To project more than two different view images to each eye of viewers, either the field of view (FOV) of each elemental lens or each projector objective, or scanning angle should be minimized or increase the number of pixels within a pixel cell/elemental image. To increase the number of pixels, the pixel size should be smaller as described by the relationship in section 4. When the pixel size is considered as  $1.0\ \mu\text{m}$ , there will be 1,000 pixels within an elemental optic with a pitch of  $1.0\ \text{mm}$  in horizontal direction. If each of these pixels creates a viewing space with  $1.5\ \text{mm}$  width in horizontal direction, the 200 pixels can create  $300\ \text{mm}$  width VZCS. If this VZCS appears at around viewing distance of  $1,000\ \text{mm}$ , the viewing zone angle will be around  $17^\circ$ . But for the holographic display it will be less than  $6^\circ$ . The viewing zone angle of the light field display is bigger than that of the holographic but the values are still very small compared with that of plane image which has near  $180^\circ$ . In the light field displays, more serious problem is to find a VZFO which can resolve any number of pixels and any size of pixel within a pixel cell/elemental image. It is expected that the difficulty of resolving pixels or sub-pixels with a VZFO will grow as the pixel size decreases. As described before, the required pixel size for the light field display is not different from that for holographic display. This means that both holographic and light field imaging can be displayed on a same display panel. However, the reconstructed image size of the hologram cannot be as large as the light field image. The size will be much smaller compared with the panel size. This is

because the viewing zone angle depends on not even the pixel size but also relative size of reconstructed image to panel and the image distance from the hologram [6-98]. As mentioned before, the focusable depth range and the extension of viewing zone in depth direction are different for the two imaging. This means that the image spaces between the two imaging will also be different. In the light field display, the image space will be defined as the focusable image depth range in the front and rear spaces of the panel. The range can be extended up to near the pupil of viewers' eye by adjusting the number of simultaneously projected images [6-28], but how much is not known yet. Hence the image space in front of the display panel can be extended to near the end of the viewing zone because the images perceived at image cells where viewers' each eye is located determine the depth of the perceived images. Hence the image space for MV (IP) will be determined by its corresponding viewing zone forming geometry as in Fig. 6-3. The difference is its extension to the rear space of the panel as shown in Fig. 6-8. Figure 6-8 represents the image space of the light field display, having a diamond shaped space.

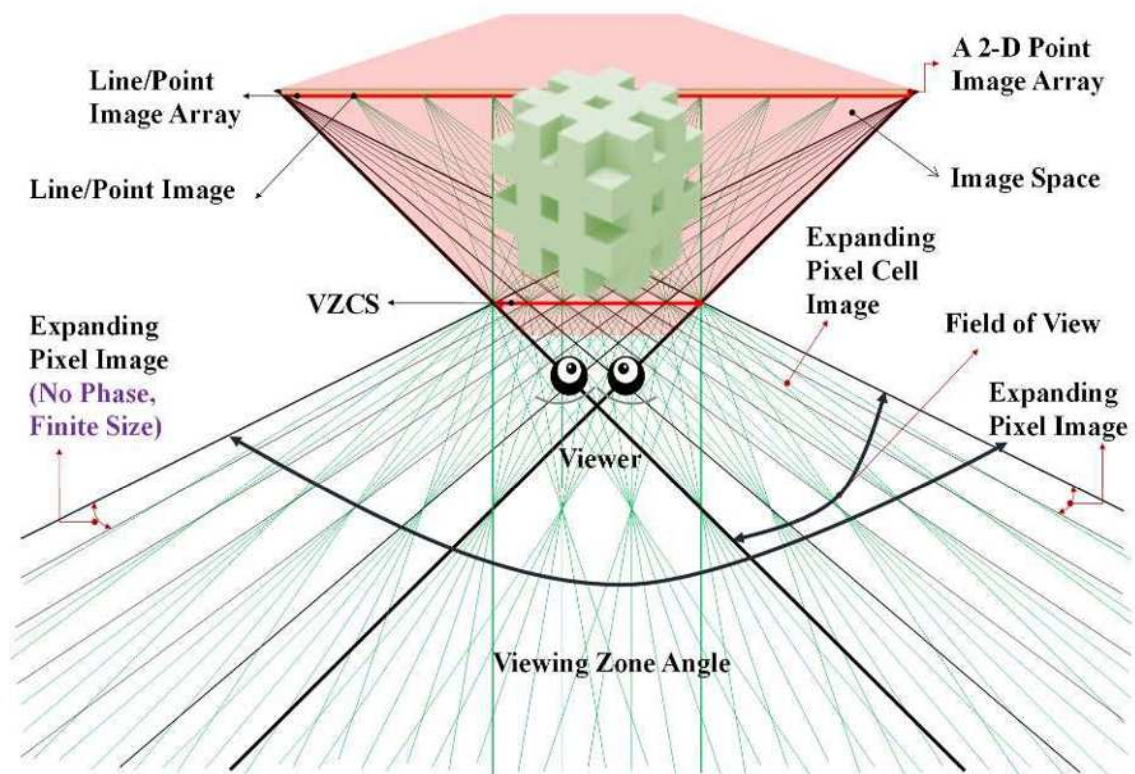


Fig. 6-8. Image space in a light field display

The geometry comes from the radial-type viewing zone forming geometry. In the holographic imaging, the image space for a real image is defined as the pyramidal shape space specified in Fig. 6-9. Figure 6-9 represents the real image reconstructing geometry of the holographic display. The rays from each point hologram, i.e., each pixel is converged to the common space where the reconstructed image will appear.

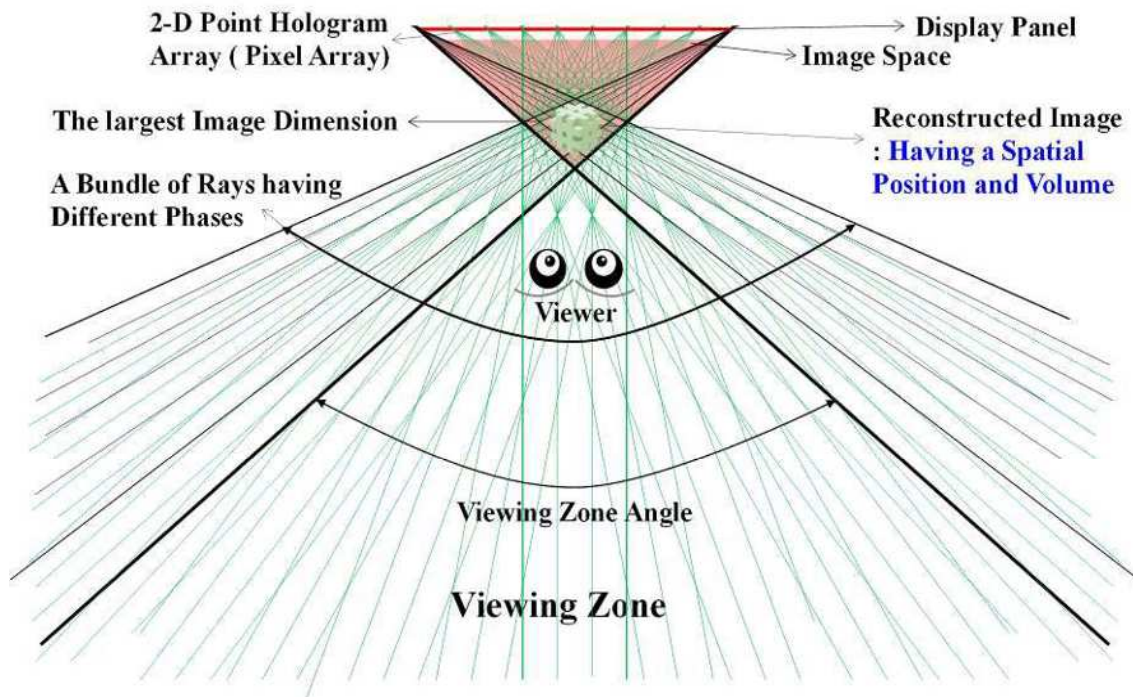


Fig. 6-9. Image space in a Holographic display

Hence the geometry is very similar to the radial type viewing zone forming geometry as in Fig. 6-3(a). However, the viewing zone in Fig. 6-9 is corresponding to the incomplete viewing zone in Fig. 6-3(a). Figure 6-9 informs that the viewing zone will appear at farther distance from the reconstructed image as the image size increases. When the size is bigger or equal to the panel size, no viewing zone will be formed. The reconstructed image will not be identified at near the hologram because the diffraction effect by being a digital chip makes the reconstructed images accompanied with different order beams to interfere each other. This interference keeps its status until the diffracted beams reaches to the plane where different orders of diffraction beams are completely separated because each diffracted beam accompanies a reconstructed image. So, the space between the hologram and the plane will not allow appearing of identifiable reconstructed images. For the case of the viewing zone extension in depth

direction, the holographic imaging has much extended viewing zone compared with the light field imaging. In the holographic imaging, the viewing zone can be theoretically extended to infinity from the starting position of the viewing zone. However, for the light field imaging, there is no solid criterion of determining the amount of the extension. But it is expected that the extension will be more as the number of different view images increase. The differences in the quality parameters between holographic and light field imaging are summarized in Table 6-1.

Table 6-1. Comparisons of the quality parameters between holographic and light field imaging

Items	Holographic-Display	Light Field Display	Remark
An image Point Size	<b>A Pixel</b>	<b>*A pixel cell</b>	*Elemental Image
Image Unit	<b>A Ray</b>	<b>*A Pixel</b>	*Have a Finite Size
Phase Information	<b>Present</b>	<b>Absent</b>	
Image Points Number	<b>Pixel resolution</b>	<b>*Pixel cell Numbers</b>	* Lower resolution
Reconstructed Image Size	*Smaller than Panel size	Close to Panel size	*Depends on Depth
Recorded Image	Almost continuous	Discretized	
Viewing Zone Angle	Pixel size, Relative size of reconstructed image to panel, Image location	Field of view, Number of pixels in a Pixel cell and F	F: Focal length of Elemental Optics
Depth Presence	Real	*Virtual	*Vergence
Adaptability to a Large size Panel	Difficult	Easy	Relative
Perceivable Depth Range	*Front and rear spaces of a panel	Near Panel	*No Near Panel Spaces: Diffr. Effect
Depth Resolution	Astigmatism	*Pixel Size	*Camera +Display

## 6.6 Problems and current issues in holographic and light field imaging

As mentioned before, for the realization of the light field displays, a display panel having a pixel (or a sub-pixel size) size less than  $5\mu\text{m}$  is needed, when the viewing distance is set to 1000 mm. The commercially available displays are mostly having the 4k UHD ( $3840 \times 2160$ ) class. The smallest size monitor having 4k resolution is 24 inch [6-99], This gives a pixel size of around  $138 \mu\text{m}$ . The smallest size display having 8k UHD ( $7680 \times 4320$ ) used to display IP image was around 27 inch [6-100]. This display has a pixel size of around  $88.5 \mu\text{m}$  but it is no longer commercially available. The commercially available the 8k UHD display has 98 inch size. Hence

the pixel size is around  $282\ \mu\text{m}$  that is more than two times of the 4K monitor. Hence building the light field display with the currently available monitors or TVs will be very difficult even the viewing distance is set to 500 mm. The LCoS chip with the same 8k UHD resolution with  $4.8\ \mu\text{m}$  pixel size had also been introduced but this chip was used to display a hologram [101] but it is no longer available. So, the light field displays introduced so far will not be the light field display as they claimed according to the definition in this paper, except the one with  $4.25\ \mu\text{m}$  sub-pixel size [6-21]. But a 5.26 inch display panel with 2250 pixels per inch is currently in development for mobile application [6-102]. This panel will have approximately  $11\ \mu\text{m}$  pixels. If each pixel in this panel consists of sub-pixels, the sub-pixel size will be approximately  $3.75\ \mu\text{m}$ . Hence it will be possible to build a light field display with this panel. Since the viewing distance of the mobile display will be at most 600 mm, the sub-pixel size will be good for building a light field display. Regarding the light field display, it is also very important to find the relationship between the number of simultaneously projected images on the pupil of each eye, and focusable depth range extension and the presence of monocular depth. As mentioned before, the two simultaneously projected images can extend the DOF to the SM zone [6-22]-[6-76] and as the number of images increases to 3 and 4, the DOF expands more to the SM zone [6-28]. This is shown in Fig. 6-10. Figure 6-10 shows the DOF values for a 23 years old male with more than 1.5 eyesight when 2, 3 and 4 different view images with a pixel disparity between image are projected to subject's each eye. The displayed images are a repeatedly moving Malta cross with a perspective within the diopter ranges  $-2.86$  to  $-0.61(2.2)$ .

The DOF ranges for 2, 3 and 4 different view images to each eye are  $-0.6 \sim -2.0$  ( $-1.4$ ),  $-0.4 \sim -2.1$  ( $-1.7$ ) and  $-0.45 \sim -2.5$  ( $-2.05$ ) diopters, respectively. The DOF ranges are increasing from  $-1.4$ ,  $-1.7$  to  $-2.05$  as the number of different view images increases and they are much wider than the DOF for stereoscopic images,  $-1.66 \sim -1.03(0.6)$  diopters.

In the holographic imaging, viewing angle [103,104,105] and image size increase [6-106]-[6-108] based on various multiplexing methods, and full color image generation [6-109], [6-110] have been the major topics to overcome the limitations imposed by the small sizes of digital display chips, and their low resolutions and large pixel sizes in current display chips. The frequently employed methods to resolve the limitations are multiplexing methods. The methods are combining chips with the same characteristics to make them to work virtually as a chip with bigger size and higher resolution. Three different multiplexing methods such as time, spatial and spatiotemporal are currently known [6-1].

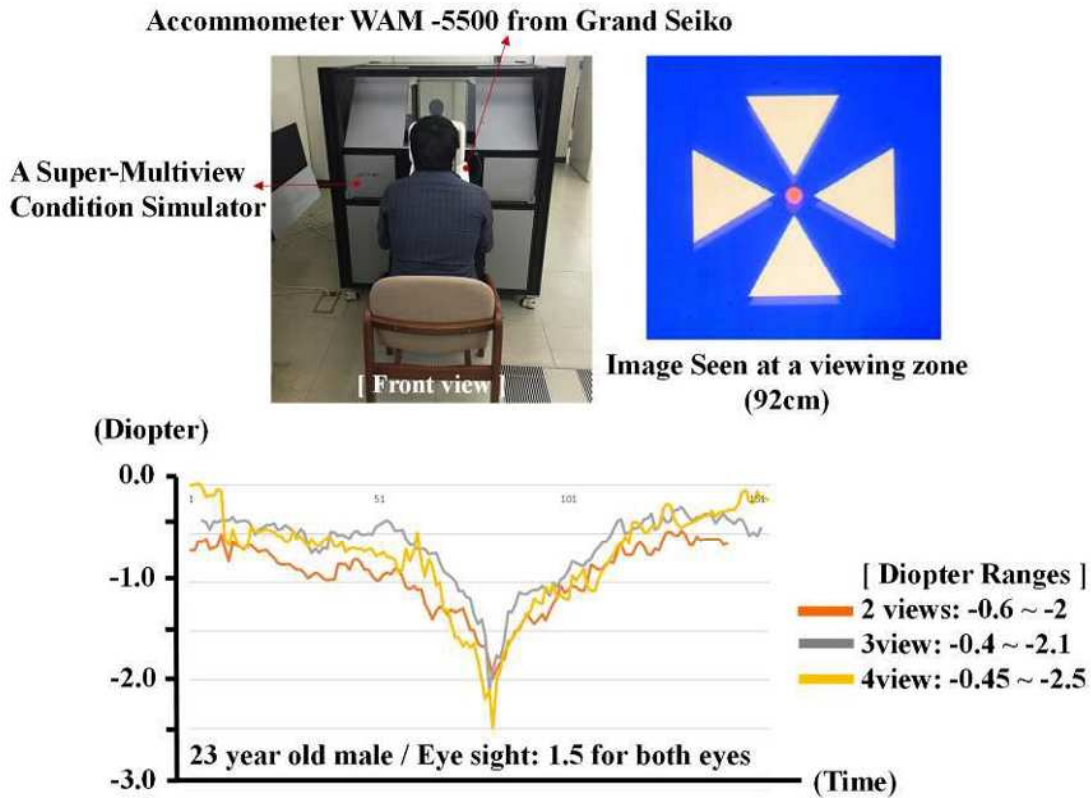


Fig. 6-10. DOF values when 2, 3 and 4 different view images are simultaneously projected

The time multiplexing is typical for a high-speed chip such as DMD, the spatial [6-107] and spatiotemporal [6-104], [6-111] for SLM. However, the multiplexing methods can bring a physically enlarged reconstructed image and more resolved multiplexed image but cannot enlarge the viewing angle because this angle is determined by the pixel size in the chip to be multiplexed. In the digital display chips, the viewing angles are the same as the diffraction angle and are defined by the pixel size for a given laser beam but this angle defines one directional size of the image space where the reconstructed image can be located. But the other direction by the crossing angle between reference and object beams in recording hologram [98]. The viewing angle defines the possible range of the directional angles to view all image pieces in a horizontal direction of the multiplexed image as shown in Fig. 6-11(a). The holographic display having  $360^\circ$  viewing angle with use of a rotation spherical mirror [6-105] is possible by the definition. The viewing angle is discrete and nothing to do with the actual viewing the reconstructed image. The angle defining the actual viewing the reconstructed image is the viewing zone angle. As

mentioned before, the reconstructed image size should be smaller than the chip size to create a viewing zone. The image size relative to the chip size determines the viewing zone distance from the reconstructed image; bigger makes longer. In Fig. 6-11, the viewing zone forming geometry of both time (Fig. 6-11(a)) and spatial (Fig. 6-11(b)) multiplexing are depicted. For the case of the time, the multiplexed frames (holograms) are on the circumference of a circle centered the center of the scanning mirror. In the opposite side of the arc where the multiplexed frames are located, the starting point of each hologram's viewing zone is located. Figure 6-11(a) shows that the reconstructed image piece from a frame is joined sequentially with time, with the reconstructed images from the holograms on other frames to form a physically enlarged or more resolved multiplexed image. However, the viewing zone for each image piece from a frame do not overlapped with those for other image pieces. There is not any common viewing zone for viewing the multiplexed image simultaneously but each image can be viewed at its own viewing zone. This is why a diffusing screen is needed to see the multiplexed image. In the geometry, if a demagnifying lens is located at the viewing zone, the reconstructed image can be demagnified and each viewing zone can be enlarged but no common viewing zone for the contracted multiplexed image. For the case of spatial multiplexing, in principle the multiplexed chips can have a common viewing zone as shown in Fig. 6-11(b). The viewing zone is defined as the common space formed by the lines connecting the four corners of multiplexed chips and the edges of the largest dimensions in each directions of the object image in the parallel plane of the chips. In this case,  $\alpha$  which is the angle between the line passing to the top edge of the multiplexed chips and parallel to the normal line of the chips, and the line connecting the top edge and the bottom of the reconstructed image should not exceed the crossing angle between reference and object beams.

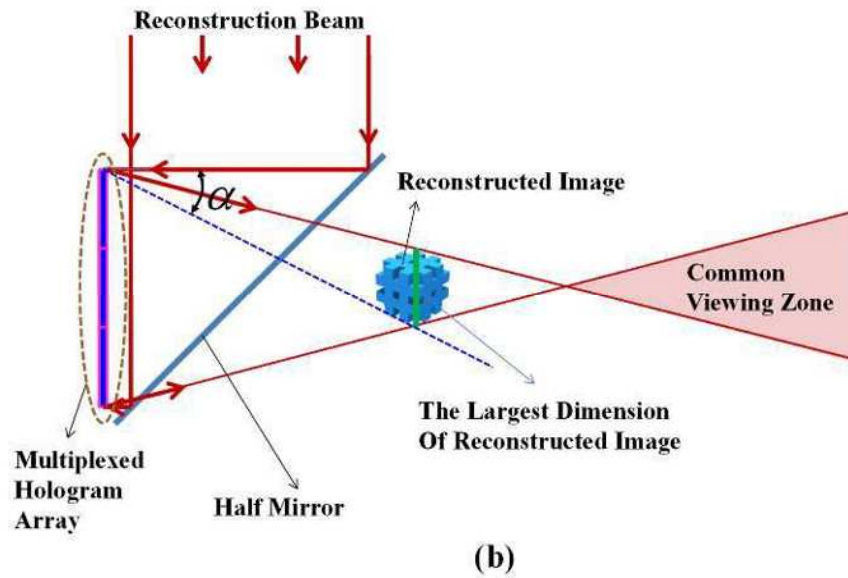
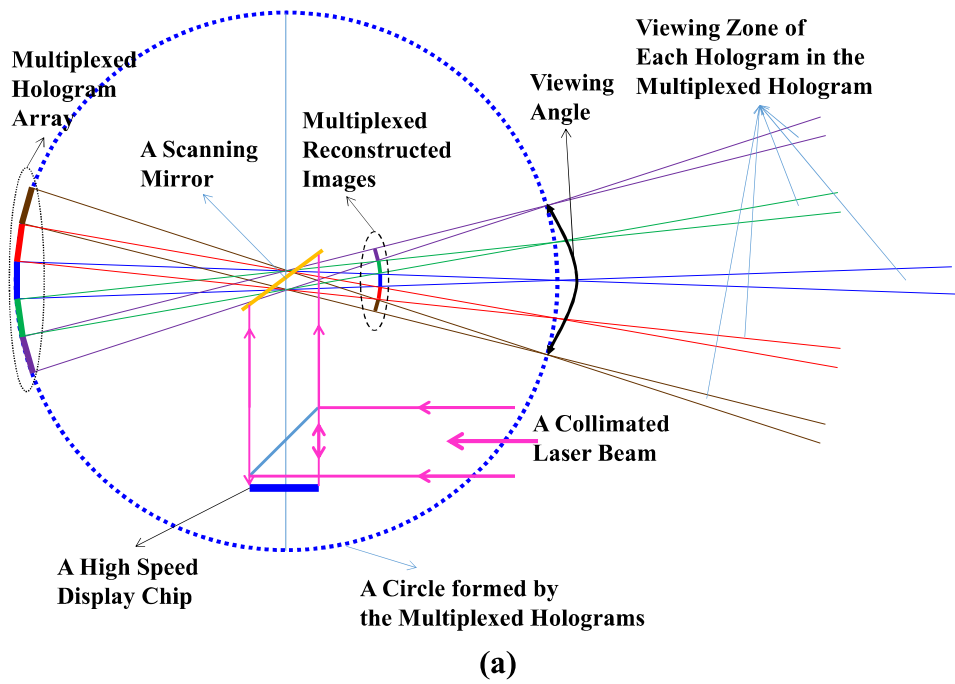


Fig. 6-11. Viewing zone forming geometries of (a) time and (b) spatial multiplexing

When  $\alpha$  is bigger than the crossing angle, each display chip should be individually illuminated. In this multiplexing, the viewing zone can be further expanded by sacrificing the viewing zone angle. In this sense, a chip with smaller pixel size will be better to apply the spatial multiplexing as shown in Fig. 6-11(b). There is a

possible way of joining the viewing zone of multiplexed chips. This is shown in Fig. 6-12. The relative position of the reconstructed image from each chip to be multiplexed is adjusted such that its reconstructed image is joined with others and the starting point of viewing zone is superposed with those of others [6-104]. In this way, the viewing zone will also be joined but there still no common viewing zone for the multiplexed images. Hence a diffuser is also needed to view the multiplexed image. Regarding the full color display, the developments are not very noticeable.

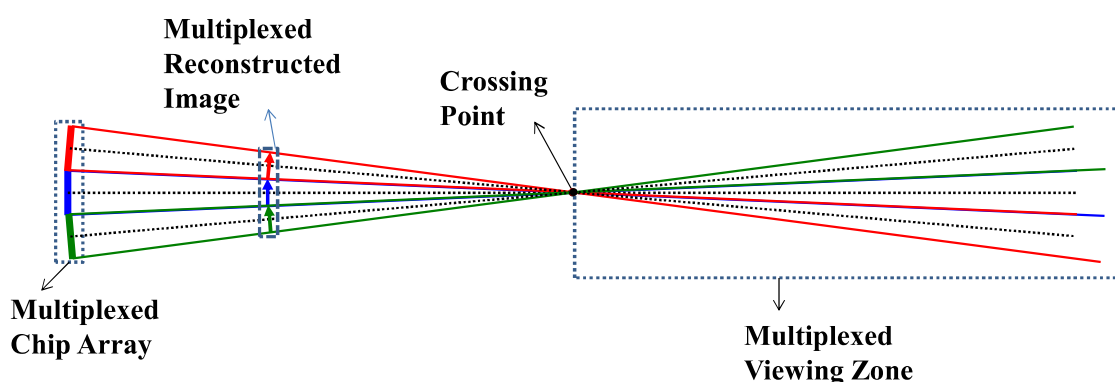


Fig. 6-12. A possible way of joining the viewing zone of multiplexed display chips

## 6.7 Future progresses in the holographic and light field displays

The current developments of light field and holographic imaging rely mostly on the flat panel displays. In this way, the two imaging can be in a same display for plane images. The display will be the future TV at home. The final goal of the two imaging is creating the natural viewing condition through the display. The minimum requirement of achieving the goal is providing both continuous parallax and large extended focusable image depth range. In this regard, the questions such as 1) “Will it be possible to increase the DOF further and to have a monocular depth with more than two neighboring view images? And 2) how many different view images are needed to create a natural viewing condition?” should be answered. To satisfy the requirement, a display panel specialized for the light field and holographic displays should be developed in future. Since the panel requirements for the two imaging are not different, the same panel can be used for these two imaging. The display for these two imaging is in development: A display chip with 1  $\mu\text{m}$  pixel size based on giant magneto-resistive (GMR) material [86] and an LCoS display chip with 8k UHD resolution [103] had already been used to display hologram. Furthermore, a 2250 Pixels/inch display panel for mobile application is in development to build a light field

display. These chips and display are still small in size but they will work as the steppingstones for future holographic and light field displays. Eventually, the panel/chips should have the resolution and pixel density to display 3-D images with image quality comparable to that of the plane image, In this regard, the panels and chips with the size for a smart phone and a pixel size close to  $1\ \mu\text{m}$  with no diffraction beams are desired, especially for the holographic displays. They make the displays to have a simpler structure and better image quality than now. The diffraction beams are inevitable in the digital display chips/panels. They are annoying and reducing the light efficiency of them tremendously. A way of eliminating them should be found. And also, if lasers are continuously used for the displays, eye safety problem should be more thoroughly investigated [6-112]. Regarding the light field displays, there is another opportunity of building them with use of pico-projectors [6-113]. The dimension of a pico- projector is reduced to the size of a smart phone and its pixel resolution is reached to near Full HD ( $1920 \times 720$ ). So, it is easier to aligning many of them in a line within a fixed space to build the 2-D version of FLA/MID or Holovizio. Building a large dimension light field display with an array of pico-projectors will be much beneficial than with the chips or the display. This is because the projector array does not need the VZFO. As the pixel size decreases, the VZFO's resolving power of small size pixels should be increases, the current lenticular and parallax barrier will have difficulties in resolving pixels with sizes less than  $20\ \mu\text{m}$  [6-114]. Hence to realize a light field display with a display panel specialized for 3-D imaging, a method of improving the resolving power of the current VZFOs or a new VZFO should be developed. In building the light field display, more number of different view images than the current Multiview imaging will be required. For this purpose, the number of pixels should be increased by increasing the pixel density physically or virtually. However, since the pixel size becomes smaller as the pixel density increases, the pitch size of the VZFO's elemental optics can be reduced to smaller than that in the Multiview imaging. In this case, the image cell may not be discriminated from those of its adjacent by the diffracted beam from each elemental optic. So, the pitch size should be designed to make the diffracted beam size smaller than the image cell size.

## 6.8 Conclusions

IP's equivalent optical geometry of arranging multiview images as a 2-D point image array has been the basis of all contact-type multiview 3-D imaging introduced so far, i.e., FLA/MID and Holovizio, and electro-holographic displays based on digital display chips. Hence it is no doubt that the same geometry will be used to the future holographic and light field displays. The criteria separating the holographic and light field imaging from

Multiview imaging are the presences of continuous parallax and large focusable image depth. These two quality parameters are essential to create the natural viewing condition which is the ultimate goal of the displays for the imaging. The first requirement to satisfy these parameters will be a display panel having a pixel size close to 1  $\mu\text{m}$ . A pixel having an irregular shape will be better to increase the light efficiency by eliminating the diffraction pattern. Since the panel requirements for the light field and holographic displays are almost the same and they have the same goal, they can be on a display panel with the plane images in future. A display panel/chip specialized for the 3-D imaging is the shortcut for the success of 3-D images in the market in future.

## 7. Summaries and conclusions

The main goal of this paper is to understand moiré phenomenon in 3D display and to find out how to minimize moiré. We can easily find moiré phenomenon even in daily life. This moiré phenomenon can also be confirmed on a 3D display, which is different from the moiré phenomenon in a typical 2D display. The moiré phenomenon in the 3D display not only changes the moiré pattern according to the direction of the observer's view direction but also depends on the thickness and period of the display medium used. This difference is a major factor in deteriorating the quality of the image in the 3D display, which interferes with the viewer. In order to minimize the moiré phenomenon in the 3D display, the characteristics of the moiré phenomenon in the 3D display are studied. In this study, geometric characteristics (chirping phenomenon) and color characteristics of moiré are mathematically expressed and confirmed through experimental verification. Based on these results, we can accurately predict moiré in 3D display. In the slanted type 3D display, moiré phenomenon can also be defined using mathematical expressions and algorithms and can be confirmed by an experimental method through simulation. In addition, the basic principles and formation process of 3D display image are explained by geometric concept diagram and mathematical expression. As a representative method of 3D display image, we introduce the principle of hologram and light field imaging method through geometrical concept diagram and experiment.

In chapter 2, mathematical theory was developed to verify that chirped moiré patterns are generated when two overlapping regularly patterned VZFOs have thickness. The verification of the moiré phenomenon was done through the developed simulator. Simulation results are one of the essential elements for characterizing moiré characteristics. The chirped moiré fringes are shifted by changing the viewing position of the viewer, and the shifted period variation changes with increasing / decreasing viewing distance and viewing angle. A chirped moiré fringes are created because the bottom plate pattern is visible through the top plate. The bottom plate is deflected as it passes through the top plate and through the top plate, and the uniform period changes due to the chirped period due to the refraction. The chirping of moiré fringes becomes clearer as the viewing angle increases and the viewing distance decreases. This is a phenomenon because it depends on the viewing distance and plate length. The chirp characteristics of moirés can be used to measure the refractive index of the material.

In Chapter 3, the color moirés in contact-type 3-D imaging represent differently from the conventional moirés based on beat phenomenon. The difference is in the presence of the VZFO material thickness, a large period difference between the pixel and VZFO's equivalent line patterns and blocked pixel pattern by the VZFO line pattern. The color of this moiré phenomenon cannot be eliminated completely. Conventional moiré minimization methods increase the crosstalk between neighboring images and cause a problem of reducing the number of active pixels and image sharpness. Therefore, in this study, we developed the method of quantification of moiré by using equations, simulations, and experiments. These results were applied to 3D display to predict moiré.

In chapter 4, the color moiré fringes appearing in the contact-type 3-D displays, can be characterized by developed equation. The formation of the moiré pattern fringe is explained using the concept of geometric formation and verified by simulation and experiment using VZFO with different line thickness. Mathematical expressions of moiré are applied under conditions of various 3D displays. We also experimentally verify the reduction of the contrast of the moiré pattern due to the reduction of the line thickness of the VZFO line period.

In Chapter 5, we introduced an algorithm for simulating slanted color moirés for angular ranges of 0 to 45 degrees in a 3D display. In a 3D display, the color moiré is induced by periodically blocking the pixel pattern of the panel by the equivalent line pattern of the VZFO. This concept is useful as a way to find a way to minimize color moiré in a 3-D display. In order to find the method of moiré minimization we verified by using the developed simulation algorithm. The simulation results inform that the angles used before to minimize the color moirés are different from the angle which is considered as minimizing the color moiré contrast in this chapter. The application of the minimized color moiré pattern is introduced through an experimental example.

In Chapter 6, the parameters defining the image quality of 3-D imaging are defined. Also, we introduced the geometric principles of all contact multi-view 3-D images such as electronic hologram display, holographic, FLA / MID based on digital display chip. In particular, it describes the criteria for separating hologram and light field

imaging from multiview imaging. The separation criterion is the presence of continuous parallax and a large focusable image depth. These two quality parameters are essential to create a natural observation condition, the ultimate goal of the display for the image. To understand the phenomenon of moiré in the 3D display should know the difference and the geometric principles in 3D display. This understanding of 3D display is essential for understanding and minimizing moiré phenomenon in the future.

# Reference

## Chapter 1.

- [1-1] V. Saveljev, J.-Y. Son, B. Javidi, S.-S. Kim, and D.-S. Kim, "Moiré minimization condition in three-dimensional image displays," *J. Disp. Technol.* 1(2), 347–353 (2005).
- [1-2] J. Kim, J.-Y. Son, K.-H. Lee, H. Lee and M.-C. Park, "Behaviors of moiré fringes induced by plate thickness," *journal of Optics* 17, 035801, (2015)
- [1-3] V. V. Saveljev, Jung-Young Son and Kyung-Hum Cha, "about a moiré-less condition in Non-Square Grids," *journal of Display Technology*, V4(3), 332-339, (2008)
- [1-4] V. Saveljev and S.-K. Kim, "Three-dimensional Moiré display," *J. Soc. Inf. Disp.* 22(9), 482–486 (2014).
- [1-5] V. Saveljev, "Orientations and branches of moiré waves in three-dimensional displays," *J. Korean Phys. Soc.* 57(6), 1392–1396 (2010).
- [1-6] V. Saveljev and S.-K. Kim, "Simulation and measurement of moiré patterns at finite distance," *Opt. Express* 20(3), 2163–2177 (2012).
- [1-7] V. Saveljev and S.-K. Kim, "Estimation of contrast of moiré patterns in 3D displays," in *Proceedings of 14th International Meeting on Information Display (IMID)*, (2014), pp. 417.

## Chapter 2

- [2-1] I. Amidror 2000 *The Theory of the Moiré Phenomenon*, Kluwer Academic Publishers
- [2-2] O. Kafri and I. Glatt 1989 *The Physics of Moire Metrology*, John Wiley and Sons, New York
- [2-3] A. Aghion. et al. 2014 "A moiré deflectometer for antimatter", *Nature Communications*, 5, 4538
- [2-4] J. Shao. Y. Ding, H. Tian, X. Li, Xian Li and H. Liu, 2012 "Digital moiré fringe measurement method for alignment in imprint lithography," *Optics & Laser Technology*, 44(2), 446-451
- [2-5] Victor J Cadarso. et al. 2013 "High-resolution 1D moirés as counterfeit security features" *Light: Science & Applications*, 2, e86
- [2-6] A. Schilling, W.R. Tompkin and R. Staub, 2006 "Diffractive moire features for optically variable devices," *Proc SPIE*, 6075, 60750V1-12

- [2-7] R. A. Steenblik, M. J. Hurt, 2004 “Unison Micro-optic Security Film,” Proc SPIE 5310, 321–327
- [2-8] F.P. Chiang and B. Ranganayakamma 1971 “Deflection measurements using moirè gap effect”, Experimental Mechanics, 11, 296-302
- [2-9] F.P. Chiang and R.M. Juang 1973 “A method to shift moirè fringes using gap effect”, Experimental Mechanics, 13, 209-211
- [2-10] Jung-Young Son, Vladimir V. Saveljev, Yong-Jin Choi, Ji-Eun Bahn and Hyun-Hee Choi, 2003 “Parameters for Designing Autostereoscopic Imaging Systems Based on Lenticular, Parallax Barrier and IP Plates”, Optical Engineering, 42, 3326-3333
- [2-11] Vladimir V. Saveljev, and Sung-Kyu Kim, 2012 “Simulation and measurement of moirè patterns at finite distance”, Optics Express, 20(3), 2163-2177
- [2-12] V. V. Saveljev, Jung-Young Son and Kyung-Hun Cha, 2008 “About a moire-less condition in Non-Square Grids,” IEEE/OSA J. of Display Technology, 4(3), 332-339
- [2-13] Y. Nishijima and G. Oster, 1964 “Moiré Patterns: Their Application to Refractive Index and Refractive Index Gradient Measurements,” JOSA, 54(1), 1-5
- [2-14] N. Sultanoba, S. Kasarova, and I. Nikolov, 2009 “Dispersion properties of optical polymers,” Acta Physica Polonica A, 116, 585-587: (Please reference also <http://refractiveindex.info>)
- [2-15] B. R. Mahafza, 2005 Radar Systems Analysis and Design using MATLAB, 2nd Edition, Chapman & Hall/CRC, Boca Raton, Florida
- [2-16] M. Abramowitz, I. A. Stegun, 1972 Handbook of Mathematical Functions with Formulas, Graphs, and Mathematical Tables, Dover, New York

### **Chapter 3.**

- [3-1] F. Okano, H. Hoshino and I. Yuyama, “Real Time Pickup Method for a Three Dimensional Image Based on Integral Photography,” Appl. Opt. V36, pp1598-1603 (1997)
- [3-2] Jung-Young Son and Bahram Javidi, “3-Dimensional Imaging Systems Based on Multiview Images,” (Invited Paper), IEEE/OSA J. of Display Technology, V1(1), pp125-140 (2005)

- [3-3] Jung-Young Son, Bahram Javidi and Kae-Dal Kwack, "Methods for Displaying 3 Dimensional Images" (Invited Paper), Proceedings of the IEEE, Special Issue on: 3-D Technologies for Imaging & Display, V94(3), pp502-523 (2006)
- [3-4] Jung-Young Son, Hyoung Lee, Beom-Ryeol Lee, Kwang-Hoon Lee, "Holographic and Light-Field Imaging as Future 3-D Displays," (Invited) Proc. of the IEEE, 105(5), 1-16 (2017).
- [3-5] Yoon-Chul Song, Vladimir V. Saveljev, Jung-Young Son, Seok-Won Yeom, Yu. A. Vashpanov, "Conditions for Moiré Free Contact-Type 3 Dimensional Displays", J. of Optical Society of Korea, V12(2), pp93-97 (2008)
- [3-5] F.P. Chiang. et al. A method to shift moiré fringes using gap effect", Experimental Mechanics. 13. 209-211 (1973)
- [3-6] O. Kafri. et al. The Physics of moiré Metrology. (John Wiley and Sons, New York (1989)
- [3-7] I. Amidror. The Theory of the Moiré Phenomenon. (Kluwer Academic Publishers (2000)
- [3-8] Victor J Cadarso. et al. High-resolution 1D moirés as counterfeit security features. Light: Science & Applications, 2, e86 (2013)
- [3-9] K. T. Kim and Jung-Young Son, "Lenticular Plate 3 Dimensional Image Display Technology," (Translation), Gidari Co, Seoul, Korea (2003)
- [3-10] Jaisoon Kim, Jung-Young Son, Kwang-Hoon Lee, Hyoung Lee and Min-Chul Park, "Behaviors of moiré fringes induced by plate thickness", Journal of Optics. 17(3), 035801, Feb 20, 2015
- [3-11] Hyoung Lee, Sung-Kyu Kim, Kwanghoon Son, Jung-Young Son, and Oleksii O. Chernyshov, "Fringe periods of color moirés in contact-type 3-D displays," Opt. Express, 24(13), 14183-14195 (2016).
- [3-12] Beom-Ryeol Lee, Jung-Young Son, Oleksii O. Chernyshov, Hyoung Lee and Ilkwon Jeong, "Color moiré simulations in contact-type 3-D displays", Optical Express, 23(11), 14114-14125, (2015).
- [3-13] Vladimir V. Saveljev, Jung-Young Son, Bahram Javidi, Sung-Kyu Kim and Dae-Sik Kim, "A Moiré Minimization Condition in 3 Dimensional Image Displays," IEEE/OSA J. of Display Technology, V1(2), pp347-353 (2005)
- [3-14] Jung-Young Son, Beom-Yul Lee, Min-Chul Park and Hyoung Lee, "Moiré reduction by a diffuser in a multiview three-dimensional imaging system", J. of Soc. for Information Display, V19(12), pp873-879 (2011)

[3-15] V. V. Saveljev, Jung-Young Son and Kyung-Hun Cha, "About a moire-less condition in Non-Square Grids," IEEE/OSA J. of Display Technology, V4(3), pp332-339 (2008)

[3-16] F.P. Chiang and B. Ranganayakamma, "Deflection measurements using moirè gap effect", Experimental Mechanics, V11, pp296-302 (1971)

[3-17] Jung-Young Son, Vladimir V. Saveljev, Kae-Dal Kwack, Sung-Kyu Kim and Min-Chul Park, "Characteristics of Pixel Arrangements in Various Rhombuses for Full-Parallax 3 Dimensional Image Generation," Appl. Opt., V45(12), pp2689-2696 (2006)

#### **Chapter 4.**

[4-1] J.-Y. Son, and B. Javidi, "3-Dimensional Imaging Systems Based on Multiview Images," Journal of Display Technology, 1(1), 125-140 (2005).

[4-2] B.-R. Lee, J.-Y. Son, O. O. Chernyshov, H. Lee and I.K.Jeong, "Color moiré simulations in contact-type 3-D displays," Optics express, 23(11), 14114-14125, (2015).

[4-3] J. Kim, J.-Y. Son, K.-H. Lee, H. Lee, and M.-C. Park, "Behaviors of moiré fringes induced by plate thickness," Journal of Optics 17, 035801,(2015).

[4-4] Shin-ichi Uehara, Tsutomu Hiroya, Kouji Shigemura, and Hideki Asada, "Reduction and Measurement of 3D Moiré Caused by Lenticular Sheet and Backlight" SID Symposium Digest of Technical Papers, 432-435, (2009).

[4-5] V. V. Saveljev, Jung-Young Son and Kyung-Hun Cha, "About a moire-less condition in Non-Square Grids," Journal of Display Technology, 4(3), 332-339, (2008).

[4-6] K. Nagasaki, "A 3D display with variable depth moire pattern", Proceeding of SICE Annual Conference (Aug. 20-22, 2008, Tokyo, Japan), IEEE, 1936-1941.

[4-7] Yunhee Kim, Gilbae Park, Jae-Hyun Jung, Joohwankim and Byoungcho Lee, "Color moire pattern simulation and analysis in three-dimensional integral imaging for finding the moire-reduced tilted angle of a lens array", Applied Optics, 49(11), 2178-2187, (2009).

[4-8] F.P. Chiang and B. Ranganayakamma, "Deflection measurements using moirè gap effect," Experimental Mechanics, 11, 296-302, (1971).

[4-9] Amidror, The Theory of the Moiré Phenomenon, (Kluwer Academic Publishers, 2000).

- [4-10] G. Oster and Y. Nishijima, "Moire patterns", *Scientific American*, 5(208), 54-63, (1963).
- [4-11] W. Rihaczek, *Principle of high-resolution Radar*, (McGraw Hill, New York, 1969).
- [4-12] J.-Y. Son, V. V. Saveljev, Y.-J. Choi, J.-E. Bahn and H.-H. Choi, "Parameters for Designing Autostereoscopic Imaging Systems Based on Lenticular, Parallax Barrier and IP Plates," *Optical Engineering*, 42(11), 3326-3333, (2003).
- [4-13] W.-H. Son, J.W. Kim, J.-Y. Son, B.-R. Lee and M.-C. Park, "The basic image cell in contact-type multiview 3-D Imaging systems", *Optical Engineering*, 52(10), 103107, (2013).
- [4-14] [www.ucamco.com](http://www.ucamco.com)
- [4-15] <http://imaging.nikon.com/lineup>

## **Chapter 5.**

- [5-1] Beom-Ryeol Lee, Jung-Young Son, Oleksii O. Chernyshov, Hyung Lee and Ilkwon Jeong, 2015 Color moiré simulations in contact-type 3-D displays, *Optical Express*, 23(11), 14114-14125
- [5-2] Vladimir V. Saveljev, Jung-Young Son, Bahram Javidi, Sung-Kyu Kim and Dae-Sik Kim, 2005 A Moiré Minimization Condition in 3-Dimensional Image Displays, *IEEE/OSA J. of Display Technology*, V1(2), pp347-353
- [5-3] Yunhee Kim, Gilbae Park, Jae-Hyun Jung, Joohwan Kim, and ByoungHo Lee, 2009 Color moiré pattern simulation and analysis in three-dimensional integral imaging for finding the moiré-reduced tilted angle of a lens array, *Appl. Opt.*, V48 (11), pp. 2178-2187
- [5-4] Chao-Chao Ji, Cheng-Gao Luo, Huan Deng, Da-Hai Li, and Qiong-Hua Wang, 2013 Tilted elemental image array generation method for moiré-reduced computer-generated integral imaging display, *Optics Express*, V21(17), PP. 19816-19824
- [5-5] Zhenfeng Zhuang, Phil Surman, Lei Zhang, Rahul Rawat, Shizheng Wang, Yuanjin Zheng, and Xiao WeiSun, 2016 moiré-reduction method for slanted-lenticular-based quasi-three-dimensional displays, *Optics Communications*, V381, pp. 314-322
- [5-6] Makoto Okui, Masaki Kobayashi, Jun Arai, and Fumio Okano, 2005 Moiré fringe reduction by optical filters in intergral three-dimensional imaging on a color flat-panel display, *Appl. Opt.* V44 (21), PP. 4475-4483

- [5-7] Jung-Young Son, Beom-Yul Lee, Min-Chul Park and Hyoung Lee, 2011 Moiré reduction by a diffuser in a multiview three-dimensional imaging system, *J. of Soc. for Information Display*, V19(12), pp873-879
- [5-8] H. Sasaki, N. Okaichi, H. Watanabe, M. Kano, M. Kawakita, and T. Mishina, Color moiré reduction and resolution enhancement technique for intergral three-dimensional display, *3DTV Conference: The True Vision-Capture, Transmission and Display of 3D Video (3DTV-CON)*, Copenhagen, Denmark 2017 (DOI: 10.1109/3DTV.2017.8280402)
- [5-9] S. T. de Zwart, W. L. Ijzerman, T. Dekker and W. A. M. Wolter, 2004 A Switchable Auto-Stereoscopic 2D/3D Display, *IDW'04, Proc. of the 11th International Display Workshops*, Japan, pp1459-1460
- [5-10] M.R Swash, A. Aggoun, O. Abdulfatah, B. Li, J. C. Fernández, and E. Tseklevs, 2013 Holoscopic 3D Image Rendering for Autostereoscopic Multiview 3D Display, *Broadband Multimedia Systems and Broadcasting (BMSB)*, 2013 IEEE International Symposium on, London, UK (DOI: 10.1109/ BMSB.2013.6621683)
- Amidror, 2000 *The Theory of the Moiré Phenomenon*, Kluwer Academic Publishers
- [5-11] Jaisoon Kim, Jung-Young Son, Kwang-Hoon Lee, Hyoung Lee and Min-Chul Park, 2015 Behaviors of moiré fringes induced by plate thickness, *Journal of Optics*. 17(3), 035801
- [5-12] Hyoung Lee, Sung-Kyu Kim, Kwanghoon Son-Jung-Young Son, and Oleksii O. Chernyshov, 2016 Fringe periods of color moirés in contact-type 3-D displays, *Opt. Express*, 24(13), 14183-14195

## **Chapter 6.**

- [6-1] Jung-Young Son and Bahram Javidi, "3-Dimensional Imaging Systems Based on Multiview Images," *IEEE/OSA J. of Display Technology*, V1(1), pp125-140, 2005
- [6-2] Jung-Young Son, Bahram Javidi and Kae-Dal Kwack, "Methods for Displaying 3 Dimensional Images" (Invited Paper), *Proceedings of the IEEE, Special Issue on: 3-D Technologies for Imaging & Display*, V94(3), 2006, pp502-523
- [6-3] <http://www.monitor4u.co.kr/>
- [6-4] <http://news.samsung.com/kr/3015>
- [6-5] [http://www.zdnet.co.kr/news/news\\_view.asp?artice\\_id=20110825102246&lo=zv40](http://www.zdnet.co.kr/news/news_view.asp?artice_id=20110825102246&lo=zv40)
- [6-6] A. Woods, T. Docherty and R. Koch "Image Distortions in Stereoscopic Video Systems", *Proc. SPIE* V1915, pp36-48, 1993

- [6-7] Jung-Young Son, Yuri Gruts, Joo-Hwan Chun, Yong-Jin Choi, Ji-Eun Bahn, and Vladimir I. Bobrinev, "Distortion Analysis in Stereoscopic Images", *Optical Engineering*, V41(3), pp680-685, 2002
- [6-8] *Fundamental of 3-D Imaging Techniques (Japanese Edition)*, T. Izumi(Supervisor), NHK Science and Technology Lab., Ohmsa, Tokyo, 1995
- [6-9] K. Aksit, A. Hossein, G. Niaki, E. Ulusoy, and H. Urey, "Superstereoscopy technique for comfortable and realistic 3D displays," *Opt. Lett.* V39(24), 6903-6906 (2014).
- [6-10] R. J. Collier, C. B. Burckhardt and L. H. Lin, *Optical Holography, Student Edition*, Academic Press, New York, U.S.A., 1971
- [6-11] A. Gershun, *The Light Field*, Cambridge Ma, USA: MIT, 1939, V18, pp51-151, translated from *J. Math. Phys.*, Moscow, Russia by P. Moon and G. Timoshenko.
- [6-12] M. Levoy and P. Hanrahan, "Light field rendering," In *proc, 23rd Annu. Conf. Compu. Graph. Interactive Tech.*, pp31-42, 1996
- [6-13] T. Yendo, N. Kawakami, and S. Tachi, "Seelinder, the cylindrical light field displays," *ACM SIGGRAPH 2005 Emerging technologies*. ACM, Press, New York, USA 2005.
- [6-14] A. Jones, I. Mcdowall, H. Yamada, M. Bolas, and P. Debevec, "Rendering for an interactive 360° light field display," *ACM transactions on Graphics (TOG)* V26, pp338-343, 2007.
- [6-15] G. Wetzstein, D. Lanman, M. Hirsch, W. Heidrich, et, al, "Compressive Light Field Displays," *IEEE computer graphics and Applications*, V32(5), pp6-11, 2012
- [6-16] Yamada, Hodaka, et al, "Three-Dimensional Light Field Display with Overlaid Projection," *Tenth International Conference on Intelligent Information Hiding and Multimedia Signal Processing (IIH-MSP)*, 2014. IEEE, pp407-410, 2014.
- [6-17] Yamaguchi Masahiro, and Ryo Higashida, "3D touchable holographic light-field display," *Applied optics* 55.3 (2016): A178-A183
- [6-18] Toru Iwane, "Light field display and 3D image reconstruction," *Proceeding of SPIE*, vol. 9867, doi: 10.1117/12.2227081, May 2016
- [6-19] [www.holografika.com/](http://www.holografika.com/)
- [6-20] F. Bettio, E. Gobbetti, F. Marton, G. Pintore, "Scalable rendering of massive triangle meshes on light field displays," *Computer Graphics*, V32(1), pp55-64 (2008)

- [6-21] Yasuhiro Takaki, Kosuke Tanaka, and Junya Nakamura, "Super multi-view display with a lower resolution flat-panel display," *Optics Express*, Vol. 19, Issue. 5, pp. 4129-4139 (2011)
- [6-22] Haruki Mizushina, Ippei Negishi, Hiroshi Ando, and Shinobu Masaki, "Accommodative and Vergence Responses to Super Multi-View 3D Images," *The Journal of The Institute of Image Information and Television Engineers*, 67(12) J475~j478, (2013).
- [6-23] Leno S. Pedrotti and Frank L. Pedrotti, S. J., *Optics and Vision*, Prentice Hall International, Inc., Upper Saddle River, New Jersey, USA, 1998
- [6-24] D. M. Hoffman, A. R. Girshick, K. Akeley, and M. S. Banks, "Vergence-Accommodation conflict hinder visual performance and cause visual fatigue," *J. Vis.*, V8 (3), 2008, DOI:10.1167/8.3.33
- [6-25] Y. Kajiki, H. Yoshikawa and T. Honda," Ocular Accommodation by Super Multi-View Stereogram and 45-View Stereoscopic Display", IDW'96, Proc. of the 11th International Display Workshops, PP489-492, 1996
- [6-26] Y. Takaki and H. Nakanuma, "Improvement of Multiple Imaging System Used for Natural 3D Display Which Generates High-Density Directional Images," *Proc. SPIE V5243*, 2003, pp43-49
- [6-27] Y. Takaki and N. Nago, "Multi-projection of lenticular displays to construct a 256-view super multi-view display," *Optics Express*, V18(9), pp8824-8835, 2010
- [6-28] Beom-Ryeol Lee, Jung-Young Son, Sumio Yano, ilkwon Jeong, "Increasing the depth of field in Multiview 3D images," *Proceeding of SPIE*, vol. 9867, doi: 10.1117/12.2229346, May 2016
- [6-29] Ju-Seog Jang, and Bahram Javidi, "Three-dimensional synthetic aperture integral imaging," *Optics Letters*, Vol. 27, Issue. 13, pp. 1144-1146 (2002)
- [6-30] A. Stern and B. Javidi, "3D Image Sensing, Visualization, and Processing using Integral Imaging," *Proceedings of the IEEE Vol. 94*, pp. 591-608 (2006)
- [6-31] *Three-Dimensional Imaging, Visualization, and Display*, Eds. B. Javidi, F. Okano, and J. Y. Son, (Springer, 2009).
- [6-32] T. Okoshi, *3 Dimensional Imaging Techniques*, Asakura Book Store (Japanese Edition), Tokyo, Japan, 1991
- [6-33] Ryder S. Nesbitt, Steven L. Smith, Raymond A. Molnar, and Stephen A. Benton, "Holographic recording using a digital micromirror device." *Proc. SPIE*, V3637, pp12-20, 1999

- [6-34] K. Bauchert, S. Serati, and A. Furman, "Advances in liquid crystal spatial light modulators", Proc. SPIE, V4734, pp35-43, 2002
- [6-35] Yasuhiro Takaki and Naoya Okada, "Hologram generation by horizontal scanning of a high-speed spatial light modulator," Appl. Opt. 48, 3255-3260 (2009)
- [6-36] Jung-Young Son, Vladimir I. Bobrinev and Kyung-Tae Kim, "Depth Resolution and Displayable Depth of a Scene in 3 Dimensional Images," J. Opt. Soc. Am. A, V22(9), pp1739-1745, 2005
- [6-37] John. A. Norling, "The stereoscopic Art-A reprint," Journal of SMPTE, V60, pp268-307, 1953
- [6-38] Charles Wheatstone, "On some remarkable, and hitherto unobserved phenomena of binocular vision (Part the first), Philosophical Transactions of the Royal Society of London, pp371-394, 1938
- [6-39] A. Lit, "The Magnitude of the Pulfrich Stereo-Phenomenon as a Function of Binocular Difference of Intensity at Various Levels of Illumination," Am. J. Psychology, V62, pp159-181, 1949
- [6-40] H. Isono and M. Yasuda, "Flicker-Free Field Sequential Stereoscopic TV System and Measurement of Human Depth Perception, Journal of SMPTE, V99(2), pp138-141 (1990)
- [6-41] F. E. Ives, U.S. Patent 725,567 (1903)
- [6-42] Herbert E. Ives, "Optical properties of a Lippmann Lenticulated Sheet, JOSA, V21, pp171-176, 1931
- [6-43] E. N. Leith, and J. Upatnieks, "Reconstructed Wavefront and Communication Theory
- [6-44] Knut Langhans, Christian Guill, Elisabeth Rieper, Klaas Oltmann, Detlef Bahr, "SOLID FELIX: a static volume 3D-laser display," Proc. SPIE V5006, pp161-174, (2003)
- [6-45] I. I. Kim, E. Korevaar, and H. Hakakha, "Three-dimensional volumetric display in rubidium vapor", Proceedings of SPIE, Vol. 2650, pp. 274-284, San Jose, CA, 1996.
- [6-46] E. Downing, L. Hesselink, J. Ralston, R. Macfarlane, "A Three-Color, Solid-State, Three-Dimensional Display", Science, Vol. 273, pp. 1185-1189, 1996.
- [6-47] Jung-Young Son, V. V. Smirnov, L. N. Asnis, and V. B. Volkonsky, H. S. Lee, "Real Time 3D Display with Acousto-Optical Deflectors," Proc. SPIE Vol. 3639, pp 137-142, (1999)
- [6-48] H. Yamada, C. Masuda, K. Kubo, T. Ohira, and K. Miyaji, "A 3-D Display Using a Laser and a Moving Screen," Proc. of Japan Display, 1986, pp416-419
- [6-49] Shinichi Tamura and Kokichi Tanaka, "Multilayer 3-D display by multidirectional beam splitter," Applied Optics, 21(20), 3659-3663 (1982).

- [6-50] <https://www.lgmobile.co.kr/mobile-phone>
- [6-51] [https://en.wikipedia.org/wiki/List\\_of\\_3D-enabled\\_mobile\\_phones](https://en.wikipedia.org/wiki/List_of_3D-enabled_mobile_phones)
- [6-52] J. S. Kollin, S.A. Benton and M.I. Jepsen, "Real-time display of 3-D computed hologram by scanning the image of acousto-optic modulator," SPIE Proc. V1136(G.M. Morris Ed.), #1136-60, 1989
- [6-53] J. Hamajaki, "3D Display Technologies in Japan, Present Status and 3D-TV on a CRT," ITEC'91 ITE Annual Convention, Tokyo, 1991, pp587-590,
- [6-54] H. Isono, M. Yasuda, D. Takemori, H. Kanayama, C. Yasuda and K. Chiba, "50-inch Autostereoscopic Full-Color 3-D TV Display System," Proc. of SPIE, V1669, 1992, pp176-185
- [6-55] G. Lippmann, "Epreuves reversibles donnant la sensation du relief," J. Phys. Theor. Appl., 7(1), 821-825 (1908)
- [6-56] Edward H., Adelson, and John YA Wang. "Single lens stereo with a plenoptic camera." IEEE transactions on pattern analysis and machine intelligence 14.2 (1992): 99-106.
- [6-57] Ren Ng, Marc Levoy, Mathieu Bredif, Gene Duval, Mark Horowitz, and Pat Hanrahan, "Light field photography with a hand-held plenoptic camera." Computer Science Technical Report CSTR 2.11 (2005): 1-11.
- [6-58] Manuel Martínez-Corral, Adrián Dorado, Héctor Navarro, Anabel Llavador, Genaro Saavedra, and Bahram Javidi, "From the plenoptic camera to the flat integral-imaging display," Proc. SPIE 9117, Three-Dimensional Imaging, Visualization, and Display 2014, 91170H 9 June 2014), DOI: 10.1117/12.2051119
- [6-59] <http://us.toshiba.com/computers/laptops/qosmio/X770>
- [6-60] Jung-Young Son, Byung-Gyu Chae, Wook-Ho Son, Jeho Nam and Beom-Ryeol Lee, "Comparisons of Viewing Zone Characteristics of MV and IP", IEEE/OSA JDT, V8 (8), pp464-471, 2012
- [6-61] Jung-Young Son, Wook-Ho Son, Sung-Kyu Kim, Kwang-Hoon Lee and Bahram Javidi, "3-D imaging for creating real world like environments", Proceedings of THE IEEE (Invited), V101(1), pp190-205, 2013
- [6-62] Chun-Hea Lee, Jung-Young Son, Sung-Kyu Kim and Min-Chul Park, "Visualization of Viewing Zones formed in a contact-type multiview 3-D imaging system", IEEE/OSA JDT, V8 (9), pp546-551, 2012
- [6-63] F. Okano, H. Hoshino and I. Yuyama, "Real Time Pickup Method for a Three Dimensional Image Based on Integral Photography," Appl. Opt. V36, pp1598-1603, 1997

- [6-64] Jung-Young Son, Vladimir V. Saveljev, Yong-Jin Choi, Ji-Eun Bahn and Hyun-Hee Choi, "Parameters for Designing Autostereoscopic Imaging Systems Based on Lenticular, Parallax Barrier and IP Plates", *Optical Engineering*, V42(11), pp3326-3333, (2003)
- [6-65] Beom-Ryeol Lee, Jae-Jeong Hwang, and Jung-Young Son, "Characteristics of composite images in MV and IP", *Applied Optics*, V51(21), pp5236-5243, 20, July, 2012
- [6-66] H. Isono, M. Yasuda and H. Sasaza, "Autostereoscopic 3-D LCD display using LCD-generated parallax barrier, 12th International Display Research Conference, Japan Display'92, pp303-306, 1992
- [6-67] J. Harrold, D. J. Wilkes, and G. J. Woodgate, "Switchable 2D/3D Display –Solid Phase Liquid Crystal Microlens Array," IDW'04, Proc. of the 11th International Display Workshops, Japan, 2004, pp1495-1496
- [6-68] Y. Kao, Y. Huang, K. Yang, P. C.-P. Chao, C. Tsai, and C. Mo, "An Auto-Stereoscopic 3D Display Using Tunable Liquid Crystal Lens Array that Mimics Effects of GRIN Lenticular Lens Array," SID'09 DIGEST, pp. 111 ~114, 2009
- [6-69] Yong Hyub Won, Junoh Kim, Cheoljoong Kim, Doseub Shin, Junsik Lee, Gyohyun Koo, "3D multi-view system using electrowetting liquid lenticular lenses," *Proceeding of SPIE*, vol. 9867, doi:10.1117/12.2225191, May 2016
- [6-70] Jung-Young Son, Vladimir V. Saveljev, Dae-Sik Kim, Yong-Moo Kwon and Shin-Hwan Kim, "A Three Dimensional Imaging System Based on LED Array," *Optical Engineering*, V46(10), pp103205-4(2007)
- [6-71] Y. Kajiki, H. Yoshikawa and T. Honda, "Ocular Accommodation by Super Multi-View Stereogram and 45-View Stereoscopic Display", IDW'96, Proc. of the 11th International Display Workshops, PP489-492, 1996
- [6-72] Sung-Kyu Kim, Dong-Wook Kim, Yong-Moo Kwon and Jung-Young Son, "Evaluation of the Monocular Depth Cue in 3D Displays", *Optics Express*, V16(26), pp21415-21422 (2008)
- [6-73] Y. Takaki and H. Nakanuma, "Improvement of Multiple Imaging System Used for Natural 3D Display Which Generates High-Density Directional Images," *Proc. SPIE V5243*, 2003, pp43-49
- [6-74] K. Susami, S. Abe, Y. Kajiki, T. Endo, T. Hatada and T. Honda, "Ocular vergence and accommodative state to super multi-view stereoscopic image", *3 Dimensional Image Conference 2000 by Operating Committee of 3 Dimensional Image Conference 2000*, 2000, pp155-158
- [6-75] Tibor Balogh, Peter Tamas Kovacs, Zsuzsa Dobranyi, and Gaal Gaspar Balogh, "The Hologvizio System: New Opportunity Offered by 3D Displays," *Proc. of the TMCE 2008*, (2008).75. Haruki Mizushima, Ippei

- Negishi, Hiroshi Ando, and Shinobu Masaki, "Accommodative and Vergence Responses to Super Multi-View 3D Images," *The Journal of The Institute of Image Information and Television Engineers*, 67(12) J475-j478, (2013).
- [6-76] Haruki MIZUSHINA, Junya NAKAMURA, Yasuhiro TAKAKI, and Hiroshi ANDO, "Increase in accommodation range induced by super multi-view displays," *ITE Technical Report* 37(24), 1-4 (2013).
- [6-77] Zebra Imaging Inc., M. A. Klug, C. Newawanger, Q. Huang, M.e. Holzbach, "Active digital hologram displays," U.S. Patent 7,227,674, June 2007
- [6-78] L. H. Enloe, J. A. Murphy and C. B. Rubinstein, "Hologram Transmission via Television." *The Bell System Technical Journal*, V45, pp333-335, 1966
- [6-79] S. A. Benton, "The Second Generation of the MIT Holographic Video System", *Proceeding of TAO FIRST INTERNATIONAL SYMPOSIUM on Three Dimensional Image Communication Technologies*, Dec. 6-7, 1993, Tokyo Japan, ppS-3-1-1-S-3-1-6
- [6-80] St.-Hilaire, Pierre, M. Lucente, J.D. Sutter, R. Pappu. C. D. Sparrell and S. A. Benton, "Scaling Up the MIT Holographic Video System," *Proc. SPIE*, V2333, pp374-380, 1994
- [6-81] J. Y. Son, S. Shestak, S.K. Kim, V. Epikhan, "A Multichannel AOM for Real Time Electroholography", *Applied Optics*, 38(14), pp.3101-3104 (1999).
- [6-82] S. A. Benton, V. M. Bove, *Holographic Imaging*, (Wiley, 2008)
- [6-83] K. Maeno, N. Fukaya, O. Nishikawa, K. Sato and T. Honda, "Electro-Holographic Display Using 15-Megapixel LCD," *SPIE*, V2652, 1996, pp15-23
- [6-84] Jung-Young Son, Oleksii Chernyshov, Hyoung Lee, Beom-Ryeol Lee, Min-Chul Park, "Resolution of electro-holographic image," *Proceeding of SPIE*, vol. 9867, doi: 10.1117/12.2229345, May 2016.
- [6-85] Min-Chul Park, Beom-Ryeol Lee, Jung-Young Son, and Oleksii Chernyshov, "Properties of DMDs for Holographic Displays", *Journal of Modern Optics*, V62(19), pp1600-1607, 2015
- [6-86] K. Machida, D. Kato, T. Mishina, H. Kinjo, K. Aoshima, K. Kuga, H. Kikuchi and N. Shimidzu, "Three-Dimensional Image Reconstruction with a Wide Viewing-Zone-Angle Using a GMR-Based Hologram," *Digital Holography and 3D Imaging Technical Digest*, DTh2A.5, OSA, 2013
- [6-87] D. Pasltis, and F. Mok, "Holographic memories," *Scientific American*, 273(5), pp. 70-76, 1995

- [6-88] Jung-Young Son, Yuriy Vashpanov Moon-Seok Kim, Min-Chul Park and Jae-Soon Kim, "Image light distribution in the multiview 3-D imaging system," IEEE/OSA Journal of Display Technology V 6(8), pp. 336-345, 2010
- [6-89] Jung-Young Son, Vladimir V. Saveljev, Jae-Soon Kim, Sung-Sik-Kim and Bahram Javidi, "Viewing Zones in 3-D Imaging Systems Based on Lenticular, Parallax Barrier and Microlens Array Plates", Applied Optics, 43(26), 4985-4992(2004)
- [6-90] Jung-Young Son, Vladimir V. Saveljev, Sung-Kyu Kim and Kyung-Tae Kim, "Comparisons of the Perceived Image in Multiview and IP Based 3 Dimensional Imaging Systems," Japanese J. of Applied Physics, V46(3A), pp1057-1059, 2007
- [6-91] Wook-Ho Son, Jinwoong Kim, Jung-Young Son, Beom-Ryol Lee and Min-Chul Park, "The basic image cell in contact-type multiview 3-D Imaging systems", Optical Engineering, 52(10), pp. 103107-1 ~ 103107-11, Oct 10, 201387
- [6-92] Jung-Young Son, Shin-Hwan Kim, Dae-Sik Kim and Bahram Javidi, "Image Forming Principle of Integral Photography," IEEE/OSA J. of Display Technology, V4(3), pp324-331, 2008
- [6-93] Beom-Ryeol Lee, Jeung-Chul Park, Il-Kwon Jeong, Jung-Young Son, "Properties of a super-multiview image", Proc. SPIE, V9117, 91170Z, Aug 28, 2014
- [6-94] <http://www.ti.com/dlp>
- [6-95] W. J. Dallas, Computer Generated Holograms, Springer-Verlag, Berlin, Germany, 1980
- [6-96] F. A. Jenkins, H. E. White, Fundamental of Optics, Korean Student Edition, McGraw- Hill, New York, 1976
- [6-97] P. Hariharan, Optical Holography: Principle, techniques and applications, New York, U.S.A., Cambridge University Press, 1984
- [6-98] Jung-Young Son, Jin-Woong Kim, Kyung-Ae Moon, Jae-Han Kim, "Viewing conditions of multiplexed holographic images", Optics and Lasers in Engineering, pp63-73, Apr 07, 2015. doi: 10.1016/j.optlaseng.2015.03.014
- [6-99] Dell P2415Q, <http://accessories.ap.dell.com/>

- [6-100] Jun Arai, Masahiro Kawakita, Takayuki Yamashita, Hisayuki Sasaki, Masato Miura, Hitoshi Hiura, Makoto Okui, and Fumio Okano, "Integral three-dimensional television with video system using pixel-offset method," *Optics Express*, 21(3) 3474-3485 (2013).
- [6-101] Kenji Yamamoto, Yasuyuki Ichihashi, Takanori Senoh, Ryutaro Oi, and Taiichiro Kurita, "3D objects enlargement technique using an optical system and multiple SLMs for electronic holography," 20(19), 1137-21144 (2012).
- [6-102] "Samsung develops '11K' super-resolution display along with 13 companies ... putting 26.5 million USD for 5 years" <http://english.etnews.com/20150710200002>
- [6-103] T. Senoh, T. Mishina, K. Yamamoto, O. Ryutaro, and T. Kurita, "Viewing-Zone-Angle-Expanded Color Electronic Holography System Using Ultra-High-Definition Liquid-Crystal Displays with Undesirable Light Elimination," *Journal of Display Technology*, V7(7), pp382-390, 2011
- [6-104] Tomasz Kozacki, Grzegorz Finke, Piotr Garbat, Weronika Zaperty, and Małgorzata Kujawińska, "Wide angle holographic display system with spatiotemporal multiplexing," *Opt. Express* 20, 27473-27481 (2012)
- [6-105] Y. Sando, D. Barada, and T. Yatagai, "Holographic 3D display observable for multiple simultaneous viewers from all horizontal directions by using a time division method," *Opt. Lett.* 39(19), 5555-5557 (2014)
- [6-106] Yasuhiro Takaki and Naoya Okada, "Hologram generation by horizontal scanning of a high-speed spatial light modulator," *Appl. Opt.* 48, 3255-3260 (2009)
- [6-107] Jung-Young Son, Beom-Ryeol Lee, Oleksii O. Chernyshov, Kyung-Ae Moon, Hyoung Lee, "Holographic display based on a spatial DMD array", *Opt. Lett.*, Vol. 38 Issue 16, pp3173-3176, August 15, 2013.
- [6-108] Jung-Young Son, Chun-Hae Lee, Oleksii O. Chernyshov and Beom-Ryeol Lee and Sung-kyu Kim, "A floating type Holographic Display", *Optics Express*, Vol. 21 Issue 17, pp20441-20451, August 22, 2013
- [6-109] Xuewu Xu, Xinan Liang, Yuechao Pan, Ruitao Zheng, Zhiming Abel Lum, Phyu Mar Yi Lwin, and Sanjeev Solanki, "Development of full-color full-parallax digital 3D holographic display system and its prospects," *Proc. SPIE 8644, Practical Holography XXVII: Materials and Applications*, 864409 (2013).
- [6-110] Yasunori Ito, Yuki Shimozato, Peng Xia, Tatsuki Tahara, "Four-Wavelength Color Digital Holography," *Journal of Display Technology*, Vol.8, Issue 10, pp. 570-576, (2012)

[6-111] D. Teng, L. Liu, Y. Zhang, Z. Pang, S. Chang, J. Zhang, and B. Wang, "Spatiotemporal multiplexing for holographic display with multiple planar aligned spatial-light-modulators", *Optics Express*, 22(13) 15791 (2014)

[6-112] Jung-Young Son, Manho Jeong, "The Effects of MPE on Electro-Holographic Displays", *Optics Express*, 22(3), pp 2207-2215, 2014

[6-113] <http://www.sony.com/electronics/projector/mp-cl1>

[6-114] Experimentally obtained with a Toppan's lenticular plate with 1 mm pitch, which was made at year 2000.

## List of publications

### Papers related to this thesis

1. Hyoung Lee, Sung-Kyu Kim, Kwanghoon Sohn, Jung-Young Son, and Oleksii O. Chernyshov, "Fringe periods of color moirés in contact-type 3D displays," *Opt. Express*, Vol. 24, Issue 13, pp. 14183-14195, 2016

2, Hyoung Lee, Jung-Young Son, Beom-Ryeol Lee, and Sumio Yano, "Color moirés in contact-type three-dimensional displays," *Optical Engineering*, Vol. 57, Issue 6, pp. 061612-1~9, 2018

3. Hyoung Lee, Jung Kim, Ki-Hyuk Yoon, Jung-Young Son, and Sumio Yano, "Simulation of slanted color moiré in IP-type 3-D displays," *Journal of Optics*, Major revision (2019. 02. 22) and waiting response.

### International conferences related to this thesis

1. Hyoung Lee, Jung Kim, and Jung-Young Son, "period of color moiré fringes in contact-type 3-D display," *International Display Workshops 2016, 3DSA6/3D5-4*, Fukuoka, Japan, Dec. 2016

2. Hyoung Lee, Jung Kim, Do-Hyung Kim, and Sumio Yano, "Multiview image acquisition based on an aperture sharing in Mirrorless camera," *IMID 2017 DIGEST, F54-2*, Busan, Korea, Aug. 2017

3. Hyoung Lee, Jung Kim, Sumio Yano, Jung-Young Son, and Gwanghee Heo, "Simulation of slanted color moires in IP-type 3-D display," *International Display Workshops 2018, Nagoya*, Japan, Dec. 2018